Progress in Materials Science 148 (2025) 101385

Contents lists available at ScienceDirect

Progress in Materials Science

journal homepage: www.elsevier.com/locate/pmatsci

Advances in high entropy oxides: synthesis, structure, properties and beyond

Chang Liu [a,1], Shun Li [b,1], Yunpeng Zheng [a,c], Min Xu [d], Hongyang Su [d], Xiang Miao [e], Yiqian Liu [a], Zhifang Zhou [a], Junlei Qi [a,f], Bingbing Yang [a,f,g], Di Chen [d,*], Ce-Wen Nan [a], Yuan-Hua Lin [a,*]

[a] State Key Lab of New Ceramics and Fine Processing, School of Materials Science and Engineering, Tsinghua University, Beijing 100084, PR China
[b] Institute of Quantum and Sustainable Technology (IQST), School of Chemistry and Chemical Engineering, Jiangsu University, Zhenjiang 212013, Jiangsu, PR China
[c] Key Laboratory of Eco-materials Advanced Technology, College of Materials Science and Engineering, Fuzhou University, Fuzhou, 350108, PR China
[d] The Future Laboratory, Tsinghua University, Beijing 100084, PR China
[e] School of Chemistry, Beijing Advanced Innovation Center for Biomedical Engineering, Beihang University, Beijing 100191, PR China
[f] Foshan (Southern China) Institute for New Materials, Foshan 528200, PR China
[g] Key Laboratory of Materials Physics Institute of Solid State Physics HFIPS Chinese Academy of Sciences, Hefei 230031, PR China

ARTICLE INFO

Keywords:
High entropy oxides

ABSTRACT

The unique structural features of high entropy oxides (HEOs) offer opportunities for flexible and precise structure control, thereby fostering a broad spectrum of structure–property tuning. This

Abbreviations: ABF-STEM, annular bright-field scanning transmission electron microscopy; AC, alternating current; ADASYN, adaptive synthetic sampling; AN, $AgNbO_3$; ARPES, Angle-resolved photoemission spectroscopy; BT, $BaTiO_3$; BTO-BFO-CTO, $BaTiO_3$-$BiFeO_3$-$CaTiO_3$; BNT, $(Bi,Na)TiO_3$; CALPHAD, calculation of phase diagrams; CNF, conductive carbon nanofibre; CSBPN, $(Ca_{0.5}Sr_{0.5}Ba_{0.5}Pb_{0.5})Nb_2O_7$; DC, direct current; DFT, density functional theory; DRX, disordered rocksalt; EBSD, electron backscatter diffraction; EELS, electron energy loss spectroscopy; EDX, energy dispersive X-Ray analysis; EFA, entropy-forming-ability; EM, microscope; EPR, electron paramagnetic resonance; EXAFS, extended X-ray absorption fine structure; FE, Faradaic efficiency; FFT, fast Fourier transform; FPS, flame-assisted plasma sintering; GNP, glycine nitrate procedure; HAADF-STEM, high-angle annular dark-field scanning transmission electron microscopy; HEAs, high entropy alloys; HEBs, high entropy borides; HECs, high entropy carbides; HE-LNMO, $LiNi_{0.8}Mn_{0.13}Ti_{0.02}Mg_{0.02}Nb_{0.01}Mo_{0.02}O_2$; HENs, high entropy nitrides; HEO, high entropy oxide; HER, hydrogen evolution reactions; HT, hydrothermal; LIB, lithium-ion battery; Li-NASICON, lithium–sodium superionic conductor; LOM, lattice oxygen-participated mechanism; MFP, mean free path; MFM, magnetic force microscopy; MLCC, multi-layer ceramic capacitors; ML, machine learning; MOFs, metal–organic frameworks; M.R., mean ionic radii based parameter; NASICON, sodium superionic conductor; NBD, nano beam diffraction; NCM, $LiNi_{0.8}Mn_{0.1}Co_{0.1}O_2$; NSP, nebulized spray pyrolysis; NN, $NaNbO_3$; NP, nanoparticles; NRR, nitrogen reduction reaction; ODT, order–disorder transition; OER, oxygen evolution reaction; PDF, pair distribution function; PEO, poly(ethylene oxide); PES, Photoemission spectroscopy; PLD, pulsed laser deposition; PNR, polar nanoregion; RCP, reverse co-precipitation; RE, rare earth elements; RHEED, reflection high-energy electron diffraction; SAED, selected area electron diffraction; R-O-T-C, rhombohedral-orthorhombic-tetragonal-cubic; SCS, solution combustion synthesis; SE, solid electrolyte; SEM, scanning electron microscope; SPS, spark plasma sintering; SSB, solid-state battery; STEM, scanning transmission electron microscopy; TBC, thermal barrier coating; TEC, thermal expansion coefficient; TEM, transmission electron microscope; TM, transition metal elements; UPS, ultraviolet photoemission spectroscopy; VEC, valence electron concentration; XAS, X-ray absorption spectroscopy; XGBoost, extreme gradient boosting; XMCD, X-ray magnetic circular dichroism; XPS, X-ray photoemission spectroscopy; XRD, X-ray diffraction; YSZ, yttrium-stabilized zirconia.

* Corresponding authors.
E-mail addresses: dichen@tsinghua.edu.cn (D. Chen), linyh@tsinghua.edu.cn (Y.-H. Lin).

[1] Chang Liu and Shun Li are co-first author.

https://doi.org/10.1016/j.pmatsci.2024.101385
Received 4 November 2023; Received in revised form 16 September 2024; Accepted 1 October 2024
Available online 10 October 2024

Multicomponent equiatomic system
Functional properties

review surveys the extensive research carried out on HEOs, from initial exploration to recent advancement, summarizing progress in the refinement of synthesis techniques, elucidation of the high entropy effect, and understanding of atomic structures at multiple scales. Leveraging the impact of high entropy effect on structures, HEOs exhibit a wide range of properties from thermal to electrical, which have potential applications in fields such as thermoelectrics, dielectrics, energy storage, lithium batteries, catalysis, magnetism and supercapacitors. The correlations between structure and property are analyzed, and potential property-property relations are examined. Finally, we underscore the key challenges and unresolved questions that future research needs to address.

1. Introduction

Entropy is a classical thermodynamic parameter to describe the degree of disorder in a material system. The breakthrough synthesis of high entropy alloys (HEAs) [1] has sparked interest in utilizing entropy to synthesise stabilized new single-phase materials, and positioned the high entropy effect as an influential factor for material design and property optimization. The idea of introducing multi-components to increase the disorder of material systems has been expand to ceramics, including oxides, nitrides, carbide and borides [2]. High entropy oxides (HEOs) were first formulated by Rost et al. [3] in 2015, introducing configuration disorder by uniformly distributing various distinct cations across a single sub-lattice. The subsequent surge of scientific research in HEOs has deepened our understanding of high entropy effect and enabled tailoring of properties such as thermoelectrics, dielectrics, energy storage and catalysis, etc. Over nearly a decade of studies, the complexity of investigated structures has increased, ranging from simple forms like rock-salt structure to more intricate configurations like tungsten bronze structure [4] and magnetoplumbite structure [5], from bulk to thin film grown via pulsed laser deposition (PLD) [6–8] and even low-dimensional nanostructures (e.g., nanosheets [9] and nanoparticles [10]). Research scope has also broadened from microscale phenomena to nanoscale features, such as oxygen vacancy [11] and anion doping [12], and from single phase to non-single phase, such as CuCoNi nano alloy exsoluted in $Co_3MnNiCuZnO_x$ [13], CoFeCuNi nanoalloy exsoluted in $Zr_{0.5}(NiFeCuMnCo)_{0.5}O_x$ [14] and $(Sr_{0.25}Ca_{0.25}Ba_{0.25}La_{0.25})TiO_3$/Pb@Bi [15]. The evolution of HEOs research reflects an ongoing trend towards more comprehensive and nuanced explorations of these versatile materials.

Unlike HEAs that exhibit a complete absence of atomic order, HEOs retain a level of consistent atomic alignment, maintaining general lattice structures with multiple elements randomly occupying certain sites. The driving force of high entropy permits both oversized and minuscule elements to integrate into the crystal structure, which would typically struggle to form a stabilized single phase with unique structures. The diversity of elements choice opens vast potential for structure–property optimization. The goal is to understand the underlying principles of HEOs to allow for controlled structural and property engineering through pre-specified phase fractions and morphologies. Despite the considerable amount of research, the impact of high entropy on oxide structures (including crystal structures, valence states, coordination numbers, and local lattice distortions, etc.) and the relationship between structure and property remain unclear. It is evident that the synthesis method, chemical composition, morphology, microstructure, stability, and functional properties are interconnected. For further systematic study of HEOs, a comprehensive and deep understanding of the mechanisms underlying these structure-properties optimization is necessary. Therefore, collective efforts in addressing the aforementioned challenges also need to be summarize and analyzed, outlining a methodological framework for guiding future HEO research.

In recent years, extensive research attention on high entropy ceramics has provoked several insightful reviews [2,16–19], with increasing attention being given to high entropy nitrides (HENs), carbides (HECs), and borides (HEBs). Reviews of HEOs generally focus on either synthesis and structural design [20,21], specific applications like reversible energy storage or/and catalysis [22–26], or certain properties such as magnetism [27]. This paper aims to provide a comprehensive and up-to-date review of HEOs, focusing on different aspects as well as their research methodology (Fig. 1). The discussions and analysis encompass the definition of HEOs, key descriptors, computation and calculations based on these descriptors, the origin of high entropy effect and its four aspects, representative systems, and the structural-property relationships related to their functionalities and applications. From a methodological perspective, both theoretical and experimental approaches are examined, starting with synthesis and structural characterization techniques, to explore how recent research has investigated the diverse properties and applications of HEOs.

2. High entropy oxides

2.1. Definition and descriptors

High entropy oxides typically include more than five elements, each contributing 5–35 at. % at specific cation sites, resulting in a total entropy increase ΔS is more than 1.5R (otherwise it will be classified as medium ($R<\Delta S<1.5R$) and low entropy ($\Delta S<R$)). Initial HEO studies focused on introducing five elements at certain cation sites, but recent studies have broadened to synthesize complex oxides with greater element diversity. This includes multi-components at various cation sites and increasing element variety at certain sites. Defects typically oxygen vacancies [28,29], are attracting increasing attention in studies of HEOs. Typically, HEOs rely on entropy stabilization to achieve a single stable solid solution, surpassing the segregation driven by enthalpy minimization, and maintain a single phase at high temperatures. Brahlek et al. defined HEOs as materials where configuration entropy contributes to formation and

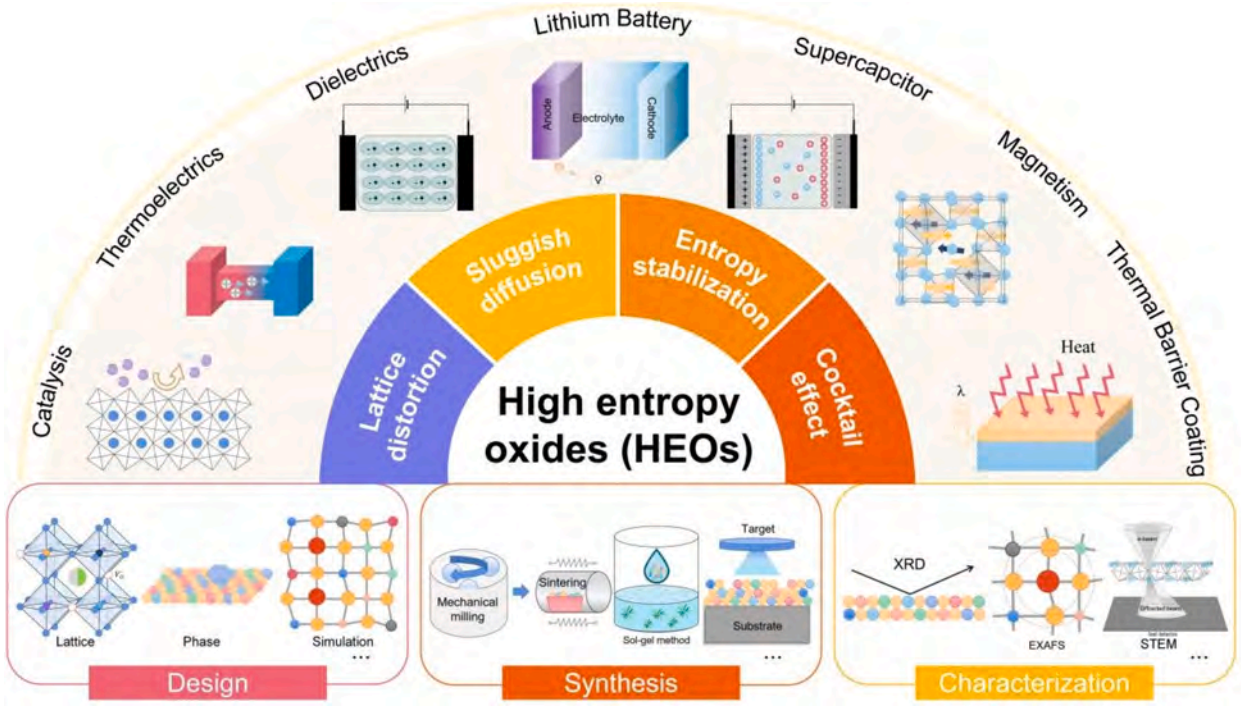

Fig. 1. Schematic sketch of HEO studies.

stability, but is not necessarily dominant over enthalpy [30].

HEOs, with their multi-principal elements and therefore vast composition space, extend the phase space [31], adding complexity to experimental ergodic scanning and embodies the necessities of theoretical models. Effective computation schemes require not only input of experimental data fitting but also appropriate descriptors of structural characteristics. Several empirical descriptors have been developed to assess the phase stability of high-entropy materials [19], analogous to the renowned Hume-Rothery rules for binary solid solutions [32]. These descriptors can be categorized into three groups, each offering a different perspectives on describing configurations.

(1) Descriptors based on entropy and enthalpy

Basically, it is natural to consider thermodynamic parameters as descriptors to describe the structure disorder. These descriptors are derived from Gibbs free energy, by calculating mixing enthalpy and entropy change. Among them, configuration entropy is one of the

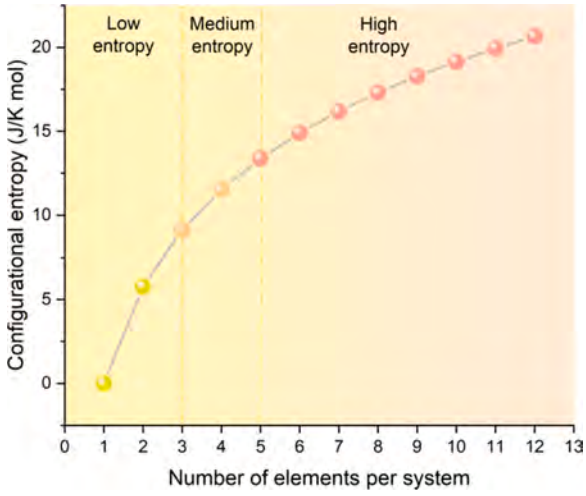

Fig. 2. The relation of mixing entropy with a variation of the number of components with equiatomic fraction.

most widely applied, usually ignoring the effect of possible oxygen vacancies. One of the most classic descriptor is configuration entropy S_{config}, which can be written as:

$$S_{config} = -R\left[\left(\sum_{i=1}^{N} x_i Inx_i\right)_{cation-site} + \left(\sum_{j=1}^{M} x_j Inx_j\right)_{anion-site}\right] \quad (1)$$

where x_i and x_j represent the mole fraction of elements present in the cation and anion sites, respectively, and R is the universal gas constant [23].

Most composition designs focus on introducing disorder in only cation sites but introducing elemental diversity in anion cites has emerged [33], where Eq. (1) still applies. Considering the mathematics of Eq. (1), we would review the empirical classification of high, medium and low entropy. For a system with two elements with varying fractions, the highest entropy can reach to 0.693*R*, when two elements are in equiatomic fraction. Following the same logic, the highest entropy is realized (*R*In*n*) when each elements (the number of elements is denoted as *n*) are in the same mole fraction. For a case of the equiatomic fraction of elements, the configuration entropy varying with number of elements per system can be shown in Fig. 2, which shows the highest amount of entropy a system can get in different numbers of elements. Thus for high entropy, more than five elements are needed. But for medium entropy, more than three elements is enough.

Early studies of adopting high entropy strategy mostly focus on equiatomic design but non-equiatomic design are gaining increased interests [34–36]. While the number of possible combinations of non-equiatomic fractions of elements can be countless in mathematics, recent studies suggest that specific ratios are commonly employed (Fig. 2).

For HEOs with element diversity in different cation sub-lattice sites, Eq. (1) can be extended to:

$$S_{config} = -R\left[\left(\sum_{i=1}^{N} x_i Inx_i\right)_{cation-site1} + \left(\sum_{j=1}^{M} x_j Inx_j\right)_{cation-site2} + \ldots\right] \quad (2)$$

According to Euqation (2), it shows the tailoring flexibility of HEOs can be. If two cation sub-lattice sites are involved in composition complexity, the least overall number of cation elements is still 5. Multiple sites of diversity provide enhanced stability and structural robustness for entropy design. Besides, for certain fuctionality, composition complexity in different sub-lattice sites are necessary.

Beyond configuration entropy, further entropy terms considering other contributors of entropy such as dislocation (Eq. (3)) broaden the scope of understanding high entropy effect. The mean strain energy raised by the dislocation contributes to the overall enthaply increase in the HEO system. High configuration entropy brought by compositional complexity can compensate for the strain energy associated with dislocations. However, dislocations create additional microstates or configurations that atoms can occupy. In this way, the dislocation entropy can also be a contributor to overall free energy decrease, which is expressed as follows:

$$\Delta S_{\text{dislocation}} = -k_B\left[p_i \text{In} p_i + (1-p_i)\text{In}(1-p_i)\right] \quad (3)$$

where k_B is the Boltzmann constant, p_i is the possibility to detect the dislocation in the model which is proportional to the total number of cations along the dislocation line [37].

In the practical case of $(Sm_{0.2}Gd_{0.2}Dy_{0.2}Er_{0.2}Yb_{0.2})_2Zr_2O_7$, p_i can be 0.34 %. $\Delta S_{\text{dislocation}}$ displays in the form of Shannon entropy, which measures the randomness or uncertainty of a probability distribution. The presence of dislocations is rare, which fits in the appling situations of Shannon entropy.

Similar to Eq. (2), the Li-configurational molar entropy change is written as Eq. (4), depicting the distributional variability of Li atoms in the host structure. In a very simplified ideal solid solution model with Li atoms moving freely between a given number of empty sites, without changing interactions (among each other and with the host lattice) during the charge/discharge process, the molar entropy change can be expressed as follows:

$$\Delta S_{config}(x) = -R\left[x\text{In}x + (1-x)\text{In}(1-x)\right] \quad (4)$$

where R is the molar gas constant and x is the relative amount of exchangeable sites being occupied [38].

Besides, Sarkar et al. [39] applied sub-lattice model and claimed $\frac{S_{config}}{atom}$ (Eq. (5)) as a more reliable metric in comparison of HEOs:

$$\frac{S_{config}}{atom} = -R\left(\frac{\sum_{x=1}^{x} a^x \sum_{N=1}^{N} (f_i^x Inf_i^x)}{\sum_{x=1}^{x} a^x}\right) \quad (5)$$

where *R* is the universal gas constant, a^x is the number of sites on the *x* sub-lattice, f_i^x is the fraction of elemental species randomly distributed on the respective sub-lattice and *N* is the number of elements in a given sub-lattice [39].

Actually for a spinel structure AB_2O_4, a^x for each sites (A, B and O) are 1, 2, and 4 respectively. Thus the configuration entropy is calculated at each sites respectively. $\frac{S_{config}}{atom}$ can be considered as the weighed average of S_{config} all the sub-lattice sites for a HEO. If elemental diversity is introduced in only one type of sub-lattice sites, then Eq. (5) can be expressed the same as Eq. (3). Eq. (2) and (5) represent different ways of considering the contribution of configuration entropy. For Eq. (2), all the sites are considered equal in donating the overall configuration entropy while for Eq. (5), the amount of sub-lattice sites appearing in HEOs is considered and a higher fraction of the sub-lattice sites means a higher contribution in S_{config}.

Except for configuration entropy, vibration entropy can be obtained by Density functional theory (DFT) calculations and started to be considered as a contributor to phase stabilization, whose expression is given as below:.

$$S_{vib} = \frac{1}{2T}\sum_{qj}\hbar\omega_{qj}coth\left[\hbar\omega_{qj}/2k_BT\right] - k_B\sum_{qj}ln\left[2sinh\left(\hbar\omega_{qj}/2k_BT\right)\right] \quad (6)$$

where T, $\hbar$, q, j and ω_{qj} are the temperature, reduced Planck constant, wave vector, band index, and phonon frequency, respectively [40].

Applying S_{vib} is rather rare, due to the impractical costs of first-principles calculations and the invalidated accuracy of DFT calculations for vibration energies, as the calculation often relies on nonunique supercell models and zero-K harmonic approximation, excluding anharmonic effects at high temperatures [41]. Besides, experimental studies on S_{vib} are also scarce due to the complexity in delicate measurements and the intricate charge balance between cations and anions. Consequently, from the aspect of the heat capacity, the vibrational entropy can be expressed as follows:

$$\Delta S_{vib} = \int_0^T \frac{C_p(T)}{T}dT \quad (7)$$

Woodfield et.al. [42] synthesized a series of multicomponent rutile oxides and challenged the conventional understanding that increased disorder would lead to increased vibrational entropy. The excess vibrational entropy could be attributed to the increase in polyhedral distortions due to cationic disorder. Increased component diversity can lead to distortions in the crystal lattice, which may limit the range of vibrational modes or restrict certain vibrations. Variations in bond strengths between different atoms could result in stiffer bonds in some cases, which would reduce the amplitude of atomic vibrations. Thus, a more "rigid" lattice would have fewer low-frequency phonon modes, leading to a reduction in overall vibrational entropy.

Instead of simply applying entropy as descriptors, Pitike et al. [43] used the statistical mean and standard deviations of local mixing enthalpies to predict the stability of five-component oxides. Sarker et al. [44] invented an entropy-forming-ability (EFA) descriptor, by calculating the energy distribution "width" of a given unit cell with a randomized sampling of elements. The narrower distribution means the easiness of accessing disordered configuration and thus favors high entropy. The expression of EFA can be written as:

$$\mathrm{EFA} = \left(\sqrt{\frac{\sum_{i=1}^{n} g_i(H_i - H_{mix})^2}{(\sum_{i=1}^{n} g_i) - 1}}\right)^{-1} \quad (8)$$

where n is the total number of sampled geometrical configurations and g_i are their degeneracies. H_{mix} is the mixed-phase enthalpy approximated by averaging the enthalpies H_i of the sampled configurations [44]:

$$H_{mix} = \frac{\sum_{i=1}^{n} g_i H_i}{\sum_{i=1}^{n} g_i} \quad (9)$$

Compared with other high entropy materials, descriptors of HEOs based on thermodynamics still possess further space of developments. Firstly, these descriptors still fail to realize a balance between the simplicity in mathematical form and the integrity of actual thermodynamic details. For example, Liu et al. [45] put forward a descriptor largely determined by the internal strain field of different elements on the same site which is related to the enthalpy, and predicts the atomic solubility for high-entropy materials. A parameter δ is defined, involving the average shear modulus and the effective lattice constant. Multicomponent solid solution systems are derived from a quasibinary reaction of various binary solid solutions, thus adding to the complexity of the total free energy change in an equimolar multicomponent solution. This status quo is reasonable since solving the thermodynamics of HEOs is considered more challenging. Calculation of Phase Diagrams (CALPHAD) approach [46] is the most extensively used computational thermodynamics method to predict phases of high-entropy materials, which uses thermodynamic parameters of end members from an existing database constructed by applying experiments and first-principles calculation [46], and indentifies the minimum [47]. While CALPHAD has been successfully applied to high-entropy alloys, its application to HEOs is rare. Some results have validated its feasibility in slag oxide systems [48] and perovskites [28]. One major challenge is that the traditional thermodynamic database is based on constituent simple compounds, and high-entropy compositions are consist of many simple compounds and are located at the center (rather than edges) of the phase diagram, which causes concerns for database reliability [46,19].

Secondly, these descriptors still mainly focus on either entropy or enthalpy. Only a relative empirical quantization traced back to HEAs provides the configuration entropy necessary to meet the standard of high entropy. Enthaply is considered less significant as a value to be surpassed by $T\Delta S$. EFA is one of the few descriptors built around enthaply and describe the single-phase stability through the formation energy distribution based on DFT calculations. But it cannot fit in all cases considering the calculation costs and applications in high entropy carbides shows its weakness in non-homogeneous enthalpy landscapes [49]. Therefore, novel descriptors which can depict the competition between entropy and enthalpy are needed. The DEED descriptor, proposed by Curtarolo et.al. [50] balanced the entropy gain and enthalpy cost associated with the formation of these materials, allowing for a more accurate classification of their synthesizability. However, further testing of the DEED descriptor is required in HEOs to validate its applicability.

Curtarolo et.al [50] characterized the systematic energy as a thermodynamic density of states spectrum $\Omega(E)\delta(E)$ in a continuum population and approximate the random distribution as an ensemble average of ordered representative states called partial occupation (POCC) tiles via DFT calculations. The DEED descriptor is described as follows:

$$DEED = \sqrt{\frac{\sigma_{\Omega}^{-1}[H_f]}{\langle \Delta H_{hull} \rangle_{\Omega}}} \tag{10}$$

where H_f and $H_{f,full}$ are the DFT formation energies of the partial occupation POCC tiles and the convex hull, respectively.

Similar to other density of states in condensed matter physics, a probability distribution of a function $f(E)$ through the renormalization $\int f(E)\Omega(E)\mathrm{d}E/\eta$ is built, where $\eta \equiv \int f(E)\mathrm{d}E$ is the renormalization constant. Thus, the statistical momenta of the POCC tiles is extracted as H_f and $H_{f,full}$.

$$\sigma_{\Omega}^2[H_f] = \frac{1}{\eta}\int \left[H_f(E) - \langle H_f \rangle_{\Omega}\right]^2 \Omega(E)\mathrm{d}E \tag{11}$$

$$\langle \Delta H_{hull} \rangle_{\Omega} = \frac{1}{\eta}\int \left[H_f(E) - H_{f,full}\right]\Omega(E)\mathrm{d}E \tag{12}$$

For a thermodynamic density of states Ω, comprising of a set of n discrete POCC tiles with formation energies $H_{f,i}$ and factor-group degeneracies g_i, the momenta can be calculated as:

$$\sigma\{H_{f,i}\} = \sqrt{\frac{\sum_{i=1}^{n} g_i\left(H_{f,i} - H_{f,full}\right)}{\left(\sum_{i=1}^{n} g_i\right) - 1}} \tag{13}$$

$$\langle \Delta H_{hull} \rangle = \frac{\sum_{i=1}^{n} g_i\left(H_{f,i} - H_{f,full}\right)}{\sum_{i=1}^{n} g_i} \tag{14}$$

$$\langle \Delta H_f \rangle = \frac{\sum_{i=1}^{n} g_i H_{f,i}}{\sum_{i=1}^{n} g_i} \tag{15}$$

Besides, the mixed enthalpy–entropy descriptor (MEED) proposed by Dey et.al. [51] also needs further adaptations in studies of HEOs. MEED criterion for synthesizability can be applied via an auxiliary dimensionless descriptor r_{MEED}:

$$r_{\mathrm{MEED}}(\Delta H_{\mathrm{r}}, \langle \Delta E_D \rangle) \equiv \sqrt{\left(\frac{\Delta H_r}{\Delta H_r^c}\right)^2 + \left(\frac{\langle |\Delta E_D| \rangle}{\langle |\Delta E_D| \rangle^c}\right)^2} \tag{16}$$

where ΔH_r is the difference in formation enthalpy between the solid solution and the most stable compound formed by its constituent elements. $\langle |\Delta E_D| \rangle$ is the average of absolute differences in defect formation energy among all possible substitutional point defects in the respective constituent host materials in the same crystal structure of the high entropy materials. ΔH_r^c and $\langle |\Delta E_D| \rangle^c$ are the corresponding ΔH_r and $\langle |\Delta E_D| \rangle$ when all the elements are considered within the studied set.

Adapting this MEED, DFT calculations of five-metal carbides showed that Compositions with $r_{\mathrm{MEED}} > \sqrt{2}$ are considered hardly synthesizable.

(2) Disorder factor for different structures

Apart from thermodynamic descriptors for depict of structural disorder, a series of disorder factor focusing on describing lattice distortion and atomic deviation have emerged. For high entropy pyrochlores, size disorder factor δ and mass disorder factor g can be written as Eqs. (17) and (18). The partial size disorder can be written as Eq. (17) for all elements sharing the same lattice sites, while Eq. (18) is the modified form considering A and B sites for high entropy pyrochlores. Size disorder factor has been reported to be a more effective descriptor than configuration entropy to describing the fluctuation of thermal conductivity [52].

$$\begin{cases} g = \sum_{i=1}^{n} x_i\left(1 - \dfrac{m_i}{\overline{m}}\right)^2 \\ \delta = \sqrt{\sum_{i=1}^{n} x_i\left(1 - \dfrac{r_i}{\overline{r}}\right)^2} \end{cases} \tag{17}$$

$$\begin{cases} g^* = \sqrt{g_A^2 + g_B^2} \\ \delta_{size}^* = \sqrt{\delta_A^2 + \delta_B^2} \end{cases} \tag{18}$$

where x_i is the atomic fraction, m_i and r_i are the mass and radius of the i^{th} ion component, $\overline{m}$ and $\overline{r}$ are the overall weighted average of mass and ionic radius, δ_A and δ_B are the lattice size differences related to the A and B sites in the pyrochlore structure, respectively [52].

Similarly, the size disorder factor of high entropy perovskites can be written as:

$$\delta = \sqrt{\sum_{i=1}^{N} c_i \left(1 - R_{B_i} / \sum_{i=1}^{N} c_i R_{B_i}\right)^2} \tag{19}$$

where R_{B_i} is the radius of the ith cation at the B site; c_i is the mole fraction of the ith cation [29].

Similarly, a radius-based criteria was put forward for fluorite, where a mean ionic radii-based parameter (M.R.) is applied, according to Eq. (20) showing below:

$$\text{M.R.} = \sqrt{\frac{\sum_{i=1}^{N} (r_i - \bar{r})^2}{N-1}} \tag{20}$$

where N is the number of cations, r_i is the radii of the individual cations, and $\bar{r}$ is the average/mean radii. If M.R. > 0.095, a single-phase fluorite is preferred, else low temperature dual-phases (fluorite and bixbyite) and a high temperature single-phase bixbyite are anticipated [53].

While methods such as special quasirandom structures and coherent-potential approximation are utilized to reduce the cost, and calculations based on thermodynamics, empirical rules and first principles have been successfully employed, computational studies on HEOs remain in their early stages. Applying advanced tools like machine learning (ML) and other artificial intelligence (AI) algorithms can address the lack of precision in describing local lattice distortion and interatomic interactions. Thus the combination of the disorder factor with entropy-based descriptor is possible for data collection as well as other coefficients such as electronegativities. Fang et.al [54] applied three classic ML algorithms—Extreme Gradient Boosting (XGBoost), Random Forest, and Naïve Bayes to predict the crystal structures of HEOs, in which the XGBoost model showed the best performance. Features collected include the anion-to-cation radius ratio $\frac{r_A}{r_C}$, differences in Pauling and Mulliken electronegativities ($\Delta\chi_{Pauling}$ and $\Delta\chi_{Mulliken}$), and other thermodynamic and structural parameters. The ADASYN (Adaptive Synthetic Sampling) method was employed to generate synthetic data for underrepresented classes, enhancing the training of ML models. The anion-to-cation radius ratio $\frac{r_A}{r_C}$ had the greatest impact on predicting the crystal structure. Lower values of $\frac{r_A}{r_C}$, $\Delta\chi_{Pauling}$, and $\Delta\chi_{Mulliken}$ tend to lead to a fluorite crystal structure, while larger values favor spinel and rock-salt structures.

Additionally, the most challenging issue for computations of HEOs is the vast composition space and the consequent high computation cost. High throughput calculations, combined with ML-incorporated big-data discovery, are paving the way for a deeper understanding of HEOs, ranging from their structures to properties.

(3) Classical structure descriptor for different structures:

Some researchers used crystallographic information such as the tolerance factor for perovskites [55], or simply calculated the standard deviation of ionic radii for fluorites [53] to describe the high entropy on structures. For example, tolerance factors for perovskite ABO_3 [56] pyrochlore AB_2O_7 [57], as shown in Eqs. (21) and (22) respectively, reflect the general ability of HEOs in remaining certain type of atomic arrangements.

$$t_{mean} = \frac{r_{A,average} + r_{B,average}}{\sqrt{2}(r_{B,average} + r_O)} \tag{21}$$

$$t = 1.43373 - 0.42931\left(\frac{r_{A,average} + r_O}{r_{B,average} + r_O}\right) \tag{22}$$

where $r_{A,average}$ and $r_{A,average}$ are the average radius of elements at A and B sub-lattice sites respectively. Besides, for pyrochlore structures, the structural stability of pyrochlore is mainly determined by the ratio between the average ionic radius of A and B cations $\left(\frac{r_A}{r_B}\right)$. The defect fluorite structure is favored when the ratio $\left(\frac{r_A}{r_B}\right)$ is smaller than 1.46 and the pyrochlore structure is favored as the ratio $\left(\frac{r_A}{r_B}\right)$ range of 1.46 to 1.78 [58].

A number of descriptors have been mentioned according to their basis of determination. It's worth noting that, for a designed HEO system, a robust and highly reliable general descriptor to accurately depict the effect of high entropy in phase formation and stability is still lacking. The descriptors discussed below are generally effective under specific circumstances, and some of them lack sufficient physical insights.

2.2. The origin of high entropy effect in HEOs

The high entropy effect primarily stems from the increased possibilities of arrangement (including dislocations) following the integration of multiple elements, leading to an increase in configuration entropy ΔS_{conf}. Based on the Boltzmann hypothesis, the ΔS_{conf} for a multiple-species system usually aids the reduction of overall Gibbs free energy and thereby stabilizes the system. However, prior studies suggested that entropy is not always the sole driving force for solid solution formation [59]. Though the configuration entropy presents and usually plays a significant role in synthesis, the effect is still limited to some extent and unable to surpass the rule of the

solubility equilibria [60]. Configuration changes can extend to alterations in atomic interactions, which can be described via numerous parameters: cation–anion bond lengths, degree of covalence, polarization, valence state, local bond angles, vibration frequencies, magnetic effects, etc. Consequently, through strategic compositional, structure and processing design (even adjustments on a short scale), the thermodynamic competition between entropy and enthalpy can be managed to yield controllable lattice distortion and electronic structures.

The interplay between atoms is often regarded as a consequence of the introduction of configuration entropy. The debate on whether configuration plays dominated effect or if other factors are independent of configuration persists, impacting our understanding of entropy components. In some simple oxide cases, spin has been considered as a contributor to entropy and has aided in describing certain properties, such as Na_xCoO_2 with mixed valence Co cations [61]. For the spin system, the spin entropy is a function of the magnetic field. The concept of spin entropy is related to the degeneracy of electronic states, which can be captured through measurements of thermopower according to Hubbard model under Stirlings approximation. It can also follow the form of configuration entropy as $s = k_B \mathrm{I}ng$, where represents the degeneracy. For cobalt oxides such as $NaCo_2O_4$ and $La_{1-x}Sr_xCoO_3$, the degeneracy can be denoted as $g = g_3^{N_A-M} g_4^M \frac{N_A!}{M!(N_A-M)!}$, where g_3 and g_4 are the number of the configurations of Co^{3+} and Co^{4+} respectively, M is the number of Co^{4+} sites, and N_A is the overall available sites in the system. Due to the complex composition of high-entropy oxides, the spin states of different elements can be distributed in a variety of ways in the lattice, which results in a diversity of local spins. Studies of HEAs suggest performing Monte Carlo simulations to sample the configurations of the spin system and calculate averages of certain state functions. Therefore, the largest eigenvalue of the transfer matrix of the spin system is obtained and thus so does the free energy per sites. Finally the entropy is calculated using the thermodynamic relationship between the free energy [62]. Similarly in HEOs, a Monte Carlo study was performed to theoretically predict of the magnetic behavior corresponding to $La(Cr_{0.2}Mn_{0.2}Fe_{0.2}Co_{0.2}Ni_{0.2})O_3$ and generates random spin configuration by a random distribution based on a probability. A classical Heisenberg model using only the intrinsic spin and exchange parameters was shown to be sufficient to predict complex magnetic behaviors of comprised of many different magnetically active 3*d* transition metals [63]. HEOs studies mainly correlate their spin structures with magnetic order/disorder [63,64], treating it as a subsequent effect of configurational disorder. Furthermore, vibration has been considered as an independent contributor to entropy in metallic glasses [65]. A study of HEO-based lithium-ion batteries (LIBs) by Friedrich et al. demonstrated the dual effects of configuration and vibration, associating vibration entropy with changes of vibrational frequencies within the crystal [38]. Compared to HEOs, high entropy metal carbides [66] and alloys have received more extensive research attention.

High entropy effects can facilitate a randomized cation distribution across all length scale, adhering to a basic crystal structure order. However, an examination of local arrangement reveals some degree of short-range order. Over long ranges, cations and anions are confined within the crystal sub-lattices. For each cation sites, different species of metal ions are randomly distributed, providing a high homogeneity from the micro-scale to the nano-scale [67,68]. This is in contrast to materials with medium entropy effects, whereas some level of segregation across differing length scales is anticipated [30,69]. Factors such as composition design, preparation conditions, temperature, particle size can affect the extent of ordering. In the short range(i.e. nano-scale), a high density of dislocations ($\sim 10^9$ mm^{-2} [37] and $\sim 10^{14}$ mm^{-2} under deformation [70]), a higher degree of clustering [71] and enhanced polarization fluctuation [72] were observed. In addition, phenomena such as charged coupled substitutions and defects (e.g. oxygen vacancies [73]) are likely to occur due to lattice distortion arising from the atomic size mismatch among dissimilar metal cations.

The high entropy effect can establish a thermodynamic stable solid phase at relative high temperatures [23]. Typically the greater component diversity, the higher temperature is required for synthesis. The multi metal–oxygen bonds formed by the driving force of high entropy effect showed their stability. Additional doping to already-synthesized Li/Mn-doped $(Mg_{0.2}Co_{0.2}Ni_{0.2}Cu_{0.2}Zn_{0.2})O$ system by Chen et al. [74] demonstrated a weaker bonding compared to initial cation-oxygen ionic bonds in the undoped systems, leading to improved better compressible behavior. However, phase formation is also subject to the kinetics achievable at given temperatures. The kinetics of HEOs remain less studied compared to HEAs, which are often associated with sluggish kinetics of diffusion compared to conventional alloys and pure metals [75]. Such slow kinetics have been invoked to interpret the room temperature persistence of high temperature disordered structures displaying higher symmetry than their low temperature counterparts (e.g. disordered Fd-3m spinel $(Co, Cr, Fe, Mn, Ni)_3O_4$ [47]). Due to the strong covalent bond and low diffusion coefficient, HEOs depend on solid-phase mass transfer for densification. Large lattice distortion in the high-entropy system can further hinder the solid-phase mass transfer rate [76].

The sluggish diffusion of cation prefers the formation of long-range order or tendency of phase segregation for elements involved with clustering preference [77], and is used in explaining the excellent structure stability of HEOs in thermal coating [78]. The sluggish diffusion effect has been widely reported in high entropy rare-earth zirconates [78,79], reflected as lower grain growth rates and the reduction of grain boundary energies. Studies suggested that the inhibition of grain boundary migration which is benefit for grain refinement. Gao et al. [80] utilized *in situ* atmospheric STEM to visualize the nucleation and grain growth process of fluorite $(La_{0.2}Er_{0.2}Sm_{0.2}Yb_{0.2}Y_{0.2})_2Ce_2O_7$ synthesized through a polymeric-precursor-derived sol–gel approach, demonstrating slow grain growth through atom diffusion at temperatures below 900 °C while a liquid-phase-assisted grain growth process at higher temperatures. However, other studies focusing on hexaaluminates [81] challenged the idea that the sluggish diffusion effect dominated the grain growth behaviors. The transport properties studied by Grzesik et al. [82] showed that the obtained values of diffusion coefficients were within the typical ranges for transition metal oxides, failing to confirm the presence of the sluggish diffusion effect in HEO_x.

While the aim is typically to form single phase HEOs, precipitation can sometimes occur to achieve overall stability, and the initial composition design does not always yield expected results. Yao et al. [69] reported that $Zr_{0.2}Y_{0.2}Ta_{0.2}Nb_{0.2}Yb_{0.2}O_2$ consisted a monoclinic structure $M-ABO_4(ZrO_2)$ with a small amount of ZrO_2-rich particles. Luo et al. [83] reported the precipitation of Bi in their $Sr_{0.9}La_{0.1}(Zr_{0.25}Sn_{0.25}Ti_{0.25}Hf_{0.25})O_3$ system. Furthermore, Furthermore, both metallic particles and oxides (such as Ti_3O_5 [15]) have

been found under reduced annealing atmosphere. Precipitation is typically accompanied by by changes of valence state, or alterations of the local cation coordination environment, reflecting the competition between entropy and enthalpy. The precipitation of high-entropy reverse spinel $Co_3MnNiCuZnO_x$ structure has been utilized in catalysts and exsoluted CuCoNi nanoalloys have been observed to generate a sintering-resistant metal-oxide interface for the CO_2 hydrogenation reaction [13].

Overall, the elemental chosen criteria for HEOs can be consolidated into the following points:

(i) The ionic radii of the cations on a specific site at a specific oxidation state and coordination number should be similar, thus rare earth and transition metal elements are frequently employed;

(ii) At least one of the component oxide systems should possess a unique prototype structure;

(iii) Some elements should be included to compensate the excessive positive/negative charge and sometimes the smaller/larger ionic radii;

(iv) Potential lattice sites that cations can occupy should be considered, ensuring that elemental disorder is introduced to more than one type of sub-lattice sites;

(v) At least one pair of the constituent oxides should not be in completely miscible;

The selection of the composition also depends on the target structures. For instance, in perovskite structures, the tolerance factor determines the favored crystal structures. In the case of binary oxides, at least one binary oxide pair should demonstrate incomplete miscibility at 0.5 mol fraction, according to the oxide binary phase diagram [84].

2.3. *The four aspects of the high entropy effect*

Originated from HEAs [85], four aspects have been employed to describe the structure–property transformation of high entropy ceramics (including HEOs) brought by high entropy design, which are the entropy stabilization effect [86–88], the lattice distortion effect [56,89,90], the sluggish diffusion effect [75,82], and the cocktail effect [19,59], as shown in Fig. 3.

The entropy stabilization effect manifests as anomalous stabilization of the phase at the synthesis temperature, where the increasing entropy ΔS contributes to the decrease of Gibbs free energy ΔG according to the well-known equation $\Delta G = \Delta H - T\Delta S$. The large entropy contribution can overshadow the typically positive enthalpy term ΔH, thus plays a significant role in enhancing the solubility of certain elements and improving the stability of certain structures such as pyrochlores, though the enthalpy contribution toward the overall thermodynamic stability should not be dismissed.

The sluggish diffusion effect is a postulation of slower diffusion of individual elements in systems with higher configuration entropy of mixing than those with lower configuration entropy of mixing. Considering the physical root of diffusion, the atom should overcome the energy barrier to move from one site to another. For an ordered crystal structure, the possibilities of diffusion activated barrier are relative simple and thus dominate the way to form a phase. For HEAs, however, the complexity of diffusion originates from the varied local atomic environment that does not simply lead to the increased energy barrier with the increase of element numbers at certain sub-lattice sites [91]. As discussed in Section 2.2, compared to HEAs, the sluggish diffusion in HEOs warrants further investigations. The diffusion effect is more complex compared to HEAs due to the ionic bonding between metallic ions and oxygen ions. For HEOs, oxygen self-diffusion might not be preferred during the formation [92]. From a case study of (Co,Cu,Mg,Ni,Zn)O where the stoichiometry of oxygen is tunned via treatments in different atmospheres, the obtained values of diffusion coefficients are within the ranges typical for transition metal oxides and do not confirm the presence of the sluggish diffusion effect [93].

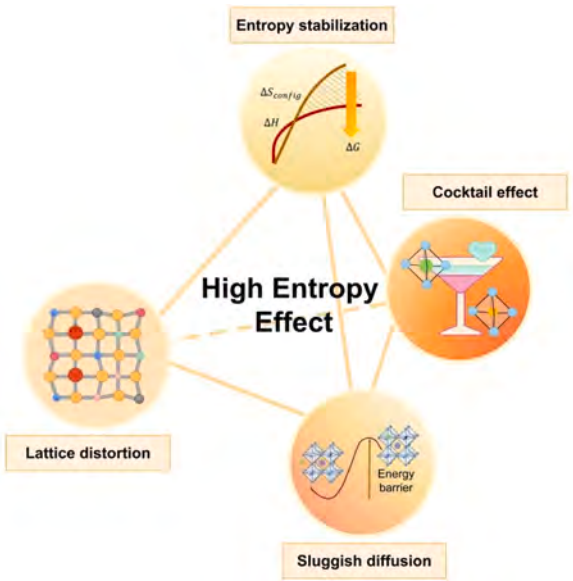

Fig. 3. Schematic sketch of the four aspects of the high entropy effect.

The lattice distortion effect describes the deviation of atomic positions from their intrinsic lattice without element diversity. The radius differences brought by elemental variety at certain sublattice sites result in a local stress field. And thus defects are likely to form to relax the lattice, increasing the local heterogeneity. The lattice distortion contributes to the various degrees of break of local arrangement order (depending on chosen elements) and thus plays a vital role in amorphization, nanostructure evolution, and band gap tuning. While cation elements introduce a varied degree of lattice strain, the oxide lattice serves as a dynamic matrix to accommodate these structural distortions.

The cocktail effect refers to the emergence of unexpected features greater than the weighted average performance of each component, such as the simultaneous enhancements of properties that are unavailable in each component solely appearing, thus providing vast space for compositional and structural possibilities for HEO design. The origin of the cocktail effect can be attributed to the deviation of the ideal mixing theory.

2.4. Representative HEO systems

Based on structural characterizations and calculations of HEOs, researchers have gained a fundamental understanding of elemental-specified features and disorder behaviors in the short range for a certain structure system. Through these findings, how the influence of certain elements on the atomic arrangement appears in the short range offers insights for composition and structure design. Among investigations of different structures, three representative HEO structure systems are studied most, which are rocksalt, perovskite and pyrochlore structures respectively. The following discussions will focus on the structure analysis of certain elemental compositions, including elemental-specified characteristics in structures and correlations of related structures.

2.4.1. Rocksalt HEO system

Efforts to analyze and understand the rocksalt HEO systems, the first synthesized system of their kind, have revealed some intriguing characteristics in composition design via both experimental and computational methods. Firstly, certain elements tend to segregate or cluster in random mixing. Metropolis Monte Carlo simulation of (Co,Cu,Mg,Ni,Zn)O by Pitike et al. [43] highlighted the segregation tendency of Zn and Cu, and preference of avoiding element mixing between Zn-Cu, Zn-Ni pairs while Mg, Co, and Ni readily form disordered solid solutions. The observed Cu clustering is attributed to a competition between elongated coordination preferred by Cu ions due to the Jahn-Teller effect and the regular octahedral coordination preferred by the other cations [94]. Additionally, DFT calculation by Anand et al. [95] revealed specific ordering order segregation between Cu-Cu and Cu-Zn pairs, where Cu-Zn pairing other than Cu-Cu pairing is preferred in high energy configuration.

Secondly, the effect of high entropy altered neighboring cations. Dupuy et al. [96] investigated the impact of grain size on electronic structure. They found heat treatment coarse-grained sample taken below the entropic transformation temperature resulted in increased lattice distortion due to transformations to enthalpy-stabilized electronic structures, and reversible transformations of Cu, Co, and Zn ions from six-fold to four-fold coordinated structures from low to high valence state. Zn can accommodate two-thirds of its neighbors with other cations, typically, Mg and Co [43]. Thirdly, the competition among the electrical properties (including electronic

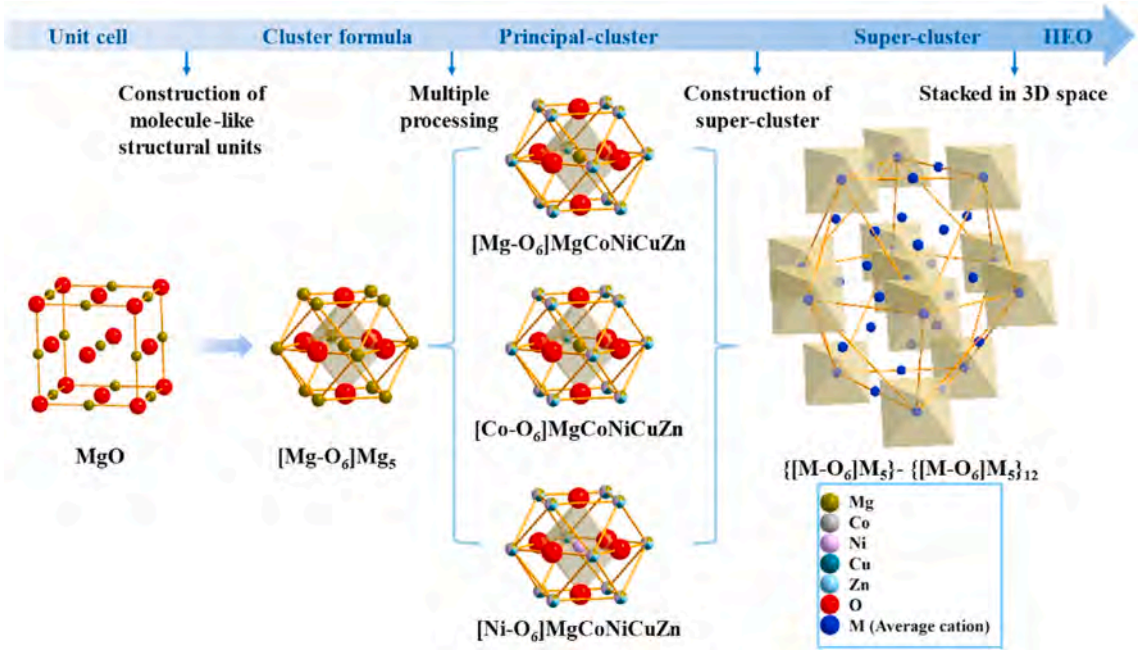

Fig. 4. Schematic diagram of the design process for rocksalt structure HEOs based on cluster-plus-glue-atom model [97]. Copyright © 2022 Elsevier.

states, ground states, and ionicity) of metal elements leads to the preferred deviation of bonding behaviors. The introduction of less electronegative Mg and Zn leads to enlarged Co/Ni-O covalency [73].

The phase instability introduced by elements with non-rocksalt structures and improved phase stability introduced by increased element diversity should reach an equilibrium. Through the cluster-plus-glue-atom model, atomic configurations can be regarded as the combination of cluster units connecting via glue atoms. Based on this understanding, elements with non-rocksalt structures (e.g. Cu, Zn) can occupy glue atom sites to reach a better structural configuration and geometric compatibility by lowering the proportion of elements with non-rocksalt structures and reducing the driving role of conformational entropy in the multi-phase to single-phase transition (Fig. 4) [97].

2.4.2. *Perovskite HEO system*

Perovskite HEOs, compared to rocksalt structures with a single metallic sub-lattice, offer increased structural flexibility with their A and B types of sub-lattice sites. Additionally, perovskite structures possess relatively high structure compatibility due to the wide tolerance factor range(0.75 ~ 1), enabling greater elemental diversity. DFT calculations by Sahinovic et al. [98] confirmed the interdependence between various parameters of perovskites/infinite layer structures (elements involved are shown in Fig. 5 (**a**)), including atomic properties, lattice parameters, tolerance factor, and different energies (Fig. 5 (**b**)). They identified group-resolved stability trends of the perovskite phase for nitrides, oxides, and fluorides (Fig. 5 (**c**)), providing a fundamental understanding of pristine perovskite structures. These perovskite oxides prefer vertical compression under layer conduction. The formation energy of perovskite structures was predominantly determined by anion sites, with B sites having a particularly strong influence on basal lattice parameters. However, in infinite layer scenarios, the vertical lattice parameter exhibited no correlations with other quantities.

When introducing the high entropy effect, the mechanism of phase transformation can be understood via Ghosh electronegativity vs d-valence diagram, Z/a and valence electron concentration (VEC) (Fig. 6). As shown in Fig. 6**(a)**, there is a significant overlap between pyrochlore, fluorite, and perovskite groups (monoclinic and cubic). This overlap can be reproduced as Voronoi diagram (Fig. 6**(b)**), providing further insights into what drives phase change in oxide materials through correlations with mechanisms such as

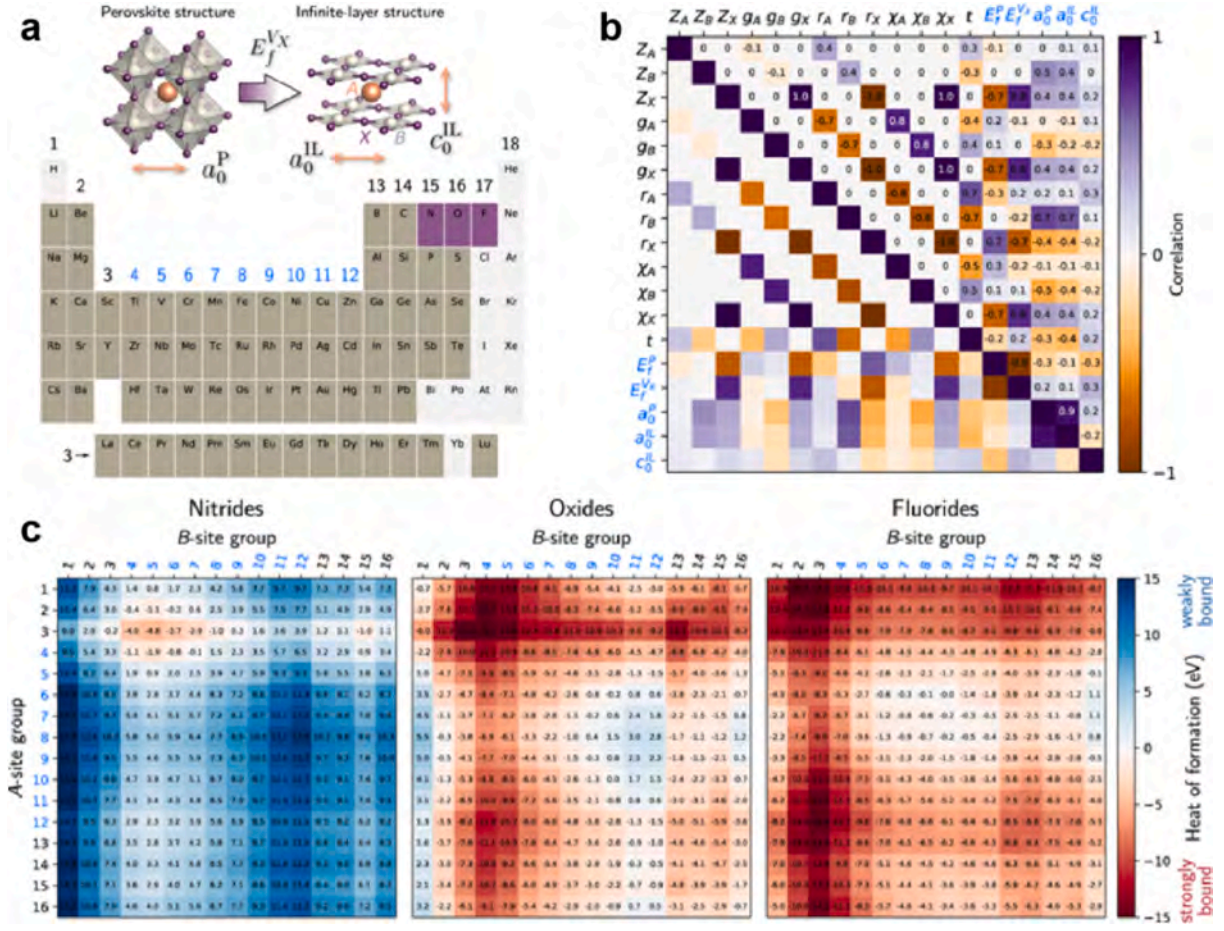

Fig. 5. (a)Elements involved in studies for perovskite/infinite layer structures, 69 for A & B sites. (b)The correlation matrix r_{ij} analyzes the interdependence of the different observables for studied perovskite/infinite layer nitrides, oxides, and fluorides. (c)Group-resolved stability trends of the perovskite phase [98] (Reproduced). Copyright © 2022 The Author(s).

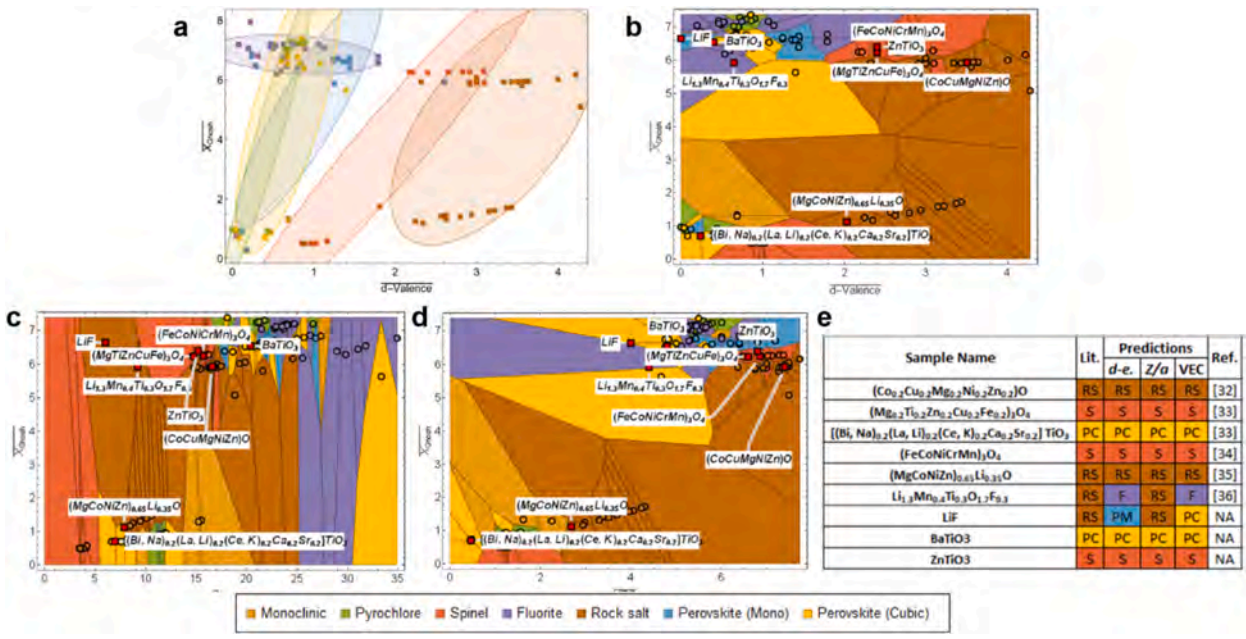

Sample Name	Lit.	Predictions			Ref.
		d-e.	Z/a	VEC	
$(Co_{0.2}Cu_{0.2}Mg_{0.2}Ni_{0.2}Zn_{0.2})O$	RS	RS	RS	RS	[32]
$(Mg_{0.2}Ti_{0.2}Zn_{0.2}Cu_{0.2}Fe_{0.2})_3O_4$	S	S	S	S	[33]
$[(Bi, Na)_{0.2}(La, Li)_{0.2}(Ce, K)_{0.2}Ca_{0.2}Sr_{0.2}]$ TiO_3	PC	PC	PC	PC	[33]
$(FeCoNiCrMn)_3O_4$	S	S	S	S	[34]
$(MgCoNiZn)_{0.65}Li_{0.35}O$	RS	RS	RS	RS	[35]
$Li_{1.3}Mn_{0.4}Ti_{0.3}O_{1.7}F_{0.3}$	RS	F	RS	F	[36]
LiF	RS	PM	RS	PC	NA
BaTiO3	PC	PC	PC	PC	NA
ZnTiO3	S	S	S	S	NA

Fig. 6. Biplots of HEO compositions as (a) d-valence vs. Ghosh electronegativity χ_{Ghosh}. The Voronoi tessellation of (b) d-valence vs χ_{Ghosh} or further biplots with (c) $\frac{Z}{a}$, or (d)valence electron concentration (VEC) involved. (e) Tabulated Prediction of HEO and non-high-entropy metal oxide compositions for three different χ_{Ghosh} biplots (d-electron, Z/a, and VEC). [99]. (Reproduced). Copyright © 2021 The Author(s).

ligand formation and electron transfer (Fig. 6**(c)**) [99].

Perovskite HEO systems with an increased number of constituent elements have been observed to demonstrate a broadened range of oxygen octahedron distortion and M-O-M angle distribution [56]. The local distortion of crystalline structure with lower symmetry

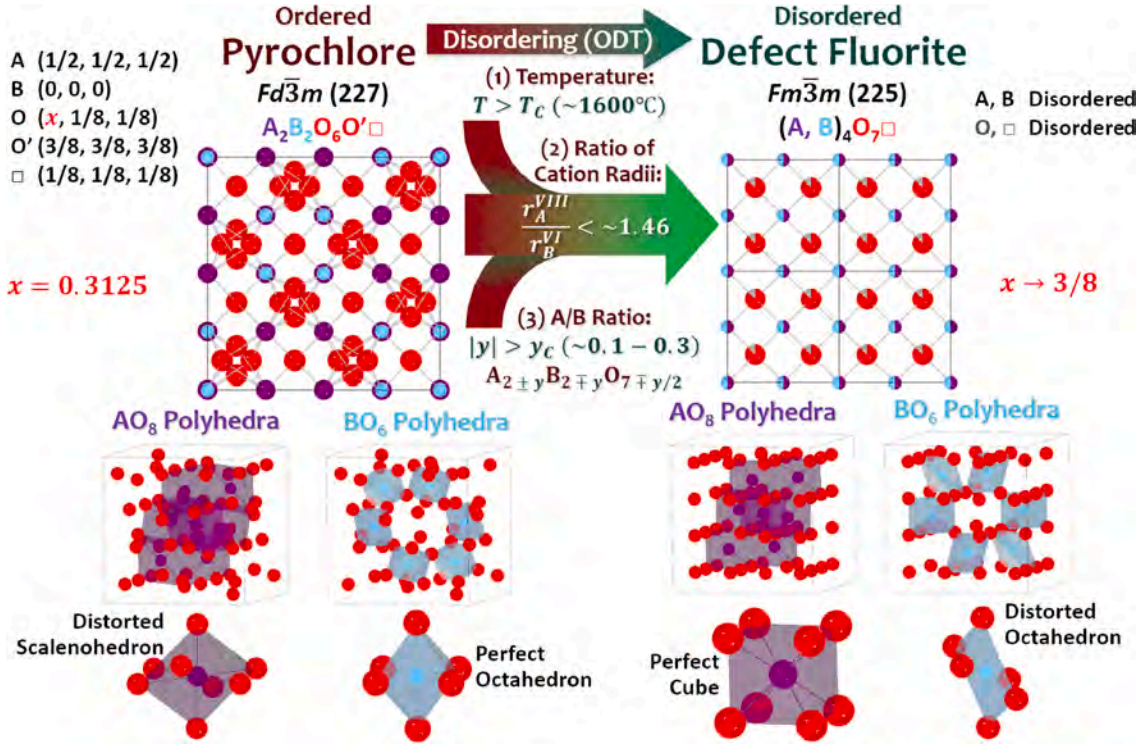

Fig. 7. Schematic illustration of the ordered pyrochlore and disordered defect fluorite structures and the associated order–disorder transition (ODT) [110]. Copyright © 2021 Acta Materialia by Elsevier.

caused by interactions of multi-transition metals in different oxidation states can cause Jahn Teller distortion along with polarization of M−O bonds, reflected as broadening and asymmetric IR vibration bands [100]. Charge compensation mechanism is applied to explain the unique oxidation state of certain metallic elements, usually associated with the presence of oxygen vacancy or the insertion/substitution of new metallic ions [101,102], and thus makes perovskite HEOs mixed ionic-electronic conductive [28,103,104]. The introduction of elemental diversity in different sub-lattice sites and the uneven distribution of certain sub-lattice sites due to non-cubic structures have shown different features in structures. However, further studies are needed. For example, in a tetrahedral $A(BB')O_3$ structure, multiple substitutions can be designed at A, B, and/or B' sites. Specific to A sites, the elongation of the c-axis cell parameter and the tilting of oxygen octahedra may lead to the differentiation of layers with richer and more poorly distributed A sites. Park et al. [105] investigated the effect of introducing more cation types at A sites based on a statistical model focusing on the oxygen vacancy formation energy statistics in mixed cation systems. They revealed a tendency for $AFeO_3$ systems to be more cubic-like with increased oxygen octahedron distortion within the lattices.

2.4.3. *Pyrochlore HEO system*

Compared to the perovskite structure, the pyrochlore structure, denoted by the formula $A_2B_2O_6O'$, is remarkable for its compositional and structural flexibility due to its increased structural complexity. In this structure, A^{3+} cations are coordinated to an oxygen octahedron, B^{4+} cations are coordinated to hexagonal bipyramidal-like oxygen surroundings, and an oxygen vacancy is surrounded by four B^{4+} cations. This complexity facilitates a broad range of possible site substitutions on the A and B sites, enabling numerous technologically significant functionalities, such as energy storage [106], thermal barrier coating [107] and more.

Similar to rocksalt and perovskite HEO systems, some compositions of pyrochlore HEO systems display clustering behavior and Jahn-Teller distortion [108]. While pyrochlore and fluorite structures share identical A and B site positions, the intrinsic presence of oxygen vacancy and different oxygen coordination leads to interesting phase transition phenomena.

For instance, the combination of 3 + and 5 + cations tends to promote local segregation of the pyrochlore phase, which decreases with rising temperature [109]. According to studies by Wright et al. [110], ordered pyrochlore structures can be transferred to disordered defect fluorite structures (Fig. 7). This order–disorder transition (ODT) is not driven by the mixing entropy but is likely driven by the difference in the average radii or the A/B ratio (1.46 ~ 1.78 [58]). During calcination, XRD examinations revealed the coexistence of defective fluorite and crystal pyrochlore structures, with the pyrochlore phase being favored as the temperature increases [111]. Though small in atomic size and 3 + valence, Sc has a strong tendency to occupy B sites and can supply charge balance for other 5 + valence B site occupations [110]. In a study conducted by Jia et al. [112], La^{3+} based high entropy pyrochlore ceramics were designed and synthesized based on valence balance, oxygen octahedron occupation tolerance, and r_A/r_B ratio requirement. Their findings suggest that reducing valence and size disorder can enhance phase formability.

Pyrochlores are not the only anion-deficient fluorite structural derivative oxides. Other derivatives include the special δ-phase oxides and bixbyites, which display a decrease in cation coordination numbers from 7 to 6 (Fig. 8) [113]. The dynamics of defect formation and structure alterations in these oxides are complex. For instance, simple pyrochlores, fluorites, δ-phase and bixbyites are sensitive to the radius of A and B site atoms. Furthermore, the cluster of oxygen Frenkel coupled with a cation antisite pair can drive the

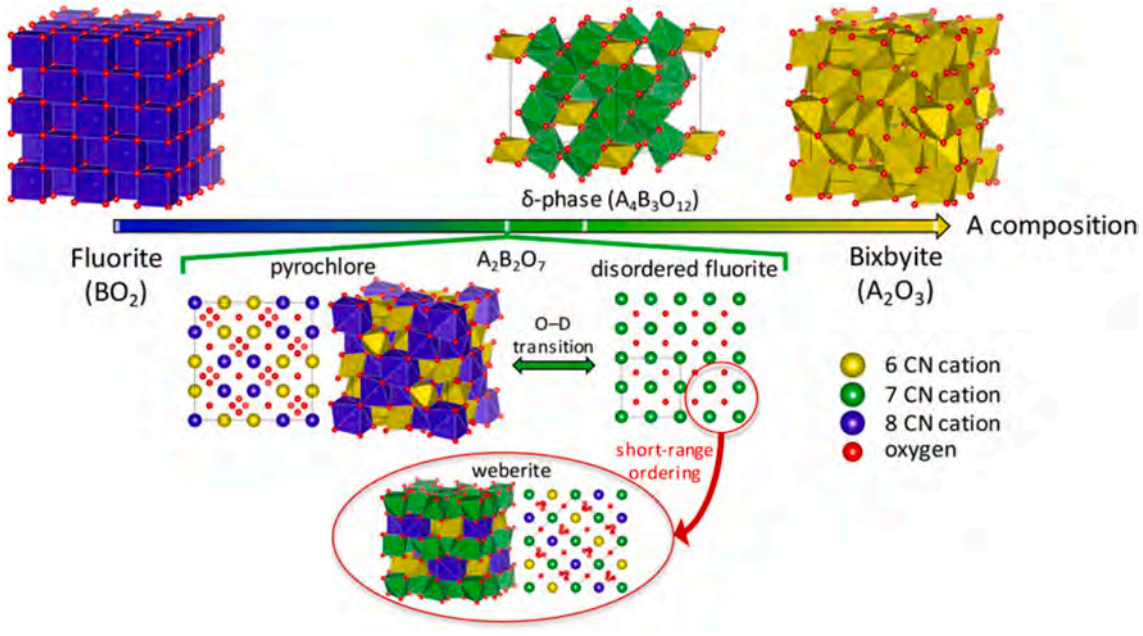

Fig. 8. Schematic representation of the anion-deficient fluorite structural derivative oxides, going from a fluorite (BO_2) to a bixbyite (A_2O_3) crystal structure [113]. Copyright © 2021 The Author(s).

formation of a disordered fluorite structure due to enhanced stability.

Structural transformations can occur through various mechanisms, including isosymmetric, reconstructive, and second-order (or first-order close to second-order) phase transitions [114]. However, studies of these phenomena within the context of corresponding HEO systems are scarce, and further studies are worthy. For example, phase transitions between fluorite-bixbyite [115] and fluorite-pyrochlore [111] structures have been reported. Investigating whether HEO systems follow the same phase transition modes as simple oxides could provide valuable insights.

2.4.4. Spinel HEO system

Spinel structure HEOs are widely applied in catalysis, magnetism, supercapacitors, and lithium battery electrodes. Spinel structure, with the general formula AB_2O_4, has two types of cation sites (A and B) that occupy two types of interstitial sites: tetrahedral and octahedral coordination formed by oxygen atoms. Furthermore, spinel structures can be classified into two main types: normal and inverse spinel structures. For a normal spinel structure, the divalent A-type cations occupy the tetrahedral sites, and the trivalent B-type cations occupy the octahedral sites. While for an inverse spinel structure, half of the trivalent B-type cations occupy the tetrahedral sites, and the remaining trivalent and divalent cations share the octahedral sites. The distribution of cations between the tetrahedral and octahedral sites can vary depending on the material and the degree of inversion depends on factors such as temperature, pressure, and the specific elements involved, thus creating abundant interactions among cations and anions while maintaining structure stability [116,117]. For spinel HEOs, the increased diversity of elements at the cation sites enhances the interactions between electron charge and spin, leading to more complex and tunable electronic, electrochemical and magnetic properties. Spinel oxides can thus be tuned seamlessly from the low-entropy to the high-entropy regime, making this an ideal platform for entropy engineering [71]. Furthermore, the random distribution of cations across tetrahedral and octahedral sites affects the inversion degree, which is critical for determining its electronic properties and catalytic activity [118].

A case study of a series of spinel HEOs nanofibers with a granular architecture and oxygen-deficient surface under calcination at 500 or 600 °C was based on (Cr,Mn,Fe,Co,Ni), (Cr,Mn,Fe,Co,Zn) and (Cr,Mn,Fe,Ni,Zn) combinations. Samples showed a preference for Co and Ni to occupy octahedral sites instead of Zn [118]. According to the study on high entropy ferrite by Doeff et al., Zn^{2+} typically prefers tetrahedral sites due to its electronic configuration, and Mg^{2+} and Fe^{2+} are often found in tetrahedral sites as well. While for the octahedral sites, a mix of cations with varying oxidation states and sizes are occupied [119].

Furthermore, it is worth noting that local elemental variation has a significant effect on the electron structures, which can be reflected in fields of electrochemistry. Via applying an impurity model, Baek et.al[120] demonstrated that the Co, Cr, and Fe sites in $(Co,Fe,Ni,Cr,Mn)_3O_4$ exhibited varying levels of catalytic activity depending on the surrounding metal atoms. Combined experimental results showed that microstrains in material structures play a crucial role in influencing oxygen evolution reaction (OER) activity [120]. The synergetic effect of multi element can realize a narrower band gap than any of the individual oxides due to the alignment of the band structures as well as intermediate band formation [121].

Among reported research results, high entropy oxides can be classified into several groups according to crystal structures, as shown in Table.1. Compared to ordinary oxides, high entropy oxides show a preference for higher symmetry and thus most high entropy oxides follow cubic structures with *fcc* packing.

3. Synthesis and structural characterization of HEOs

3.1. Synthesis of HEOs

Several synthesis strategies for high entropy HEOs have been reported to date, including solid state reaction, pulsed laser deposition (PLD), spark plasma sintering (SPS), co-precipitation, sol–gel method, nebulized spray pyrolysis (NSP), hydrothermal method, and metal-organic frameworks (MOFs) templates technique (Fig. 9). In addition, chemical synthetic routes can be complemented with mechanical processes, such as mechanochemical synthesis. While the majority of research predominantly introduces 5 elements to specific sub-lattice sites, recent developments have expanded this to include more than 5 elements. This development demonstrates an increased availability of flexible composition control [148] and underlines the need for continued advances in synthesis methods.

Solid state reaction synthesis is a prevalent method for fabricating bulk HEOs. Highly pure metal oxides with high purity are processed in equimolar stoichiometric quantities and grounded into powders. These powders are then subjected to a mechanical grinding process, followed by long-time heat treatments (typically 10–24 h [149]) at high temperatures (vary from 1000 to 1500°C [150,151]). The powdered materials are sintered in a furnace with a controlled atmosphere. The mechanical grinding aids in achieving a homogeneously random distribution of cations, while the subsequent heat treatment facilitates the crystallization process. The use of raw materials with similar crystal structures, along with phase transitions occurring with rising temperatures, aids ion diffusion and helps prevent the formation of secondary phases. To ensure the success of the process, several annealing steps with multiple intermediate milling steps, are typically required.

The spark plasma sintering (SPS) method is known for its application of pulsed or unpulsed direct current (DC) or alternating current (AC). It typically allows for high heating and cooling speeds, resulting in dense materials [152]. Flash sintering, another method that produces dense materials, uses lower heating temperature combined with an applied electric field. Flash SPS (FSPS) technique, a hybrid of flash sintering and SPS method, enables rapid densification of more conductive materials at lower temperatures. This technique has been applied in the synthesis of HEOs such as $(Mg, Co, Ni, Cu, Zn)_{1-x}Li_xO$ (less than 4 min at 25°C) [153]. Another hybrid method, reactive flash sintering (RFS), which combines reactive sintering and flash sintering, has also been applied in the synthesis of HEOs like $(La_{0.2}Nd_{0.2}Sm_{0.2}Eu_{0.2}Gd_{0.2})_2Zr_2O_7$ (densities up to 99 % at a furnace temperature of 1200°C) [154] and Sr

Table 1
Typical HEO systems and the corresponding main synthesis methods.

Crystal structures	Symmetry	Typical studied systems	Synthesis methods	References
Rock-salt	Fm-3 *m*	$(Mg_{0.2}Co_{0.2}Cu_{0.2}Ni_{0.2}Zn_{0.2})O$	Solid state reaction	[2]
			Reverse co-precipitation & Hydrothermal (HT) method (nanoparticles)	[122]
		$(Co_{0.2}Cu_{0.2}Mg_{0.2}Ni_{0.2}Zn_{0.2})O$	Nebulized spray pyrolysis (NSP) method	[123]
	–	$(Mg_{0.2}Co_{0.2}Ni_{0.2}Cu_{0.2}Zn_{0.2})O$	Pulsed laser deposition(PLD)	[124]
		$LiCr_{1/6}Mn_{1/6}Fe_{1/6}Co_{1/6}Ni_{1/6}Cu_{1/6}O_2$		[6]
		$(Co_{0.2}Ni_{0.2}Cu_{0.2}Mg_{0.2}Zn_{0.2})O$		[125]
Fluorite	Fm-3 *m*	$(Ce_{0.2}Zr_{0.2}Hf_{0.2}Sn_{0.2}Ti_{0.2})O_2$	Solid state reaction	[126]
		$(Ce_{0.2}Hf_{0.2}Y_{0.2}Pr_{0.2}La_{0.2})O_{2-\delta}$		[127]
		$(Hf_{0.25}Zr_{0.25}Ce_{0.25})(Y_{0.125}M_{0.125})O_{2-\delta}$ (M = Yb, Ca, Gd)	Spark plasma sintering(SPS) method	[128]
		$(Hf_{0.2}Zr_{0.2}Ce_{0.2})(Y_{0.2}M_{0.2})O_{2-\delta}$ (M = Yb, Gd)		
		$(Ce_{0.2}La_{0.2}Pr_{0.2}Sm_{0.2}Y_{0.2})O_{2-\delta}$	NSP method	[84]
	P42/mnm	$(Al_{0.19}Cr_{0.13}Nb_{0.19}Ta_{0.30}Ti_{0.19})O_2$(thin film)	Reactive direct current (DC) magnetron sputtering	[129]
Perovskite	Pm-3 *m*	$Sr(Zr_{0.2}Sn_{0.2}Ti_{0.2}Hf_{0.2}M_{0.2})O_3$, (M = Mn, Nb)	Solid state reaction	[55]
		$(Bi_{0.2}Na_{0.2}K_{0.2}Ba_{0.2}Ca_{0.2})TiO_3$	Flash-sintering	[130]
		$Sr(Ti_{0.2}Fe_{0.2}Mo_{0.2}Nb_{0.2}Cr_{0.2})O_3$	Solid state reaction	[131]
	P4mm	$(Bi_{0.2}Na_{0.2}K_{0.2}La_{0.2}Sr_{0.2})TiO_3$	Modified citrate acid method	[132]
	Pbnm	$(Gd_{0.2}La_{0.2-x}Sr_xNd_{0.2}Sm_{0.2}Y_{0.2})$ $(Co_{0.2}Cr_{0.2}Fe_{0.2}Mn_{0.2}Ni_{0.2})O_3$ (x = 0 and x = 0.2)	Mechanochemical synthesis (Ball milling and modified Pechini method)	[133]
	Pnma	$(Gd_{0.2}Nd_{0.2}La_{0.2}Sm_{0.2}Y_{0.2})CoO_3$	Modified coprecipitation hydrothermal method	[134]
	–	$(La_{0.2}Pr_{0.2}Nd_{0.2}Sm_{0.2}Eu_{0.2})NiO_3$	PLD & Reflection high-energy electron diffraction (RHEED)	[135]
Spinel	Fd-3 *m*	$(Cr_{0.2}Mn_{0.2}Fe_{0.2}Co_{0.2}Ni_{0.2})_3O_4$	Solid state reaction	[136]
		$(Fe,Ni,Co,Cr,Cu)_3O_4$	Metal-organic frameworks (MOFs) templates technique	[137]
		$(Mg_{0.2}Ti_{0.2}Zn_{0.2}Cu_{0.2}Fe_{0.2})_3O_4$	Facile one-step solid state reaction method and subsequent high-energy ball-milling	[138]
		$NiFe_{1.9}(Dy_{0.02}Er_{0.02}Gd_{0.02}Ho_{0.02}Tb_{0.02})O_4$, $(Co_{0.2}Cr_{0.2}Fe_{0.2}Mn_{0.2}Ni_{0.2})Fe_2O_4$ $(Co_{0.2}Cr_{0.2}Fe_{0.2}Mn_{0.2}Ni_{0.2})Fe_{1.9}(Dy_{0.02}Er_{0.02}Gd_{0.02}Ho_{0.02}Tb_{0.02})O_4$	Sol-gel method	[139]
		$(Cr_{0.2}Fe_{0.2}Mn_{0.2}Ni_{0.2}Zn_{0.2})_3O_4$, $(Cr_{0.2}Fe_{0.2}Mn_{0.2}Co_{0.2}Zn_{0.2})_3O_4$ (nanocrystalline powders)	Solution combustion synthesis (SCS)	[140]
Pyrochlore	Fd-3 *m*	$(Gd_{1/7}Eu_{1/7}Sm_{1/7}Nd_{1/7}La_{1/7}Dy_{1/7}Ho_{1/7})_2Zr_2O_7$	Solid state reaction	[58]
		$(La_{1/5}Nd_{1/5}Sm_{1/5}Eu_{1/5}Gd_{1/5})_2Zr_2O_7$		[76]
		$(La_{0.2}Y_{0.2}Gd_{0.2}Nd_{0.2}Sm_{0.2})Zr_2O_7$	Glycine nitrate procedure (GNP)	[141]
		$(Sm_{0.19}Yb_{0.19}Gd_{0.19}Er_{0.19}Dy_{0.19}U_{0.05})_2Ti_2O_7$	SPS method	[142]
	Imma	$Nd_2(Ta_{0.2}Sc_{0.2}Sn_{0.2}Hf_{0.2}Zr_{0.2})_2O_7$	Solid state reaction	[108]
Bixbyite	Fm3m	$(Y\text{-}La\text{-}Ce\text{-}Nd\text{-}Gd)_2O_{3+\beta}$	Mechanochemical synthesis (ball milling and modified sol–gel method)	[143]
	Ia-3	$Gd_{0.4}Tb_{0.4}Dy_{0.4}Ho_{0.4}Er_{0.4}O_3$	Polymeric steric entrapment method	[144]
Magnetoplumbite	–	$Ba(Fe_6Ti_{1.2}Co_{1.2}In_{1.2}Ga_{1.2}Cr_{1.2})O_{19}$	Solid state reaction	[5]

(*continued on next page*)

Table 1 (*continued*)

Crystal structures	Symmetry	Typical studied systems	Synthesis methods	References
O3-type layered	R − 3 *m*	$NaNi_{0.25}Mg_{0.05}Cu_{0.1}Fe_{0.2}Mn_{0.2}Ti_{0.1}Sn_{0.1}O_2$ $NaNi_{0.12}Cu_{0.12}Mg_{0.12}Fe_{0.15}Co_{0.15}Mn_{0.1}Ti_{0.1}Sn_{0.1}Sb_{0.04}O_2$	Solid state reaction	[145] [146]
Layered Ruddlesden–Popper (RP)	–	$(La_{0.2}Pr_{0.2}Nd_{0.2}Sm_{0.2}Eu_{0.2})_2CuO_4$	PLD	[7]
Hexaaluminates	–	$(La_{0.2}Nd_{0.2}Sm_{0.2}Eu_{0.2}Gd_{0.2})MgAl_{11}O_{19}$	Solid state reaction	[81]
Mullite	Pbam	$Bi_2M_4O_9$ (M = Ga, Al, Fe, Mn), $(Er_{0.2}Y_{0.2}Sm_{0.2}Nd_{0.2}Eu_{0.2})_2Mn_4O_{10}$, $(Er_{0.2}Y_{0.2}Sm_{0.2}Nd_{0.2}Bi_{0.2})_2Mn_4O_{10}$, $(Eu_{0.2}Y_{0.2}Sm_{0.2}Nd_{0.2}Bi_{0.2})_2Mn_4O_{10}$, $(Ce_{0.2}Y_{0.2}Sm_{0.2}Nd_{0.2}Bi_{0.2})_2Mn_4O_{10}$,	Sol-gel method	[147]

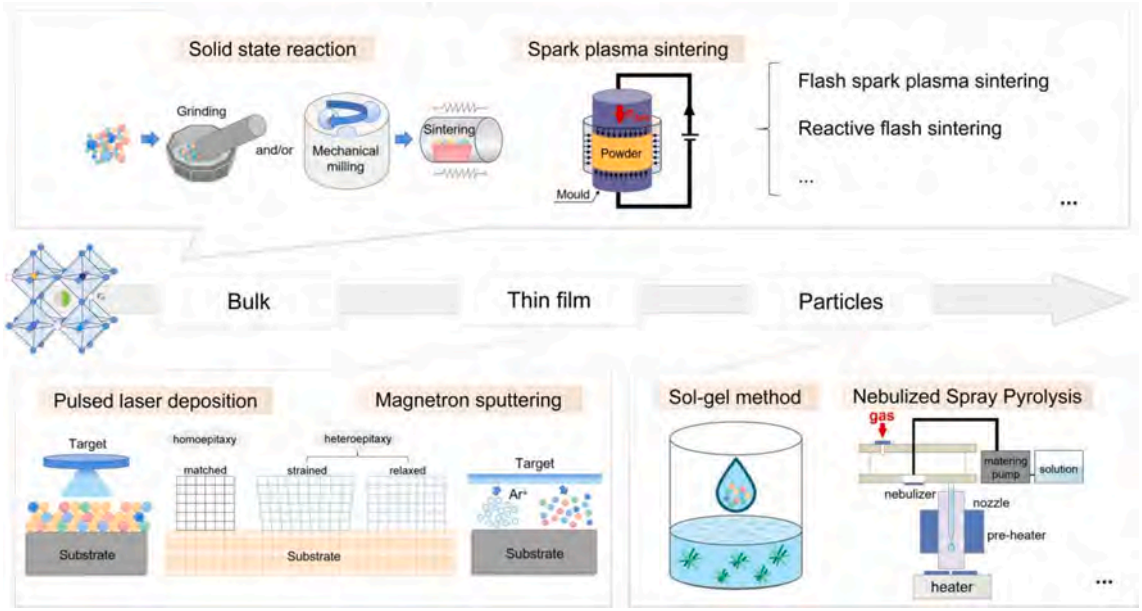

Fig. 9. The summary sketch of HEO synthesis.

$(Ti_{0.2}Y_{0.2}Zr_{0.2}Sn_{0.2}Hf_{0.2})O_{3-x}$ (at 1314°C and 1 min) [155].

Besides the methods mentioned above, solution-based chemical synthetic routes have also been developed to deal with new emerging requirements of sample quality and morphology. For instance, the nebulized spray pyrolysis (NSP) method shows great advantage in synthesizing nanoparticles with high flexibility in controlling microstructures (i.e., particle sizes and morphologies), which is believed to be suitable for lab scale synthesis for its quick single-step process. NPS method requires precursor salt solution of the respective metals dispersed into fine droplets by an ultrasonic nebulizer. The resulting mist is transferred to a hot-wall reactor through a carrier gas (e.g. N_2 and O_2) and forms complex compounds, which is finally collected on a filter paper in a heated collector to prevent water vapor from condensing on the powders [156,157]. Besides, precipitation methods have been applied, including co-precipitation [158] and reverse co-precipitation [115,157]. Salt precursors are dissolved in solutions and precipitated with the addition of an alkaline solution for co-precipitation process while a salt precursor solution drops into an alkaline solution for reverse co-precipitation process.

Among numerous solution-based chemical synthetic routes developed, the conventional simple sol–gel method, heating-assisted method and hydrothermal method can also be employed for synthesizing HEOs. Pechini method is a type of sol gel method dealing with systems involving multiple cations (e.g. perovskites) and utilizing a chelating agent(typically choose citric acid) [133]. Complex topological structures can be achieved via sol-gel process, such as spherical mesoporous spinel Ni-Co-Cr-Fe-Mn oxide [159] and nanometer-scale porous spinel $(Cr_{0.2}Fe_{0.2}Co_{0.2}Ni_{0.2}Zn_{0.2})_3O_4$ [160]. Colloidal synthesis by Sun et al. [161] demonstrated surface-confined HEO atomic layers, where transition metals are randomly substituted, embedded and stabilized on the surface lattice of CeO_2 nanoparticles (denoted as CuCoFeNiMn-CeO_2). Moreover, flame-assisted PS (FPS) method combines high temperature flames into the condensation procedure of metal salt liquid precursors and the homogeneity of nanoparticles can be optimized by tantalizing the combustion enthalpy density of the flame [162]. The FPS technique is reported to be advantageous in possessing very high phase purity and higher specific surface area compared with hydrothermal, co-precipitation, ultrasonic spray pyrolysis, and sol–gel methods [163]. Synthesis of $(Mn, Fe, Ni, Cu, Zn)_3(O)_4$ nanoparticles via FPS method have been reported [164]. Very recently, new emerging rapid Joule heating is emerging as an effective approach to thermally decompose precursors and form HEOs with multiple active sites and continuous electrical structures in a rapid and high throughout way [165]. Similar to the sol-gel method that relies on the reaction of precursors, the hydrothermal method heats aqueous metal salt precursor solution under certain temperature and pressure condition and produces HEO powders after calcination treatment. Microwave synthesis can be combined with this method to save the time and the energy required before calcination [166]. Similar to this process of preparing precursor solution, following the procedure of aging and several times of spin coating and baking and pyrolysis, a hundred-nanometer level, rather textured thin film can be produced after rapid thermal annealing [167].

Based on the above solution-based synthesis methods, the introduction of metal–organic frameworks (MOFs) as sacrificial templates provides a new low-temperature route to obtain nanostructured HEOs with large surface area, abundant active sites and rich oxygen vacancies which showed intrinsically high electrochemical activities for applications in catalysis [137] and lithium batteries [168].

Beyond the previously mentioned synthesis methods, epitaxial thin film growth methods have begun to contribute to the development of new forms of HEOs. Pulsed laser deposition (PLD) has been used to synthesize rocksalt HEOs, such as polycrystal $(Co_{0.2}Ni_{0.2}Cu_{0.2}Mg_{0.2}Zn_{0.2})O$ [124] and single crystal $LiCr_{1/6}Mn_{1/6}Fe_{1/6}Co_{1/6}Ni_{1/6}Cu_{1/6}O_2$ [6]), as well as a series of perovskite HEOs

including single crystal $LaCr_{0.2}Mn_{0.2}Fe_{0.2}Co_{0.2}Ni_{0.2}O_{3-\delta}$ [169] and RP phase $(La_{0.2}Pr_{0.2}Nd_{0.2}Sm_{0.2}Eu_{0.2})_2CuO_4$ [7]. Reactive magnetron sputtering of the powder-metallurgically prepared target has also been employed to produce $(Al_{0.19}Cr_{0.13}Nb_{0.19}Ta_{0.30}Ti_{0.19})O_2$ [129] and $(Cr\text{-}Mn\text{-}Fe\text{-}Co\text{-}Ni)_3O_4$ [170] coating on Si substrate.

The PLD equipped with reflection high-energy electron diffraction (RHEED) can monitor real-time surface atomic growth layer by layer, enabling the realization of a more precise oxide structure than other synthesis methods. This paves the way for further studies of atomic defects, nano-level ferroelectricity [171] and more. For epitaxial growth of a single crystal thin film, an appropriate substrate with a single orientation and lattice mismatch within 5 % should be chosen. The lattice parameter difference between substrate and grown HEOs affects lattice strain and thereby influences material properties. The crystallinity of HEO thin film is strongly related to several parameters, including oxygen partial pressure, laser fluence, laser spot size and target-substrate distance. The range of these parameters, which allow for fine RHEED oscillation modes, varies between different material systems.

Synthesis methods and specific technological parameters are crucial factors that dictate the structure of HEOs, as well as the control over particle-size distribution and morphologies. These factors, in turn, influence structure–property behaviors. For example, Sakar et al. [115] synthesized $(Ce_{0.2}La_{0.2}Pr_{0.2}Sm_{0.2}Y_{0.2})O_{2-\delta}$ samples using reverse co-precipitation (RCP) techniques and and achieved a reversible change in the bandgap energy via heat treatment of under a vacuum atmosphere, followed by reheat treatment in air. Krawczyk et al. [134] demonstrated the possibility of fine tuning of the semiconducting band gap via a subtle change in A-site stoichiometry. They achieved this by using a modified co-precipitation hydrothermal process to synthesize $(Gd_{0.2}Nd_{0.2}La_{0.2}Sm_{0.2}Y_{0.2})CoO_3$ under original quenching conditions, with liquid nitrogen serving as the medium. Regardless of whether advanced solution-based routes or plasma sintering routes are employed, the ultimate goal is to produce high quality HEO samples with excellent atomic level mixing and high purity, while also reducing the synthesis temperature.

3.2. *Experimental techniques for structure characterization*

Various experimental techniques have been instrumental in understanding structural order and disorder in different scales. To this end, characterization techniques are more focused on local atomic structures rather than extensive structures, which are typically tested by traditional characterization methods. Therefore, the analysis of correlations between obtained structural information and properties is conducted.

Despite relatively adequate research on correlating experimental characterization data and atomic structure configurations of HEAs, the understanding and control of local order/disorder in HEOs remains a substantial challenge. To what extent and range does the disorder present some degree of order still need further investigations. Also, it is crucial to determine whether a universally applicable rule for atomic arrangement exists within specific material systems, as this has significant implications for the design and development of materials with targeted structures. The typically used experimental characterization techniques for HEOs are summarized in Fig. 10.

(1) X-ray diffraction (XRD) and neutron scattering

XRD is a widely applied characterization method in analyzing and tracking crystal structures (including corresponding symmetries), phase transitions under different conditions (e.g. pressure [172,173] and heat-treatment [96]), and determining the formation

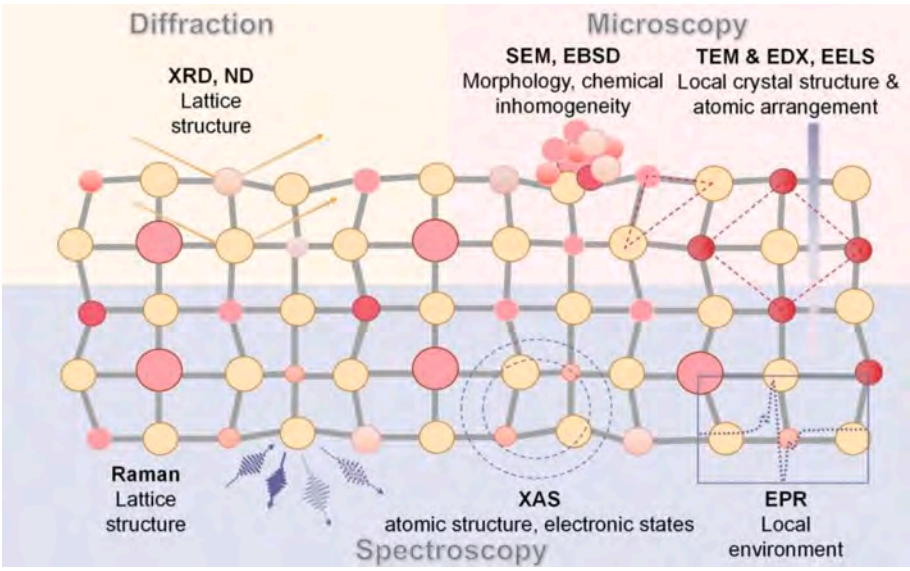

Fig. 10. The summary sketch of experimental characterization for HEOs.

of single stabilized phases (Fig. 11). Crystal structures can be obtained via Rietveld refinements. The pair distribution function (PDF), which can be extracted from XRD and neutron scattering data, provides information on the local short-range order of M−site cations (this applies to its Fourier transformed form, Structure factor $S(q)$). Both PDF and $S(q)$ can also be extracted from neutron scattering data. The analysis of the local atomic environment mainly focuses on reflecting the randomness of element distribution. Jiang et al [108] studied an example of $Nd_2M_2O_7$ with five M−site cations via neutron diffraction and investigated local atomic structure via PDF analysis. The identified sub-nanometer scale local TiO_6 octahedral distortion and some degree of short-range Ti clustering were identified in the $Nd_2(Ti_{0.2}Nb_{0.2}Sn_{0.2}Hf_{0.2}Zr_{0.2})_2O_{7+x}$ compound, while the $Nd_2(Ta_{0.2}Sc_{0.2}Sn_{0.2}Hf_{0.2}Zr_{0.2})_2O_7$ compound demonstrated highly nanoscale homogeneity of cation distribution. Meanwhile, Cheng et al. studied the structural evolution of fluorite HEO $(Ce_{0.2}La_{0.2}Pr_{0.2}Sm_{0.2}Y_{0.2})O_{2-\delta}$ via *in situ* high-pressure synchrotron XRD measurements and extracted different $S(q)$ and PDF during compression and decompression at room temperature [173].

With the assistance of synchrotron radiation, *in situ* XRD can further provide detailed information about the structural evolution under external perturbations (e.g., electric field/ thermo-field) and certain atmospheres. Ding et.al. [175] developed an O3-type oxide cathode composed of all-3*d* transition metals (TM), $NaNi_{0.3}Cu_{0.1}Fe_{0.2}Mn_{0.3}Ti_{0.1}O_2$ (NCFMT) and $(NaNi_{0.3}Cu_{0.1}Fe_{0.2}Mn_{0.3}Sn_{0.1}O_2$ (NCFMS), which replaces Ti with Sn in TMO_2 slabs., to conduct a rational research on material design. The NCFMS exhibited a larger full-width at half-maximum in peaks with more a-b axis character (larger angle to the (003) plane) when compared with the (00 l) diffraction peaks (Fig. 12 (**a**)), and a higher lattice strain within the *ab* plane (0.51 %) than between the *ab* planes (0.15 % along the *c* axis) (Fig. 12 (**b**)), compared to the NCFMT. These results indicated that the NCFMS has a stronger interaction between TM ions than that between TM ions and Na^+, and thus an enhanced cation displacement from high-symmetry sites (Fig. 12 (**c**)). The *in situ* XRD revealed that the NCFMT and NCFMS went through similar phase transition from O3 to P3 and lastly O3, as shown in Fig. 12 (**d**). Besides, during Na^+ deintercalation, the (003) peaks shifted toward lower angles in the low-voltage regions, likely due to the repulsion between the oxygen planes that corresponds to an expansion of the *c* lattice parameter. The (1 0 1) and (012) peaks shift to higher angles as active TM oxidation causes a reduction of the TM-O bond and a contraction of the *a/b* lattice parameter.

(2) Electron microscopy and techniques assembled

Transmission electron microscopy (TEM) and scanning electron microscopy (SEM) are widely applied characterization techniques in phase identification and morphology/structure analysis. TEM is advantageous in projecting 2D imaging of inner structure and testing minute samples which are unavailable via XRD. Based on TEM, high-resolution TEM (HRTEM) is developed and produces directly perceived images with higher resolution (~1 nm) and higher sensitivity to chemical compositions. The high-angle annular dark-field scanning transmission electron microscopy (HAADF-STEM, also called Z-contrast imaging) demonstrates an incoherent high-resolution image whose element-related contrast does not change significantly with the thickness of the sample and the focus of

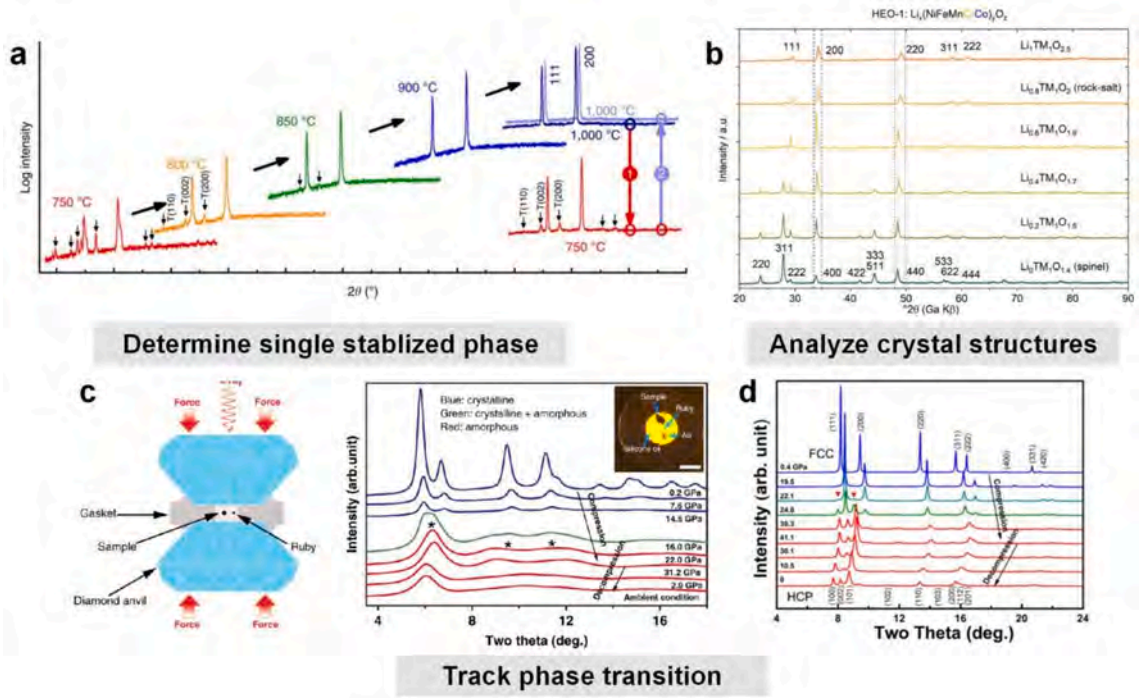

Fig. 11. The application of XRD technique on structure analysis of HEOs in (a) determining single phase stabilization during formation [3], (b) analyzing crystal structures [174], (c) and (d) tracking phase transtion under different conditions (e.g. pressure) [172,173] (Reproduced). Copyright © 2015, 2019 and 2020 The Author(s).

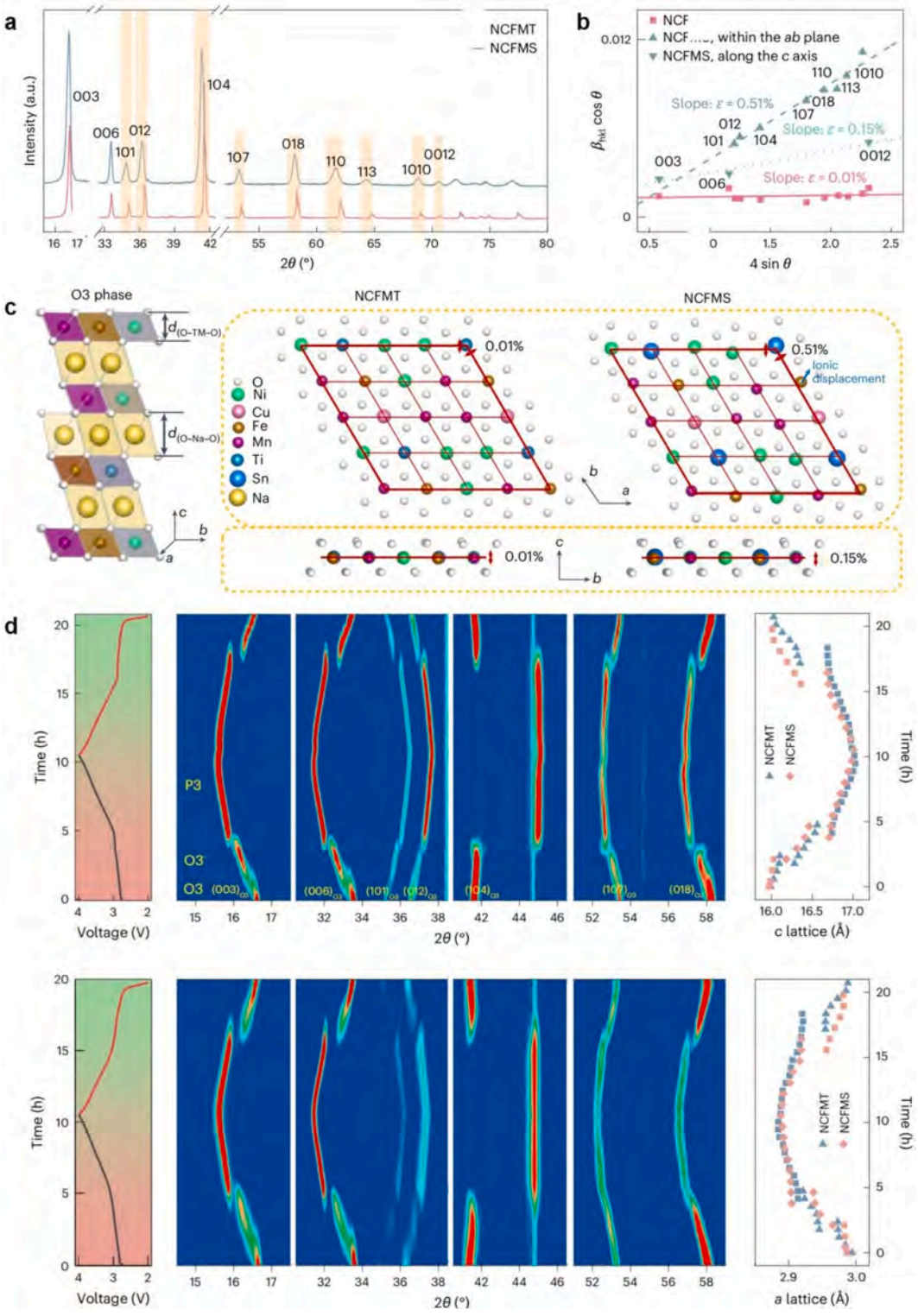

Fig. 12. A case study applying XRD and *in situ* X-ray synchrotron imaging. (a) XRD patterns of NCFMT and NCFMS. a.u., arbitrary units. (b) Independent lattice strain ε fitting based on Williamson-Hall analysis, where strain distribution within the ab plane is plotted in dashed line and between the *ab* planes is plotted in dotted line. (c) Structure illustration of O3 phase and sketch of strain distribution and ionic displacement for NCFMT and NCFMS. (d) *In situ* XRD patterns of NCFMT and NCFMS during first charge and discharge. All reproduced from [175]. Copyright © 2024 Springer Nature.

the objective lens. HAADF-STEM is less sensitive to detect light elements, which could be masked by the strong contrast of heavy elements. Correspondingly, ABF-STEM (where ABF is short for "annular bright-field") can realize the simultaneous observation of both light and heavy elements but its imaging contrast is affected by the sample thickness and the under-focus [176]. Spherical error correction could improve the sensitivity down to the sub-angstrom scale, making atomic imaging available [177,178]. Alongside TEM and STEM, additional techniques including selected area electron diffraction (SAED), energy dispersive X-ray analysis (EDX), and electron energy loss spectroscopy (EELS) can provide further information of crystallinity, composition, and morphology, etc. SEM, on the other hand, is particularly effective for providing 3D imaging of sample surface, making it valuable for characterizing microstructures such as fracture, corrosion, grains, and grain boundaries. Additionally, SEM can be integrated with advanced techniques like EDS and Electron backscatter diffraction (EBSD).

As a crystallographic experimental technique facilitated by TEM, SAED provides a diffraction pattern to determine the crystallinity, and each diffraction spot corresponds to certain lattice planes of crystal structures, indicating crystal structures of HEOs [179]. Besides, the metal nuclei grown during the lithiation process are smaller in size than the X-ray coherence length and thus are visible only by SAED [180]. Combining *in situ* XRD and *ex situ* TEM approaches (including corresponding SAED), Zheng et al. [181] explored the lithium storage behavior of the $(FeNiCrMnMgAl)_3O_4$ spinel high entropy oxide as anodes for LIBs and confirmed the reversible spinel to rock salt phase transformation phenomenon and spinel residue behavior.

Additionally, applied along with TEM or SEM, EDX, referred to as EDS or EDAX, can provide a 2D visualized display of the element distribution in a certain crystal orientation and area of the specimen by the characteristic X-ray intensities. Usually, ESD mapping is not accurate enough for surface characterization since X-rays are generated in a region of about 2 μm in depth [182]. The application of EDX analysis is mostly applied to demonstrate the highly homogeneous dispersion of multi-elements at cations [3,149,183,184]. Combining HAADF-STEM and EDS elemental maps, an atomic resolution micrograph of each elemental arrangement from a certain zone axis can be obtained. Compositional fluctuation can be extracted from integrating the spot brightness of the atomic EDS mapping micrograph after locating site centers and atomic radius through two-dimensional (2D) Gaussian fitting. Oxygen polyhedron distortion can be further counted (Fig. 13) [56]. EELS can also acquire high-resolution atomic level elemental/chemical mapping and what's more, provide additional bonding and oxidation state information [185]. The EELS study of Phakatkar et al. suggested that the oxidation states for each of the metallic elements of (Mn, Fe, Ni, Cu, Zn)$_3O_4$ varied considering their respective coordination with oxygen element and possibly with the neighboring metal cations [186]. Through investigation of HEOs from unary to quaternary entropy oxide, the quality of certain HEO systems (e.g. the chemical affinity between each element and the electronic behaviors of each

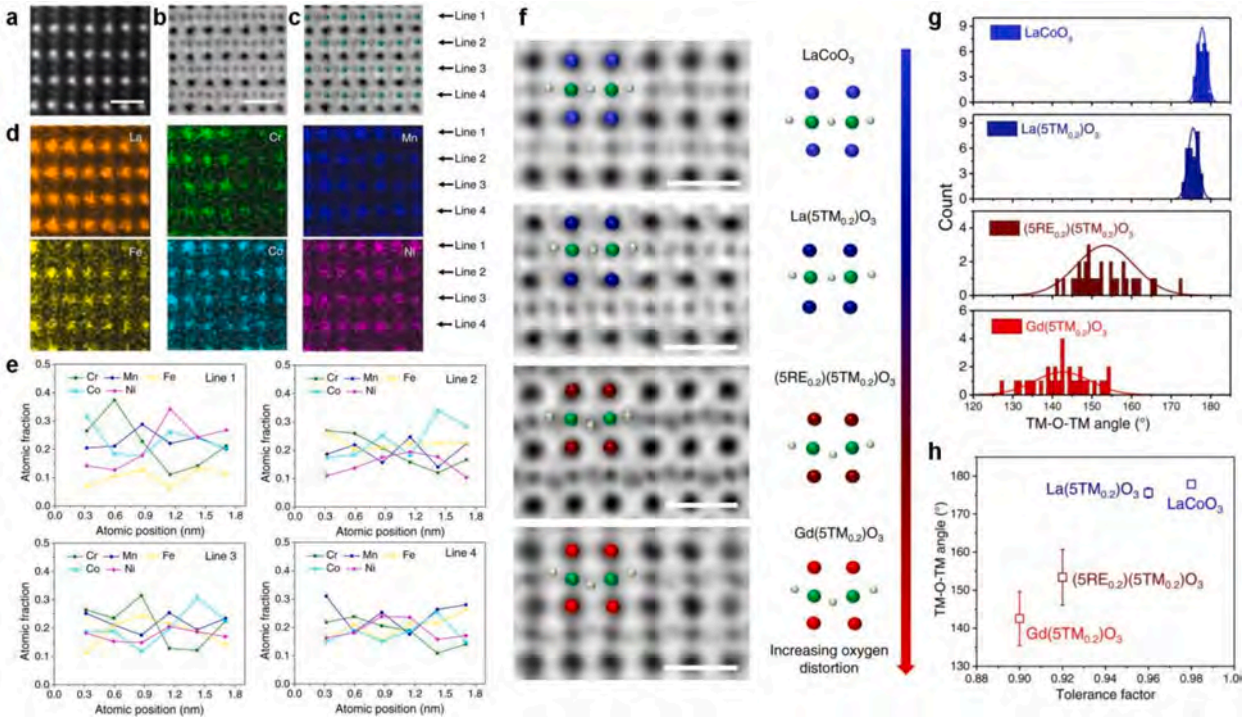

Fig. 13. Composition and oxygen octahedron distortion analysis of HEOs from HAADF/ABF-STEM and EDS mapping, focusing on a series of sample including $La(5TM_{0.2})O_3$, $Gd(5TM_{0.2})O_3$,and $(5RE_{0.2})(5TM_{0.2})O_3$.(RE = rare earth elements, TM = transition metal elements) (a) HAADF-STEM, (b) ABF-STEM, and (c) marked ABF images of $La(5TM_{0.2})O_3$ taken from [110] zone axis and following (d) atomic EDS mapping. (e) TM-O-TM angle extracted from defining atomic positions of ABF-STEM images.(f) the TM-O-TM angle of different samples extracted from ABF images enables (g) TM-O-TM angle distribution, and (h) the relationship between TM-O-TM angle and tolerance factor [56].(Reproduced). Copyright © 2022 The Author(s).

metal cation) can be elucidated.

(3) Advanced analysis based on X-ray Absorption Spectroscopy (XAS)

XAS is a robust and broadly used method in the investigation of atomic local structure as well as electronic states. XAS detects the valence change and can monitor the changes of valence and the transformations of electronic structures during a certain reaction process [180]. Moreover, advanced techniques such as X-ray absorption fine structure (EXAFS) and X-ray magnetic circular dichroism (XMCD). are developed based on XAS, providing precise information on local atomic structures.

EXAFS is a robust technique for characterizing local atomic environment. Compared with TEM which can only show a column of atomic arrangements and STEM which can only detect intensity fluctuation of certain atom arrays, EXAFS can provide information of neighboring atomic shell environment in a larger scale. By comparing the 1st and 2nd shell scattering path lengths of different elements, Rost et al. reported the Cu clustering within the lattice (disorder appeared to average out by 2nd coordination shell) while the homogeneous distribution of other elements, as observed in the EXAFS study of $(Mg_{0.2}Ni_{0.2}Co_{0,2}Cu_{0.2}Zn_{0.2})O$ (Fig. 14) [94]. Additionally, the distortion of oxygen polyhedra can be examined by comparing half-scattering path lengths of the 1st and 2nd neighboring shells between the metal absorber and the six nearest neighboring oxygen atoms [187].

X-ray absorption near-edge structure (XANES) and extended X-ray absorption fine structure (EXAFS) experiments are usually combined to elucidate the chemical states and the atomic coordination structures. XANES focuses on the structure near the absorption edge, while EXAFS explores the fine structure behind the absorption edge [188]. For example, quinary high-entropy ruthenium iridium-based oxide (M-RuIrFeCoNiO_2) was studied via XANES and EXAFS. Ru-K XANES spectra of M-RuIrFeCoNiO_2 and M-RuO_2 are located at the same energy while that of commercial RuO_2 (C-RuO_2) shift to a higher energy relative to that of Ru foil, revealing a Ru^{4+} valence state. The Fourier transform EXAFS also showed a higher Ru-O shell bond length and a lower coordination number (CN) of 4.5 (while the standard CN of RuO_2 is 6) [189]. The charging and discharging process of $Mg_{0.2}Co_{0.2}Ni_{0.2}Cu_{0.2}Zn_{0.2}O$ as the active material in a composite anode for lithium-ion batteries was studied via XANES and EXAFS after assembled in half-cells, revealing the cocktail effect of elemental synergy. The metallic state of Co, Ni and Cu during discharging based on XANES analysis and metal–metal distance matching those of fcc structure Ni, Cu, and Co according to Fourier transformed EXAFS (FT-EXAFS) analysis jointly proved the formation of interconnected nanostructure, enhancing electron transport [190]. The wavelet transformed EXAFS (WT-EXAFS) extends the visualization and interpretation for EXAFS, especially for high and low frequency parts of the EXAFS signal simultaneously [191]. For example, in a study of $La(CrMnFeCoNi)_{0.2}O_{3-x}$ nanowires, the maximum density of the Fe-O bond and Ni-O bond in k space was 4.1 $Å^{-1}$ and 4.2 $Å^{-1}$ respectively, according to WT-EXAFS. Combined with the results of FT-EXAFS, Ni and Fe were atomically incorporated into the B-site of $LaMnO_3$-type perovskite while being coordinated by O atoms.

XMCD is the difference spectrum obtained via two XAS spectra taken with left and right circularly polarized lights respectively in a magnetic field. It is efficient in studying cation site occupancy due to its simultaneous element specificity and crystal field sensitivity. The signal of XMCD is dependent on the d shell holes and XMCD will exhibit an opposite sign between octahedra and tetrahedra sites due to their opposite spins (tetrahedra: negative dichroism). Polyhedron site preference and valence of specific elements can be analyzed via the ligand field multiple theory calculations of each transition metal element sitting on certain polyhedron site and further approximate site occupancy of different polyhedra can be proceeded via linear combinations of the constituent L + R spectra (approximately equivalent to pure XAS measurements), as shown in Fig. 15 [71].

(4) Raman spectroscopy

Raman spectroscopy, a non-destructive detection technique of chemical structures, is robust for its broader applicability for

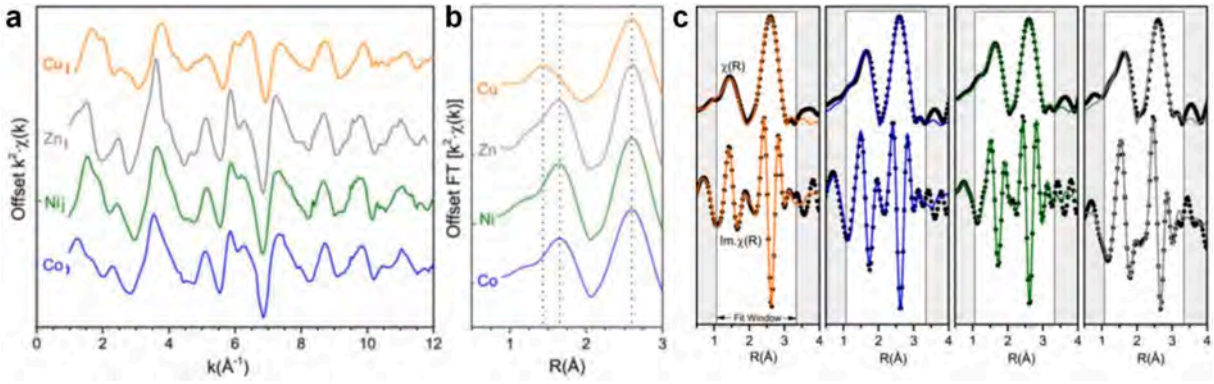

Fig. 14. Local coordination analysis based on EXAFS. (a) $k^2\chi(k)$ EXAFS spectra for Cu, Zn, Ni and Co absorbers in the $(Mg,Co,Ni,Cu,Zn)_xO$ (x = 0.2) composition and (b) FT of $k^2\chi(k)$ between 0.5 and 3.0 Å. (c) Data (Black dots) and fits for the FT of $k^2\chi(k)$, denoted $\chi(R)$, and their respective imaginary parts for Cu (orange), Co (blue), Ni (green), and Zn (grey) [94].(Reproduced) Copyright © 2017 The American Ceramic Society. (For interpretation of the references to colour in this figure legend, the reader is referred to the web version of this article.)

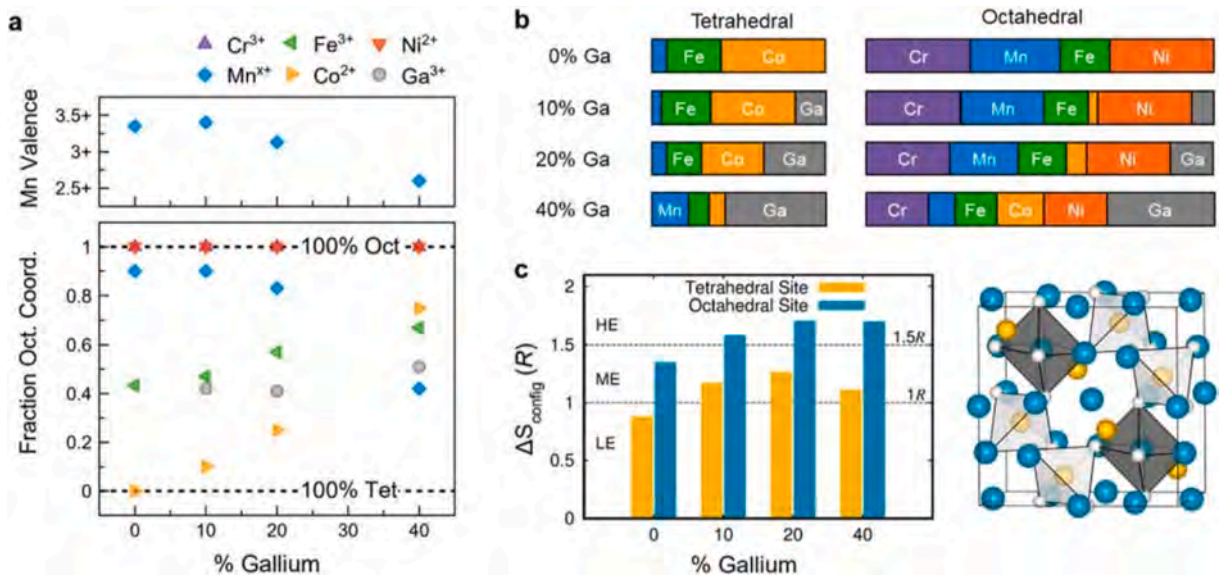

Fig. 15. Local ordering and site selectivity studies of spinel (Cr, Mn, Fe, Co, Ni)$_{3-x}$Ga$_x$O$_4$, including (a) valence of Mn and the fraction of octahedral occupation as a function of Ga concentration, (b) schematic representation of the cation occupation of different polyhedron sites for each sample and (c) calculated sublattice entropy assuming the ideal configurational disorder as a function of Ga concentration [71]. Copyright © 2022 American Chemical Society.

samples in different shapes and sizes. By comparing the main chemical bond modes of HEOs with those of classical transition metal oxides, Raman spectra can reveal the corresponding crystal structures, indicate the trend of crystal symmetry transition, and its surface mapping can be used to confirm phase homogeneity. The substitution of different cations in the equivalent lattice point, defects and crystallite sizes being in the nano regime, etc. will lead to a lowering of the local translation symmetry and thus the presence of new vibration modes which is typically absent in a perfect cubic lattice [192]. Combining the revealed vibration modes and factor group analysis of the corresponding space group, possible distinct polyhedra units within the lattice can be suggested [193]. Additionally, Raman is advantageous in the *in situ* characterization of structural deformation/displacement and phase transition [172,173].

(5) X-band electron paramagnetic resonance(EPR) spectroscopy

X-band EPR spectroscopy utilizes the response of atoms with unpaired electrons to short (ns) pulses of microwave radiation (known as X-band) in a magnetic field and characterize the local environment of transition metal oxides. Berardan et al. [194] conducted X-band EPR experiments of two samples, which are (Mg,Co,Ni,Cu,Zn)$_{0.9}$Li$_{0.1}$O with almost perfect cubic rocksalt structure and (Mg,Co,Ni,Zn)$_{0.74}$Cu$_{0.26}$O with very distorted structure, to confirm the rhombic geometry of Cu ions originated from Jahn-Teller distortion.

(6) Photoemission spectroscopy (PES)

Photoemission spectroscopy (PES), also known as photoelectron spectroscopy, basically studies the binding energies of electrons by electron energy emitted from materials and thus probes the electronic structure and chemical composition. PES includes ultraviolet photoemission spectroscopy (UPS), Angle-resolved photoemission spectroscopy (ARPES) and X-ray photoemission spectroscopy (XPS), etc. For studies of HEOs, mostly applied PES techniques are XPS, which can distinguish between different chemical states of the same element (e.g., different oxidation states), based on shifts in core-level binding energies. XPS is usually combined with XAS, especially in fields of electrochemistry. XPS plays a crucial role in the further interpretation of the XAFS results. A good example of (CrFeCoNi-Mo)$_3$O4 nanosheet by Antink et al. [195] showed the presence of high valence state transition metal ions such as Cr^{6+} and Mo^{6+} via XPS, and as well as the coexistence of lattice oxygen (M-O), defect oxygen (M-OH), and water molecules adsorbed on the surface (H-O-H). The incorporation of high-valence Cr and Mo implied mixed occupancy of both the octahedral and tetrahedral sites, leading to a remarkable increase in configuration entropy and contributing to the formation of a single-phase structure. XAS results revealed a decrease in the O K-edge spectra combined with the increased metal L-edge absorption for Co and Ni indicating a weakening in metal-oxygen covalency, resulting from a redistribution of electron density from Ni and Co to the O sites. Enlarged metal-oxygen bonds in the HEO nanosheets according to FT-EXAFS further validated weakened metal–oxygen covalency. The activated lattice oxygen is thus modulated by inducing the aforementioned partial electron transfer, which is specifically through the bridging oxygen and finally promotes the lattice oxygen mechanism.

4. Structure-property relation of HEOs

Though it is challenging to consider elemental fluctuation and short-range atomic structures, efforts in experimental characterization and computational calculations have proved that HEOs demonstrate not only homogeneous randomized distributions of each element but also complex and flexible structural characteristics depending on compositions in the short range. From structures to certain properties, based on the designing concept of the high entropy strategy, it is natural to consider the relation between aspects of the high entropy effect and specific applications. The general structural features shaped by the configurational disorder bring about intriguing reflections in thermal and electrical properties and thus possess potential in several fields of applications, including thermoelectrics, thermal barrier coating, dielectrics, energy storage, lithium batteries, and catalysis, etc. Furthermore, element-specific structural behaviors in the short range bring about variations in functional performance [196]. The following discussions will summarize major crystal structures of HEOs studied in specific applications, how the high entropy effect facilitates performance enhancement and the effect of certain elements/composition design in structure–property relations. Guidelines for future structure design to demonstrate superior performances will be based on recent advances and progress of HEOs' functionalities.

4.1. Thermoelectric property

Thermoelectrics, which convert heat and electricity without moving parts, is promising in various fields such as 5G electronics, integrated circuits, waste heat collection, temperature sensors, and cooling [197–199]. Thermoelectric oxides are receiving increasing interest due to their element abundance, good thermal and chemical stability and low environmental impact [200–203]. To achieve high thermoelectric power conversion efficiency, measured by the zT values ($zT = \frac{S^2\sigma T}{\kappa_e+\kappa_L}$ [204]), where S is the Seebeck coefficient, σ is the electrical conductivity, and κ is the thermal conductivity), it is necessary to simultaneously optimize high Seebeck coefficient (S), high electrical conductivity (σ), and low thermal conductivity (κ) [205].

Several strategies have been employed to enhance the thermoelectric properties, such as band alignment [206], resonant doping [207], dynamic doping [208], grain boundary engineering [209–211], compositing effect [212,213] and nanostructure design [214,215]. However, the interplay between electrical and thermal transports limits the further property optimization, necessitating new concepts in this field. Since high entropy ceramics were first explored in 2015 [3], entropy engineering has been utilized in multiple fields of ceramics due to numerous useful effects from high entropy [59,17,16,216]. Four aspects of the high entropy effect

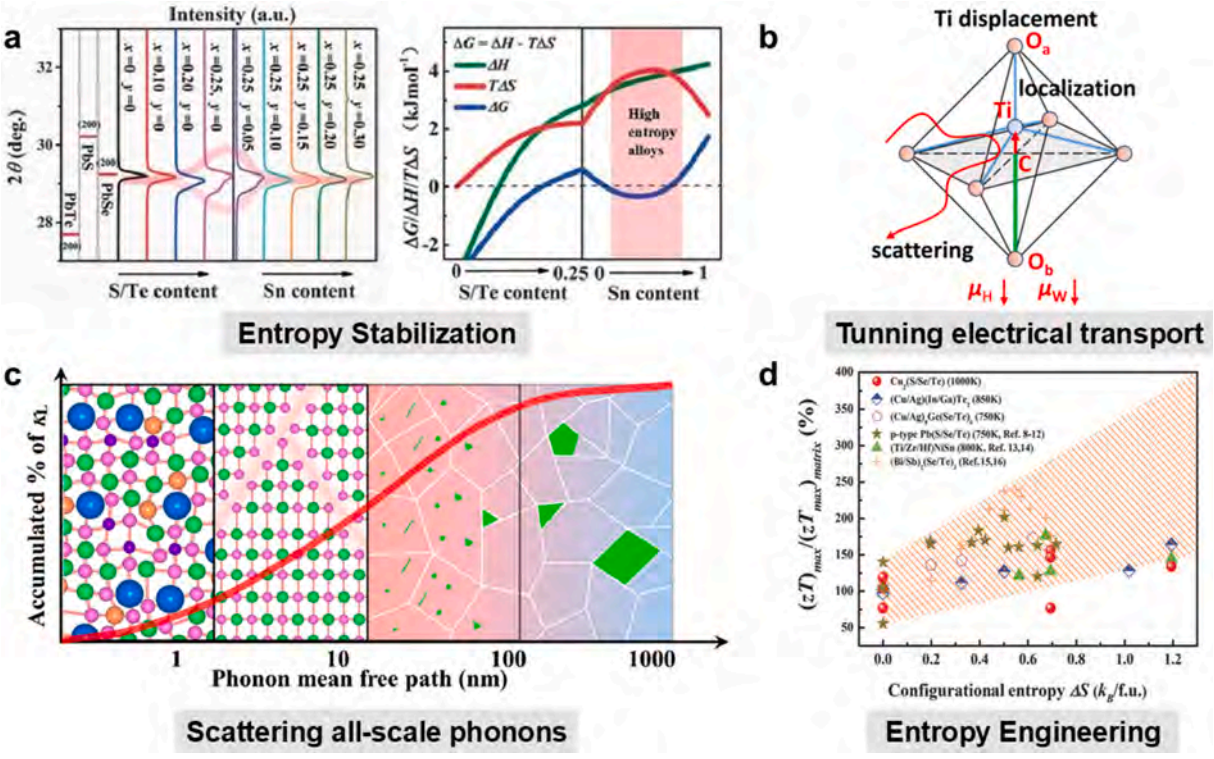

Fig. 16. (a) Entropy stabilization effect [217]. Copyright © 2021, The American Association for the Advancement of Science. (b) Tuning polyhedrons to enhance electrical properties. [238] Copyright © 2024, The Author(s). (c) Lattice distortion and defects in high entropy ceramics scattering all-scale phonons [228]. Copyright © 2021, The Author(s). (d) Entropy as a gene-like descriptor for thermoelectric properties [45]. Copyright © 2017 WILEY-VCH Verlag GmbH & Co. KGaA, Weinheim. (Reproduced).

precisely matches the needs of thermoelectrics, and entropy is considered as a gene-like indicator for promoting high zT thermoelectrics by some researchers [45].

The point-by-point explanations correlating four aspects with thermoelectric demand are as follows (Fig. 16).

(1) The entropy stabilization effect enables heavy doping and complex element substitution to form single-phase thermoelectric materials. This can introduce degenerate doping and phonon-scattering defects. Jiang et al. [217] fabricated single-phase high entropy $Pb_{0.89}Sb_{0.012}Sn_{0.1}Se_{0.5}Te_{0.25}S_{0.25}$ ceramics with a high content of doping elements, introducing defects and realizing zT value of 1.8 in n-type PbSe-based materials. In addition, high entropy ceramics can sustain high symmetry phases at relatively lower temperatures, optimizing the electrical transport properties [45]. For instance, Luo et al. combined $AgSbSe_2$-SnSe and $AgSbTe_2$-GeTe-MnTe to form new cubic phase solid solutions, and achieved a high zT value of over 1.0 [218,219].

(2) The lattice distortion effect in high entropy ceramics can strongly suppress the thermal conductivity due to phonon scattering by the distorted lattice [59,187]. The previously mentioned lattice size fluctuation (Eq. (26)), as part of the disorder scattering parameters Γ, could be a main factor in describing the extent of lattice distortion and disorder. The Debye-Callaway model describes the correlation between the lattice thermal conductivity and the disorder scattering parameter [220,221].

$$\kappa_L = \frac{k_B}{2\pi^2 v}\left(\frac{k_B}{h}\right)^3 T^3 \int_0^{\frac{\Theta_D}{T}} \frac{\tau x^4 e^x}{(e^x-1)^2} dx \tag{23}$$

$$\tau^{-1} = \tau_N^{-1} + \tau_U^{-1} + \tau_d^{-1} + \tau_b^{-1} + \cdots \tag{24}$$

$$\tau_d^{-1} = \frac{V}{4\pi v^3}\Gamma\omega^4 \tag{25}$$

$$\Gamma = \Gamma_{MF} + \Gamma_{SF} \tag{26}$$

where κ_L, k_B, v, ,h, T, Θ_D, τ, N, U, d, b, Γ, ω, Γ_{MF}, Γ_{SF} represent lattice thermal conductivity, Boltzmann constant, phonon velocity, Planck constant, temperature, Debye temperature, relaxation time, normal process, Umklapp process, defects, boundaries, disorder fluctuation parameter, phonon frequency, mass disorder fluctuation parameter, and strain disorder fluctuation parameter, respectively. Considering Eq. (25) given by Klemens [222,223], the Debye-Callaway model, and Mathiessen's Rule, the strain introduced by the high entropy design could be the main cause of phonon scattering. The phonon dispersion broadening, softening, and scattering [224,225] indicate the decrease of the relaxation time and the mean free path of phonons, contributing to the reduction of the lattice thermal conductivity. Firstly applied by thermal barrier coating ceramics [79,226,227], the lattice distortion effect of high entropy has been widely used in thermoelectrics [217,228]. In the work done by Jiang et al. in 2021, the nanostructure and the high entropy induced lattice distortion provided all-scale phonon scatters in p-type $Pb_{0.935}Na_{0.025}Cd_{0.04}Se_{0.5}S_{0.25}Te_{0.25}$ bulks, thus obtaining κ_L lower than 0.4 $W \bullet m^{-1} \bullet K^{-1}$ [228].

(3) The sluggish diffusion effect [75] in high entropy ceramics can be leveraged to slow down the movement of grain boundaries to get fine grains [229,230]. The large amount of grain boundaries in fine-grained ceramics could reduce the thermal conductivity [231–234]. Hu et al. [235] in 2018 desinged nanoprecipitates and fine grains in entropy-engineered SnTe-based ceramics, achieving a record low lattice thermal conductivity of 0.32 $W \bullet m^{-1} \bullet K^{-1}$, and demonstrating the applicability of sluggish diffusion effects in thermoelectrics. However, sluggish diffusion could prevent ceramics from densification during sintering and pose challenges to the samples that require annealing in the atmosphere. To overcome this, Zheng et al. [29] in 2021 used a 50 h sintering process for fabricating $(Ca_{0.2}Sr_{0.2}Ba_{0.2}Pb_{0.2}La_{0.2})TiO_3$ bulks, and a homemade apparatus to conduct an electrical current-assisted reducing process to anneal the samples. This approach achieved uniformly distributed high density oxygen vacancies in the samples. Nonetheless, the existence of the sluggish diffusion effect in high entropy ceramics is still questioned by some researchers [82], as ion mobility is high in these ceramics [236].

(4) The cocktail effect [237] in high entropy ceramics might give rise to new, comprehensive properties not found in any dopant independently [2,194]. While the effects of individual dopants are significant, the potential impacts of the cocktail effect should not be overlooked.

In thermoelectric oxides, high entropy strategies have played important roles. When designing high entropy thermoelectric oxides, oxides with multiple metal sites are preferred. The reasons are as follows. Metal ions participating in bonding with O provide orbitals for electrons and holes to transport in n-type and p-type thermoelectric oxides, dominating the electrical properties in thermoelectric oxides. In simple oxides with only one metal site [239], the disorder at the metal site by high entropy would strongly scatter the carriers, since carriers could transport through the only few channels provided by the only metal site. Oxides with multiple metal sites are more suitable in entropy engineering, since entropy design could be performed at sites not directly bonding to O, and providing undisturbed channels for carriers to transport. Perovskites as traditional thermoelectric oxides with A and B sites available to be tuned [55,240], are the main research focus in high entropy thermoelectric oxides, among which n-type $SrTiO_3$-based high entropy thermoelectric ceramics have received more attention [55].

For the *d* orbitals of the B-site transition metals dominating the carrier transport behaviors [241], the entropy engineering of the B-sites of perovskite oxides suppresses the lattice thermal conductivity at the expense of severely decreased electrical conductivity and mobility. Despite the 10 % La doping, the B-site disturbed $Sr_{0.9}La_{0.1}(Zr_{0.25}Sn_{0.25}Ti_{0.25}Hf_{0.25})O_3$ only displayed the electrical conductivity of 0.013 $S \bullet cm^{-1}$ [83]. The power factor (*PF*) of 67.9 $\mu W \bullet m^{-1} \bullet K^{-2}$ and zT of 0.1 were measured in $Sr(Ti_{0.2}Fe_{0.2}Mo_{0.2}Nb_{0.2}Cr_{0.2})O_3$ bulks, even though the lattice thermal conductivity was suppressed to 0.7 $W \bullet m^{-1} \bullet K^{-1}$ [131]. In comparison, the

entropy engineering at the A-sites of $SrTiO_3$ seems more promising. The high entropy $(Ca_{0.2}Sr_{0.2}Ba_{0.2}Pb_{0.2}La_{0.2})TiO_3$ bulks achieved *PF* of 295 $\mu W \bullet m^{-1} \bullet K^{-2}$ and the thermal conductivity of ~ 1.2 $W \bullet m^{-1} \bullet K^{-1}$, attributed to the uniformly distributed high density of oxygen vacancies formed during the annealing process in 5 % H_2/95 % Ar with the assistant of electrical current [29]. Annealed under an Ar/graphite atmosphere, the $(Ca_{0.2}Sr_{0.2}Ba_{0.2}Pb_{0.2}La_{0.2})TiO_3$ bulks exhibited a *PF* of 249 $\mu W \bullet m^{-1} \bullet K^{-2}$ and thermal conductivity of ~ 2.0 $W \bullet m^{-1} \bullet K^{-1}$ [242].

To avoid the deterioration of electrical mobility caused by the severe lattice distortion of high entropy, the middle entropy $(Ca_{0.25}Sr_{0.25}Ba_{0.25}Re_{0.25})TiO_3$ (Re representing the rare metals) bulks were intensively studied. The entropy-induced glass-like thermal conductivity is still maintained in middle entropy $(Ca_{0.25}Sr_{0.25}Ba_{0.25}Nd_{0.25})TiO_3$ [243]. The electrical conductivity and the *PF* value at 1073 K were restored to 105 $S \bullet cm^{-1}$ and 420 $\mu W \bullet m^{-1} \bullet K^{-2}$ in $(Ca_{0.25}Sr_{0.25}Ba_{0.25}La_{0.25})TiO_3$ bulks, but the expense was that the minimum thermal conductivity was also higher back to 2.5 $W \bullet m^{-1} \bullet K^{-1}$ at high temperature [244]. Further reducing the entropy in the middle entropy range, the high room temperature electrical mobility of 3.04 $cm^2 \bullet V^{-1} \bullet s^{-1}$, PF_{max} of 553 $\mu W \bullet m^{-1} \bullet K^{-2}$ at 973 K were realized in $Sr_{0.6}Ba_{0.3}La_{0.1}Ti_{0.9}Nb_{0.1}O_{3-\delta}$, and the minimum thermal conductivity of 3.86 $W \bullet m^{-1} \bullet K^{-1}$ was far from satisfaction [245].

Other entropy designed thermoelectric oxides also suffered from carrier-phonon coupling. For example, n-type A-site high entropy $CaMnO_3$-based $La_{0.2}Ca_{0.2}Sr_{0.2}Ba_{0.2}Y_{0.2}MnO_3$ ceramics were synthesized and suffered from the low PF_{max} of 26.6 $\mu W \bullet m^{-1} \bullet K^{-2}$ at 873 K [246]. In p-type thermoelectric oxides, the A-site high entropy $LaCoO_3$- and $Ca_3Co_4O_9$-based cobaltates were fabricated. The high *PF* of 499 $\mu W \bullet m^{-1} \bullet K^{-2}$ and low lattice thermal conductivity of 0.72 $W \bullet m^{-1} \bullet K^{-1}$ at 350 *K* in $(LaNdPrSmEu)_{0.95}Sr_{0.05}CoO_3$ was achieved, but the PF of 499 $\mu W \bullet m^{-1} \bullet K^{-2}$ was lower than the pristine $La_{0.95}Sr_{0.05}CoO_3$ [247]. The highest zT among high entropy thermoelectric oxide bulks to date was 0.3 in textured $(Ca_{0.35}Sr_{0.2}Ba_{0.15}Na_{0.2}Bi_{0.1})_3Co_4O_9$, benefited from the lattice distortion and layered structure induced low lattice thermal conductivity of 0.66 $W \bullet m^{-1} \bullet K^{-1}$ [248], but the zT was still less competitive than the pristine $Ca_3Co_4O_9$ due to the electrical performance deterioration [249].

The current studies on high or middle entropy thermoelectric oxides are listed in Table. 2. In general, the lattice thermal conductivity reduction from the high entropy lattice distortion effect is common in literature, and the mediocre *PF* of ~ 250 to 500 $\mu W \bullet m^{-1} \bullet K^{-2}$ limited the zT to the range of 0.1 to 0.3. The electrical mobility deteriorates in high entropy oxides when reducing the phonon mean free path (MFP). How to decouple the electrical-thermal transport remains a problem in entropy engineering.

To decouple the carrier-phonon transport and further enhance the properties of thermoelectric oxides via the high entropy strategy, a deep understanding of high entropy mechanisms and the development of new thermoelectric oxides are needed [250]. Several key aspects should be emphasized when designing the experiments (Fig. 17).

(1) Elements still matter in deciding the properties. The 4f orbitals of Pr/Tb dopants in high entropy $(Zr_{0.2}La_{0.2}Tb_{0.2}Sm_{0.2}Y_{0.2})O_{2-\delta}$ lay in the middle of the band gap, reducing the band gap to 2 *eV* [115]. The Cd-doping converges the light and heavy band of

Table 2
Comparison of thermoelectric properties for the high entropy oxide ceramics.

Composition	T [*K*]	zT_{max}	PF_{max} [$\mu W \bullet m^{-1} \bullet K^{-2}$]	S [$\mu V \bullet K^{-1}$]	σ [$S \bullet cm^{-1}$]	n (RT) [10^{19} cm^{-3}]	μ (RT) [$cm^2 \bullet V^{-1} \bullet s^{-2}$]	κ [$W \bullet m^{-1} \bullet K^{-1}$]	κ_L [$W \bullet m^{-1} \bullet K^{-1}$]	References
B-site high entropy n-type $SrTiO_3$-based ceramics										
$Sr(Ti_{0.2}Fe_{0.2}Mo_{0.2}Nb_{0.2}Cr_{0.2})O_3$	1073	0.10	68	−94	77	/	/	0.71	0.70	[131]
$Sr_{0.9}La_{0.1}(Zr_{0.25}Sn_{0.25}Ti_{0.25}Hf_{0.25})O_3$	873	0.000092	0.20	−393	0.013	/	/	1.89	1.89	[83]
A-site high entropy n-type $SrTiO_3$-based ceramics										
$(Ca_{0.2}Sr_{0.2}Ba_{0.2}Pb_{0.2}La_{0.2})TiO_3$	873	0.20	295	−255	45	/	/	1.20	1.15	[29]
$(Ca_{0.2}Sr_{0.2}Ba_{0.2}La_{0.2}Pb_{0.2})TiO_3$	1073	0.12	249	−200	62	5.74	/	2.20	2.04	[242]
$(Sr_{0.25}Ca_{0.25}Ba_{0.25}Nd_{0.25})TiO_3$	1073	0.13	313	−200	78	5.68	0.44	2.61	2.60	[243]
$(Ca_{0.25}Sr_{0.25}Ba_{0.25}La_{0.25})TiO_3$	1073	0.18	420	−200	105	7.98	0.18	2.50	2.26	[244]
$Sr_{0.6}Ba_{0.3}La_{0.1}Ti_{0.9}Nb_{0.1}O_{3-\delta}$	973	0.14	553	−160	216	8.89	3.04	3.86	3.36	[245]
$(Sr_{0.25}Ca_{0.25}Ba_{0.25}La_{0.25})TiO_3$/Pb@Bi	1073	0.18	330	−170	112	7.27	2.34	1.90	1.70	[15]
A-site high entropy n-type $CaMnO_3$-based ceramics										
$La_{0.2}Ca_{0.2}Sr_{0.2}Ba_{0.2}Y_{0.2}MnO_3$	873	0.017	27	−40	171	/	/	1.35	1.31	[246]
A-site high entropy p-type $LaCoO_3$-based ceramics										
$(LaNdPrSmEu)_{0.95}Sr_{0.05}CoO_3$	350	0.23	499	271	68	/	/	0.75	0.72	[247]
A-site high entropy p-type $Ca_3Co_4O_9$-based layered ceramics										
$(Ca_{0.35}Sr_{0.2}Ba_{0.15}Na_{0.2}Bi_{0.1})_3Co_4O_9$	973	0.30	270	174	89	0.0114	531	0.87	0.66	[248]

Note: The temperature point corresponding to parameters of zT_{max}, PF_{max}, S, σ, κ_L and κ is consistent with the temperature of zT_{max} value. RT (room temperature).

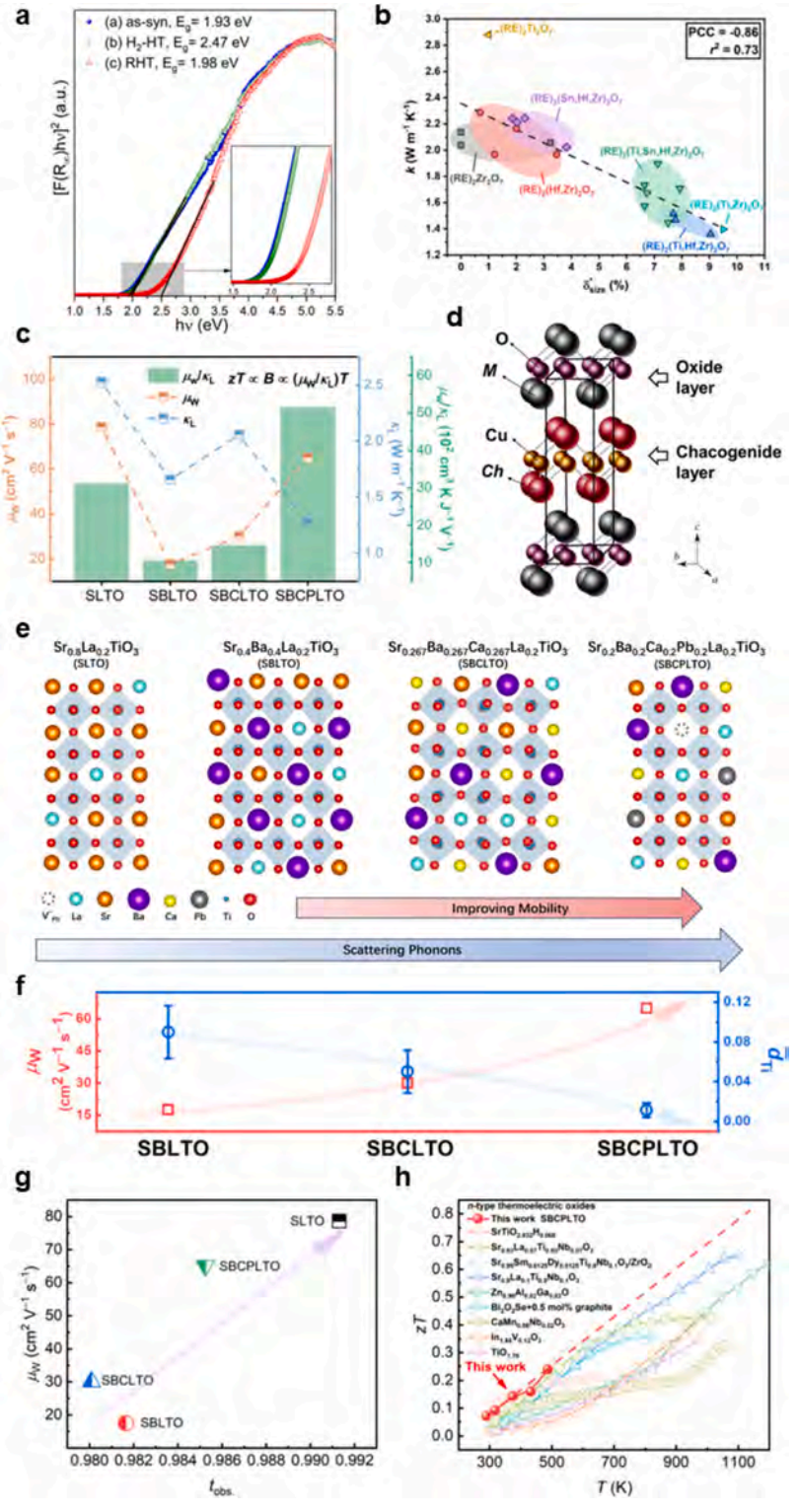

(caption on next page)

Fig. 17. Examples of key aspects for enhancement of thermoelectric properties via high entropy strategy. (a) Reversible band tuning based on certain compositions, which is validated by the Tauc plot obtained from the UV–Vis spectra of $(Ce_{0.2}La_{0.2}Pr_{0.2}Sm_{0.2}Y_{0.2})O_{2-\delta}$ powder [115]. Copyright © 2020, The Author(s). (b) Correlation of thermal conductivity with size disorder parameter of all 22 single-phase pyrochlores, indicating the nonmonotonic variation between thermal conductivity and entropy [52]. Copyright © 2020 Acta Materialia. (c) The work on the decoupling of carrier-phonon transport showing correlation between entropy and transport parameters to reveal the point that the entropy is not necessarily monotonically correlated to physical variants [238]. Copyright © 2024, The Author(s). (d) The crystal structure of MCuChO (M: Bi, lanthanide ions; Ch: chalcogen ions) [201]. Copyright © 2022 Elsevier. (e) The schematic of the strategy to decouple carrier-phonon transport via entropy engineering. (f) The enhanced weighted mobility μ_W due to the Ti displacement decrease. (g) The correlation between the tolerance factor $t_{obs.}$ and μ_W to show the effect from tuning element average radius. (h) The improved zT via entropy engineering [238]. Copyright © 2024, The Author (s). (Reproduced).

entropy-engineered PbSe-based ceramics, enhancing the Seebeck coefficient(Fig. 17 (**a**)) [228]. The introduction of individual elements in high entropy materials functions similarly in low entropy materials in many cases. The selection of elements is vital when increasing the entropy. And as aforementioned, like the selection of crystal sites to be substituted in high entropy perovskites, the right choice of the crystal site to be entropy-engineered is important, because certain phonon and electron branches in energy dispersion dominate the thermal and electrical transport, and the specific crystal sites mainly affect these certain branches [251–253].

(2) Not all properties monotonically change with increasing entropy. Taking lattice thermal conductivity for instance, the lattice distortion could minimize the thermal diffusivity and the phonon MFP [52,225], but the extent of lattice distortion is not always positively correlated with entropy [142,254]. As shown in Fig. 17 (**b**), the size disorder factor, as an indirect indicator of the high entropy effect, does not fit well in a linear relationship with thermal conductivity [52,254]. And when light elements are doped, the thermal capacity increases, according to the Dulong-Petit rule [255,256], opposite from the commonly accepted negative-correlated thermal conductivity-entropy trends (Fig. 17**(c)** [238]. Furthermore, the phonon group velocity could increase [257–259] or decrease [260] when multiple elements are introduced, decided by the strength of bonds formed, not the entropy. According to the equation, $\kappa_L = \frac{1}{3}Cvl$, where κ_L, C, v and l, represent lattice thermal conductivity, thermal capacity, phonon group velocity, and phonon MFP. The lattice thermal conductivity does not necessarily decrease with increasing entropy.

(3) New strategies to decouple thermal and electrical transport are needed. Zhang et al. [15] used the *in situ* precipitated Pb@Bi alloys to form conductive pathways and hierarchical structure in middle entropy $(Sr_{0.25}Ca_{0.25}Ba_{0.25}La_{0.25})TiO_3$, providing an effective strategy in entropy engineering of thermoelectric oxides from the aspect of extrinsic compositing [261]. In another way, the entropy engineering could help tune the crystal symmetry and ion displacement, which has been applied in dielectric capacitors [167,262]. Tuning the distortion of metal-oxide polyhedrons and the displacement of ions could also contribute to the electrical transport. Zheng et al. recently reported that the TiO_6 octahedron distortion and Ti displacement could be tailored by engineering entropy at A sites of $SrTiO_3$-based thermoelectric perovskite oxides. With lattice thermal conductivity approaching amorphous limit, by tuning the A-site average radius through element selection, the tolerance factor of the perovskite could approach 1 to suppress the Ti displacement, hence minimizing the carrier localization and scattering to enhance the mobility and decouple carrier-phonon transport via entropy engineering(Fig. 16 (**b**) and Fig. 17 (**c, e-h**)) [238]. Rational entropy engineering could be a new strategy to decouple carrier-phonon transport from the intrinsic aspect. Other strategies, like Mott-Ioffe-Regel law [233,263], might also function, for the carrier MFP approaches atomic distance in high entropy oxides.

(4) New types of oxides are demanded for high entropy thermoelectrics. For instance, layered oxides like BiCuSeO consisting of conductive and blocking layers (Fig. 17 (**d**)) [201], and oxides with high carrier mobility and low lattice thermal conductivity should be considered. Besides ceramics, there is a vast research space in single crystals and thin films. Suitable calculation methods might also push this field far forwards. In conclusion, entropy engineering is promising in optimizing the thermoelectric properties of oxides, yet more work needs to be done.

4.2. Thermal resistive property for thermal barrier coating

Thermal barrier coatings (TBCs) are extensively applied on the metallic surfaces of hot-end components in aircraft engines and industrial gas turbines to improve high-temperature endurance during long-term operation, thus extending service lifetime and improving energy conversion efficiency [264,265,17]. Ideal TBCs should possess low thermal conductivity, a well-matched thermal expansion coefficient (TEC) with the metallic substrates, and excellent thermal stability [266–268]. To date, yttrium-stabilized zirconia (YSZ) is the most widely used TBC ceramics, due to its robust mechanical properties and good thermophysical properties. However, long-term use of YSZ above 1473 K is not suitable as it undergoes an abrupt volume change due to the multiple-phase transition at high temperatures [269–273].

To address this issue, new types of TBCs with higher temperature phase stability are desirable. Over the past decades, pyrochlore-type or fluorite-type $A_2B_2O_7$ compounds (where A represents trivalent metal elements, usually rare earth elements, and B represents tetravalent metal elements, usually Zr, Hf, Ce, and Sn) have been proposed as promising TBCs candidates due to their excellent sintering resistance and phase stability. Nevertheless, their relatively high thermal conductivity and low TEC need to be optimized for further practical application [269–275].

Due to the high entropy effect, HEOs offer a promising option for advanced TBCs with superior phase stability, unique thermo-

physical behaviors, and excellent mechanical performance. Braun et al. [187] studied single-crystal rocksalt HEOs including $(Mg_{0.2}Ni_{0.2}Cu_{0.2}Co_{0.2}Zn_{0.2})O$ and the former composition plus an additional cation (Sc, Sb, Sn, Cr and Ge) and demonstrated that local ionic charge disorder could effectively reduce thermal conductivity without compromising mechanical stiffness. A correlation between mechanical behaviors and thermal performance via the ratio of Young's modulus E and thermal conductivity k is established since a reduction in thermal conductivity usually results in a compromise on the stiffness of a crystal (quantitatively described by Young's modulus). A decrease in the elastic modulus indicates a reduction in the phonon group velocity and energies, leading to suppressed thermal conductivity. Thus the parameter $E/k \propto 1/C_v\tau$, where C_v and τ represent the heat capacity at constant volume and phonon lifetime, respectively. According to this parameter, HEOs appear to realize unique combinations of simultaneously high elastic modulus and low thermal conductivity (Fig.18).

Recently, entropy engineering has emerged as an effective strategy widely adopted in TBCs materials, particularly $A_2B_2O_7$-type ceramics [277]. The overall performance of high-entropy TBCs can be influenced by four aspects of high entropy, as mentioned in section 2.3. For instance, the thermal conductivity could be significantly decreased by the lattice distortion effect due to the strong phonon scatterings. The cocktail effects enable the introduction of more elements for composition design, thus making the performance more controllable [267,270]. The recent advances in high entropy $A_2B_2O_7$-type TBCs can be categorized into A-site and B-site high entropy TBCs. The associated properties are summarized in Table. 3.

(a) A-site high entropy TBCs

Benefiting from entropy engineering, the highly sintering resistance, excellent thermal stability, low thermal conductivity, and large TEC could be simultaneously realized. Zhang et al. successfully prepared high-entropy pyrochlore-type structures based on rare-earth (RE) zirconates by conventional solid-state reaction method and reached low thermal conductivity below 1 $W \bullet m^{-1} \bullet K^{-1}$ in the temperature range of 573–1473 K [269]. In addition, the mechanical properties could also be modified. A high hardness of 15.88 GPa and Young's modulus of 295.5 GPa were achieved in high-entropy titanate pyrochlore ceramics. Combined with the low thermal conductivity of 0.947 $W \bullet m^{-1} \bullet K^{-1}$, an exquisite balance between stiffness and insulation outperformed the current reported works [272]. Furthermore, by studying the hot corrosion behavior of high entropy $(La_{0.2}Nd_{0.2}Sm_{0.2}Eu_{0.2}Gd_{0.2})_2Ce_2O_7$, it is found that the sluggish diffusion effect greatly inhibited nucleation of corrosion products and resulted in a reduction in corrosion depth, demonstrating improved corrosion resistance [278].

(b) B-site high entropy TBCs

To expand the composition design for $A_2B_2O_7$-type TBCs, it is very important to synthesize B-site doped high entropy ceramics. Wang et al designed high-entropy $La_2B_2O_7$ (B = Zn, Mg/Ni, Ce/Zr/Hf/Sn/Ti, W, Mo), with non-equivalent principal elements. It was found that $La_2(ZnMgZrWMo)_2O_7$ not only possessed high TEC ($13.9 \times 10^{-6}\ K^{-1}$) and low thermal conductivity ($0.8\ W \bullet m^{-1} \bullet K^{-1}$) but also exhibited good calcium-magnesium-aluminosilicate (CMAS) resistance [279]. Xu et al. [280] also proved that the incorporation of heterovalent cations at B-sites in high-entropy $A_2B_2O_7$ ceramics is an effective strategy to reduce the thermal conductivity without compromising the decrease of oxygen vacancy. To predict reduced thermal conductivity, Luo et al proposed that a modified size disorder parameter could be a useful index for designing thermally insulative compositionally complex ceramics.

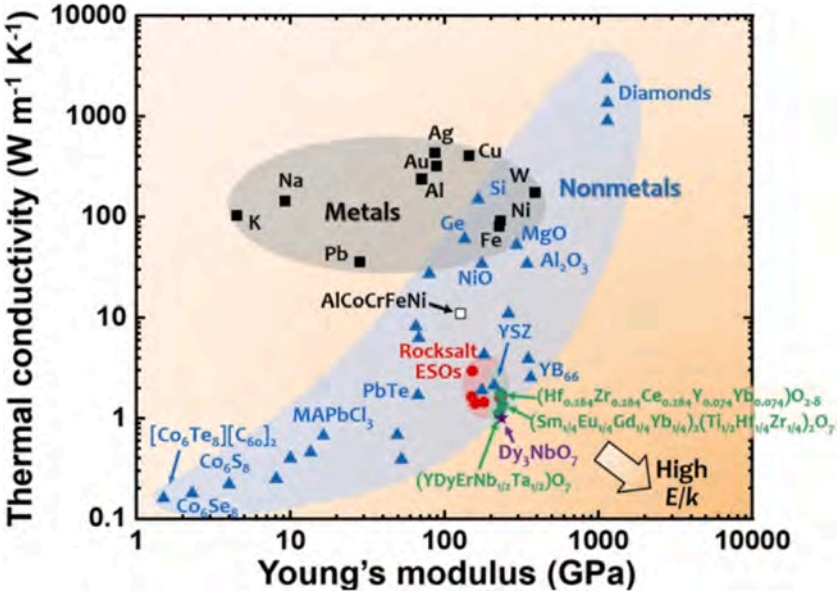

Fig. 18. Thermal conductivity (k) versus Young's modulus (E) in a double logarithmical plot to feature several HEOs with high E/k ratio [276]. Copyright © 2020, Springer Nature

Table 3
Summary of high entropy $A_2B_2O_7$-type thermal barrier coatings.

Material	Classification	Thermal conductivity, κ ($W \bullet m^{-1} \bullet K^{-1}$)	Thermal expansion coefficient, TEC ($10^{-6}\ K^{-1}$)	References
$(La_{0.2}Nd_{0.2}Y_{0.2}Eu_{0.2}Gd_{0.2})_2Zr_2O_7$	A-site	1.0 @1773 K	/	[269]
$(Sm_{0.2}Eu_{0.2}Tb_{0.2}Dy_{0.2}Lu_{0.2})_2Zr_2O_7$	A-site	0.9 @1273 K	11.0 @1273 K	[273]
$(La_{0.2}Nd_{0.2}Yb_{0.2}Y_{0.2}Lu_{0.2})_2Ce_2O_7$	A-site	1.1 @1273 K	12.6 @1485 K	[281]
$(La_{0.25}Dy_{0.25}Yb_{0.25}Y_{0.25})_2Ce_2O_7$	A-site	1.0 @1273 K	12.6 @1473 K	[282]
$(La_{0.2}Nd_{0.2}Sm_{0.2}Eu_{0.2}Gd_{0.2})_2Ce_2O_7$	A-site	0.9 @1673 K	12.0 @1673 K	[274]
$(La_{0.2}Nd_{0.2}Sm_{0.2}Gd_{0.2}Yb_{0.2})_2Zr_2O_7$	A-site	0.9 @1273 K	10.9 @1273 K	[270]
$Dy_2(Ti_{0.2}Zr_{0.2}Hf_{0.2}Ge_{0.2}Sn_{0.2})_2O_7$	B-site	1.4 @1173 K	/	[107]
$Y_2(Ce_{0.2}Zr_{0.2}Hf_{0.2}Sn_{0.2}Ti_{0.2})_2O_7$	B-site	1.3 @300 K	11.7 @1473 K	[283]
$La_2(Zr_{0.2}Ce_{0.2}Hf_{0.2}Sn_{0.2}Ti_{0.2})_2O_7$	B-site	1.1 @1073 K	9.7 @1273 K	[282]
$La_2(ZnMgZrWMo)_2O_7$	B-site	0.8 @873 K	13.9 @1473 K	[279]
$Y_2(Ti_{0.2}Zr_{0.2}Hf_{0.2}Nb_{0.2}Ta_{0.2})_2O_7$	B-site	1.9 @1673 K	/	[284]
$Dy_2(Y_{0.2}Yb_{0.2}Nb_{0.2}Ta_{0.2}Ce_{0.2})_2O_7$	B-site	0.9 @300 K	10.4 @1073 K	[280]

4.3. Dielectric and energy storage property

Dielectrics help hold charges as capacitors. Capacitors are fundamental energy storage components and electrostatic capacitors based on dielectric materials and have become crucial components in fields of electronics energy storage, power systems, and the automotive industry. Among other energy storage forms, capacitors are competitive in their ultrahigh power densities, high voltage endurance, and good reliability as the only type of all-solid device capable of releasing a large amount of electrical energy in a very short time. Nevertheless, capacitors suffer from low energy storage density in practical usage. Future trends in capacitor-based energy storage development of capacitors include miniaturization, high energy storage density, high voltage, and high stability. [285–287].

When exposed to an electric field, dielectric materials exhibit polarization, where positive and negative charges within the material are displaced in opposite directions. Polarization is the function of permittivity ε and electric field strength E. Response of polarization to an electric field depends on materials with several mechanisms and thus dielectric materials can be classified into five types through their polarization–electric field loop (P-E loop): linear, paraelectric, ferroelectric, relaxor ferroelectric, and antiferroelectric dielectrics [288]. When subjected to a varying electric field, the energy dissipation manifests as heat and is referred as dielectric loss tanδ, which is the tangent of the loss angle between the vectors of the complex permittivity and the imaginary part of the permittivity. Therefore, for different aspects of capacitor applications, other evaluation parameters are present, such as the quality factor Q f, mostly considered in microwave field, where Q is 1/tanδ and f is the resonant frequency. When the voltage reaches to a critical value, a proportion of the dielectric material experiences electrical breakdown and turns into a conductor and this minimum voltage to become electrically conductive is named as breakdown voltage E_b. Basically, the key parameter for final performance and practicality is the energy storage efficiency $\eta = \frac{U_e}{U_e+U_{loss}}$. $U_e = \int_{P_r}^{P_m} EdP$, denotes energy density, where remanent polarization P_r refers to the polarization that remains in the material after the external electric field is removed and P_m refers to maximum spontaneous polarization. U_{loss} is energy loss due to dielectric loss, hysteresis, etc.

Based on these parameters describing dielectric and energy storage behaviors, the target of performance enhancement can be summarized as three parts: increase maximum polarization, reduce remnant polarization, and enhance breakdown field strength. However, an inverse coupling relation occurs between breakdown voltage E_b and permittivity ε, as well as between U_e and η [289].

According to application scenarios, there are various inorganic material systems that have been fully verified in scientific research and industrial practice, such as $BaTiO_3$, $BiFeO_3$, and $(Bi_{0.5}Na_{0.5})TiO_3$ for multi-layer ceramic capacitors (MLCCs) [288,290,291]. HEOs, due to their high stability, tailored performance, mechanical robustness and other unique characteristics in dielectrics, are receiving increasingly intensified research attention.

HEOs have demonstrated their colossal permittivity. Bérardan et al. first reported a rock-salt structured HEO with Li^+ doping. The permittivity of $(Mg, Co, Ni, Cu, Zn)_{0.95}Li_{0.05}O$ exhibit up to 2×10^5 measured at 440 K and 20 Hz. In addition, the author found that the (MgCoNiCuZn)O-based family with high-entropy phase all possessed large values of relative permittivity regardless of substitutions. In other words, a colossal dielectric constant appears to be an intrinsic characteristic in this system, provided that the material maintains a high-entropy structure. A similar performance was found by Zhang et al. [292] in high-entropy $(La_{0.2}Li_{0.2}Ba_{0.2}Sr_{0.2}Ca_{0.2})Nb_2O_{6-\delta}$ tungsten bronze ceramics. The bulk features giant dielectric properties of dielectric constant orders of magnitude in $10^5 \sim 10^6$ when measured at 100 Hz and 625 °C, which is 1000 times that of traditional $Sr_{0.55}Ba_{0.45}Nb_2O_6$ ceramic at the same frequency. Compared to $(Ba_{1/3}Sr_{1/3}Ca_{1/3})Nb_2O_6$ ceramic, the enhanced dielectric constant and temperature stability of dielectric constant of $(La_{0.2}Li_{0.2}Ba_{0.2}Sr_{0.2}Ca_{0.2})Nb_2O_{6-\delta}$ can be contributed to the phase structure with severe lattice distortion and the presence of oxygen vacancy introduced by high-entropy design. Likewise, Xie et al. [293] investigated the effect of high entropy design on the dielectric properties in defective fluorite structure $A_2B_2O_7$. The $(La_{0.2}Pr_{0.2}Nd_{0.2}Sm_{0.2}Eu_{0.2})_2Ce_2O_7$ ceramic samples display large dielectric properties (the order of dielectric constant is 10^5-10^6) under the condition of high temperature and low frequency conditions (about 320,000 at 642°C, 100 Hz) and relatively low leakage current density between 10^{-7} and $10^{-6}\ A \bullet cm^{-2}$. However, the underlying mechanism of this large permittivity remains elusive, and although some studies have offered detailed explanations for various microstructures-dielectricity relations within identically formulated systems, further study is needed [294].

Relaxor ferroelectric behavior was observed by Yan et al. [295] in $(Ca_{0.5}Sr_{0.5}Ba_{0.5}Pb_{0.5})Nb_2O_7$ (CSBPN) perovskite layered

structure ceramics. The CSBPN bulk showed single-phase orthorhombic structure with Cmcm space group and relaxor behavior characterized by broad and frequency-dependent permittivity maxima, nanosized polar regions and slim P-E hysteresis loops. The current peak near zero electric field indicated the presence of an ergodic relaxor behavior until 100 °C, while linear-like dielectric behavior was observed above 100 °C, as evidenced by nearly rectangular I-E hysteresis and linear P-E loops. Moreover, The permittivity of high-entropy CSBPN ceramics measured at low frequency and room temperature is 130, which is nearly three times larger than that of conventional perovskite layered structure ceramics including $Sr_2Nb_2O_7$ ($\varepsilon_r = 42$) and $Ca_2Nb_2O_7$ ($\varepsilon_r = 38$). The significant increase of permittivity and unusual relaxor behavior in CSBPN ceramic can be attributed to the effect of polar nanoregions (PNRs) and local random fields induced by elemental disorder. Synthesized single-crystal $Ba(Ti_{0.2}Sn_{0.2}Zr_{0.2}Hf_{0.2}Nb_{0.2})O_3$ films by Sharma et al. [296] reveal multiple phase transitions, a high Curie temperature of 570 K, and the relaxor ferroelectric nature.

In addition to colossal permittivity, the disordered distribution of various cations may lead to improved Q_f value, thus making high entropy design a potiential strategy in developing advanced microwave ceramics with high performance. Chen et al. [297] developed a high-entropy $(Hf_{0.25}Zr_{0.25}Sn_{0.25}Ti_{0.25})O_2$ ceramic with remarkable microwave dielectric characteristics of $\varepsilon_r = 25.6$, $Q_f = 74600$ GHz at 6.5 GHz and τ_f = -47 ppm $\bullet^{\circ}C^{-1}$. The typical phase transition in $ZrTiO_4$ ceramics at a temperature below 1200 °C is confirmed to be an ordered-disordered transition, which is characterized by a transition from the high-temperature phase with a random distribution of cations to an ordered low-temperature phase, with the disordered phase has a better Q_f value in these microwave dielectric ceramics. Therefore, the introduction of Hf and Sn elements and the high entropy design contribute to the microstructure homogeneity caused by the disordered state and eventually lead to the optimized Q_f value. Similarly, a high-entropy oxide $Li(Gd_{0.2}Ho_{0.2}Er_{0.2}Yb_{0.2}Lu_{0.2})GeO_4$ was reported by Fang et al. [298] with outstanding microwave dielectric properties and stable τ_f of $-2.9\ ppm \bullet^{\circ}C^{-1}$. The weak $[RO_6]$ distortion caused by the joint occupation of five different cations corresponded to the more stable temperature coefficient of the resonant frequency.

In terms of developing high performance MLCCs, which require low loss (tanδ), excellent temperature stability and high dielectric constant (ε_r), high entropy design pivots a novel path of realization. Qi et. al. [299] reported a configuration entropy designed multielement $BaTiO_3$-$BiFeO_3$-$CaTiO_3$ (BTO-BFO-CTO) ternary system (Fig. 19**(a)** and **(b)**), combining the high intrinsic dielectric E_b of CTO, and large P_s of BTO-BFO. By delicately controlling the composition and sintering condition, the nanoisland-like segregations were precipitated around the main grains, scattering electron carriers and impeding the electrical breakdown pathway under a highly applied electric field (Fig. 19**(c)**). As a result, synergistic optimization of polarization and breakdown strength was achieved in the BTO-BFO-CTO system, leading to an ultrahigh W_{rec} of $\sim 7.2\ J \bullet cm^{-3}$ in bulks at an enhanced E_b of $39\ kV \bullet mm^{-1}$ (Fig. 19**(d)**). The corresponding multilayer ceramic capacitors showed an improved W_{rec} of $16.6\ J \bullet cm^{-3}$ and a high η of 83 %, demonstrating that this system is a promising candidate for energy storage application under specific conditions (Fig. 19**(e)**).

Dielectric-based energy storage capacitors, which store and release electric energy at an ultrahigh speed in response of dipoles to an external electric field, are widely investigated for advanced electronic and electrical power systems. Recently, benefiting from the high entropy effects, the dielectric energy storage performance has been substantially improved using high-entropy dielectrics. For instance, Yang et al. [229] reported a high-entropy stabilized pyrochlore $Bi_2Ti_2O_7$-based films by introducing multiple La, Zr, Hf and

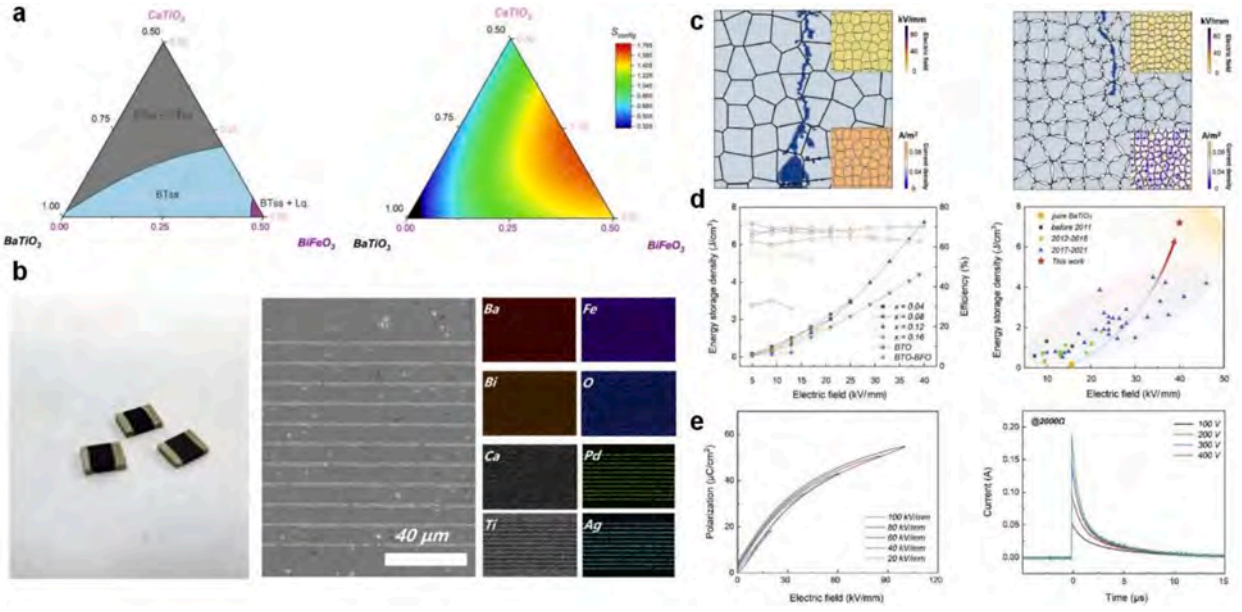

Fig. 19. (a) Phase diagram and configuration entropy of the $BaTiO_3$-$BiFeO_3$-$CaTiO_3$ ternary compositions. (b) The digital image and the cross-sectional SEM micrographs of the MLCC. (c) The nanoisland-like segregations modeling and (d) the energy storage performance of the bulk ceramic samples (e) High energy storage performance of the corresponding multilayer ceramic capacitors. [299] (Reproduced). Copyright © 2022, The Author(s).

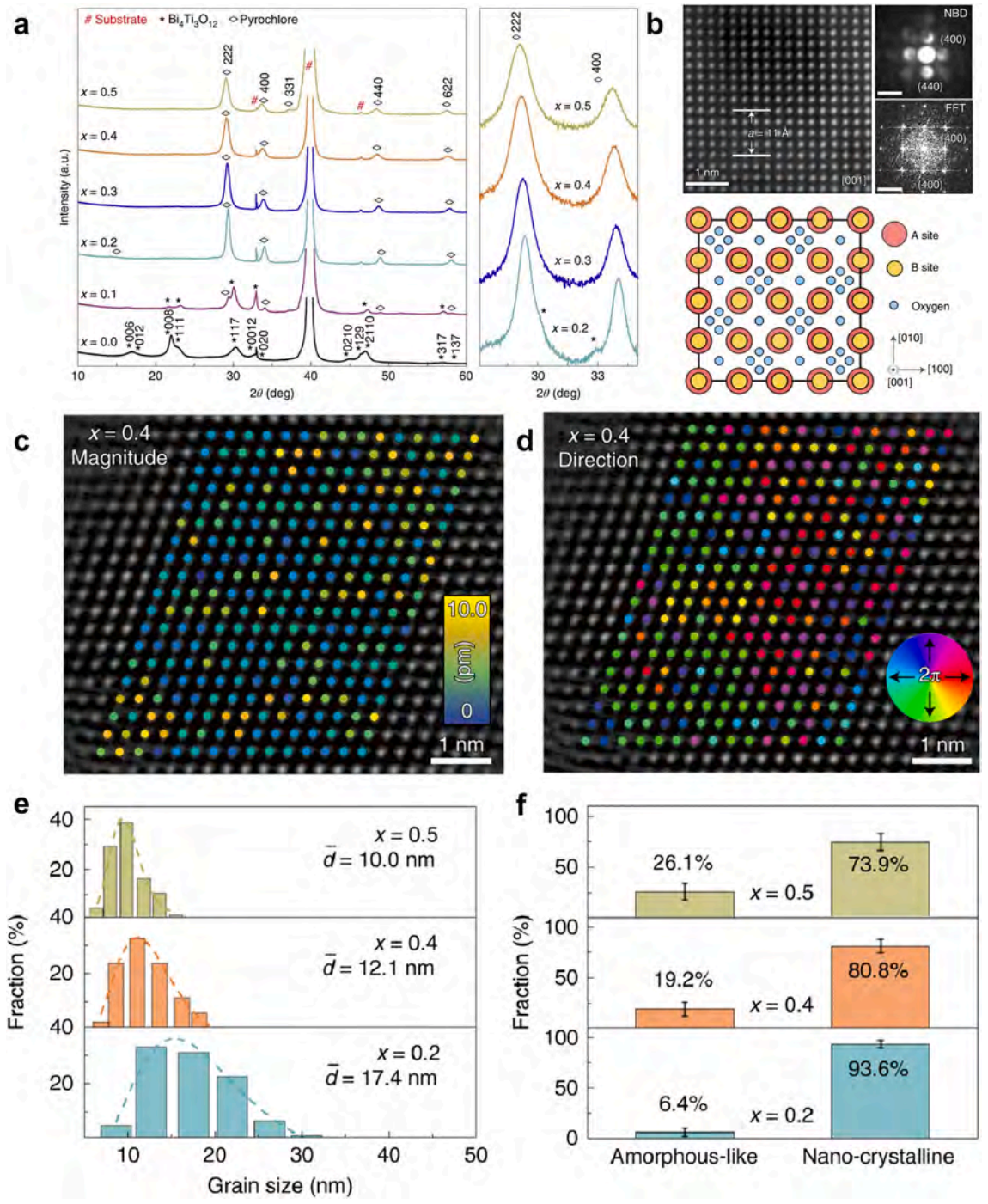

Fig. 20. (a) X-ray diffraction patterns of pyrochlore $Bi_2Ti_2O_7$-based films with increasing x. (b) HAADF, nano beam diffraction (NBD) and Fast Fourier transform (FFT) images acquired along the [001] zone axis of the high-entropy film with x = 0.4. (c) and (d), Lattice distortion illustrated by the mappings of magnitude (c) and direction (d) of cation displacements in the high-entropy film of x = 0.4. (e) and (f), Statistical grain size distributions (e) and fractions of the crystalline and amorphous-like phases (f) with the increase of entropy. (g-j) Energy storage performance of high entropy pyrochlore thin film, including (g) energy density and efficiency as functions of electric field up to E_b, (h) comparison of the energy density and efficiency with other dielectrics, (i) charging-discharging reliability and (j) temperature dependence of the energy storage properties of the films at an electric field of 2.5 MV/cm, respectively. [229] (Reproduced). Copyright © 2022 Springer Nature.

Sn elements into $Bi_4Ti_3O_2$ films. The results reveal that the increasing configuration entropy can reduce the system Gibbs free energy ΔG (ΔG = ΔH – TΔS), and thus stabilize the thermally unstable $Bi_2Ti_2O_7$ pyrochlore phase (Fig. 20**(a)** and **(b)**). These materials act as linear-like dielectrics with ultralow loss tangent and medium permittivity, contributing to high energy storage performances.

With the consideration of the different mass, size and electronegativity of introduced multiple atoms, the high-entropy composition of x = 0.4 showed large lattice distortion as confirmed by the STEM with HAADF imaging (Fig. 20 (**c**) and (**d**)). Such a scenario brings to high-entropy sluggish diffusion effects. Based on the STEM techniques, it was proved the grain size decreases and the amorphous phase increased with the increasing entropy as shown in Fig. 20 (**e**) and (**f**). Eventually, the high-entropy stabilized linear-like pyrochlore phase and reduced grain size with a small amount of amorphous helped to obtain a small polarization switching hysteresis and large breakdown field strength, and thus achieve an ultrahigh energy density of 182 $J \bullet cm^{-3}$ with an efficiency of 78 % in the high-entropy film of x = 0.4(Fig. 20 (**g**)), overwhelming a series of other dielectrics reported. Besides, the pyrochlore thin film exhibited good charging-discharging reliability (Fig. 20 (**i**)) and temperature dependence (Fig. 20 (**j**)) of the energy storage properties.

In addition, a substantial enhancement of energy storage performance was also demonstrated in high-entropy (K,Na)NbO_3 (KNN)-based ceramics by Chen et al. [300], prepared high-entropy (K,Na)NbO_3 (KNN)-based ceramics. The results demonstrated that the local random field increases by the introduction of multiple elements (i.e., Li, Bi, Ba and Sc, Hf, Zr, Ta) which enabled the coexistence of rhombohedral-orthorhombic-tetragonal-cubic (R-O-T-C) multiphase structures at room temperature (Fig. 21**a**)) and enhanced the local polymorphic distortion (Fig. 21**(b)**). Thus, the high-entropy composition showed smaller and more diverse polar nano-regions with a size of 1–3 nm than that of the low-entropy composition. Such a scenario observably delays the polarization saturation and produces a high efficiency (η of ~ 90.8%) (Fig. 21**(c)**). Besides, benefiting from the high entropy induced submicron grain (~ 600 nm) with a uniform and dense structure, a high breakdown field strength was also obtained and therefore realize a high recoverable energy storage density (W_{re} of ~ 10.06 $J \bullet cm^{-3}$) (Fig. 21**(c)**), which outperforms most of the recently reported ceramics, e.g., the $AgNbO_3$ (AN), (Bi,Na)TiO_3 (BNT), $BaTiO_3$ (BT) and $NaNbO_3$ (NN) (Fig. 21**(d)**).

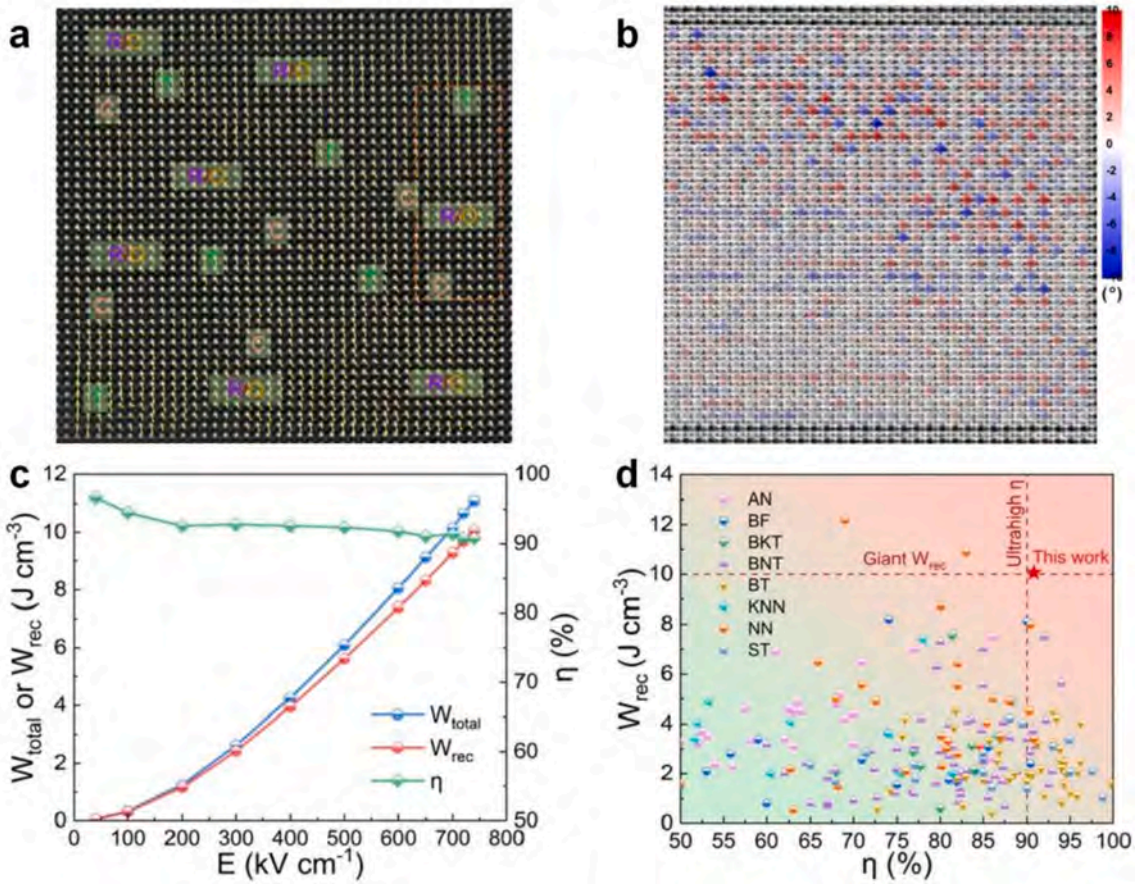

Fig. 21. (a) Atomic-resolution HAADF STEM polarization vector image of high-entropy KNN based ceramics along $[100]_c$. (b) Atomic-resolution Annular bright-field (ABF) STEM image along $[100]_c$ as well as the calculated oxygen octahedral tilt along y axis(blue and red indicate clockwise and anticlockwise tilt, respectively). (c) Total energy density (W_{total}), recoverable energy storage density (W_{rec}), and efficiency (η) as a function of electric field (E) for high-entropy KNN ceramic. (d) Comparisons of W_{rec} versus η between high-entropy KNN ceramic and other reported lead-free ceramics. [300] (Reproduced). Copyright © 2022, The Author(s). (For interpretation of the references to colour in this figure legend, the reader is referred to the web version of this article.)

4.4. Lithium batteries property

Recently, HEOs have gained considerable attention as electrode materials for lithium-ion batteries (LIBs), solid electrolytes (SEs), and catalysts for lithium metal batteries, thanks to their interesting "Cocktail Effect" and great potential for tailored energy storage properties. Benefiting from the cation tunability, HEOs offer several benefits as anodes for LIBs, especially their multi-electron redox mechanism and structural stability arising from the high entropy effect. These characteristics help to reduce volume expansion of electrodes and improve cycling performance [301].

According to various crystal structures, HEO used in LIBs electrodes can be mainly divided into rock-salt, spinel, and perovskite phases. In particular, spinel HEOs with AB_2O_4 formulation that have two Wyckoff sites confer them variable valence states and abundant oxygen vacancies, forming a special three-dimensional lithium ion transport mechanism and exhibiting considerable reversible capacity, which is believed to be a promising candidate as anode for LIBs [10,302]. Nevertheless, the electrochemical mechanisms of spinel HEOs are not clear, and there is a debate about whether spinel HEOs can maintain a stable single phase during the charging/discharging processes. For example, Patra et al. [303] synthesized a single phase $(CrNiMnFeCu)_3O_4$ and found a spinel to rock-salt transition that happened in the first lithiation process, even if it exhibited almost no capacity decay after 400 cycles.

Generally, for anode application, HEOs require both electroactive and inactive composition, where the latter acts as a structural pillar to maintain the stability of HEOs and prevent the agglomeration of active particles [301,303]. Elements of Mg, Ti and Al have been studied to stabilize HEOs by virtue of being inactive within the electrochemical window [304–306]. However, introducing inactive elements into HEOs may result in a lower capacity as they do not participate in redox reactions during the charge–discharge processes. For this reason, some HEOs were successfully synthesized without additional inactive elements. Nguyen et al. designed a non-equimolar spinel $(CrMnFeNiCu)_3O_4$ with metal cations dispersed in the A and B sites of the AB_2O_4 spinel lattice. Benefiting from its various valence states and all metal cations that are electroactive, the HEO achieved a high capacity of 1235 $mA \bullet h \bullet g^{-1}$ [10].

Despite of inactive compositions, electroactive elements play a decisive role in regulating battery performance. Various transition metals (TM) such as Cr, Mn, Fe, Co, and Ni have been intensively studied, especially Co element, which is capable of realizing superior battery performance thanks to its high conductivity and great compatibility with other elements [303]. To explore the role of different metal cations, a single phase $(Co_{0.2}Cu_{0.2}Mg_{0.2}Ni_{0.2}Zn_{0.2})O$ was synthesized and the corresponding medium-entropy compounds without Zn, Cu, and Co elements were prepared separately for comparison. It was found that the removal of Zn and Cu did not impede the overall cycling performance, whereas the cell experienced a rapid and completed failure without Co element, demonstrating the essential role of Co in achieving high capacity and good cycling stability [123].

However, considering the high cost and uneven distribution of Co element, significant efforts have been made to design Co-free HEOs [302,303,307,138]. A spinel $(CrMnFeNiCu)_3O_4$ HEO was successfully synthesized by Luo et al. [307], demonstrating steadily cycled for 150 cycles at 500 $mA \bullet g^{-1}$. With the help of operando quick-scanning XAS, they found that $Mn^{2+}/^{3+}$ and $Fe^{2+}/^{3+}$ underwent a two-step conversion reaction to form metallic phases, while Cr^{3+} was first reduced to CrO and then Cr^0 during lithiation. Interestingly, Ni and Cu, as the generally considered electroactive components, was less preferred to be oxidized during de-lithiation. In addition to Co, Ni is another important composition deployed in HEO based anodes, and is believed to be essential to stabilize the structures of HEOs and participate in redox reactions [303,123,308].

In summary, a suitable composition and well-designed structure, which can balance high capacity and long-term cycling stability, need to be carefully considered to fabricate advanced HEO-based anodes. Doping metal cations with the variety of valence states and regulating deficiencies to promote Li^+ migration offer intriguing possibilities of achieving the target.

In addition to the application of HEOs as anodes in LIBs, there has been increasing interest in exploring the use of HEOs as active materials and coatings for cathodes. These studies focus on their potential to improve the structural stability of cathodes, suppress side reactions, and enhance battery performance [309]. Similar to strategies for anodes, modulating interactions between various metal cations in HEO-based cathodes is one of the most important issues. Lun et al. [12] explored how the high entropy concept acted on

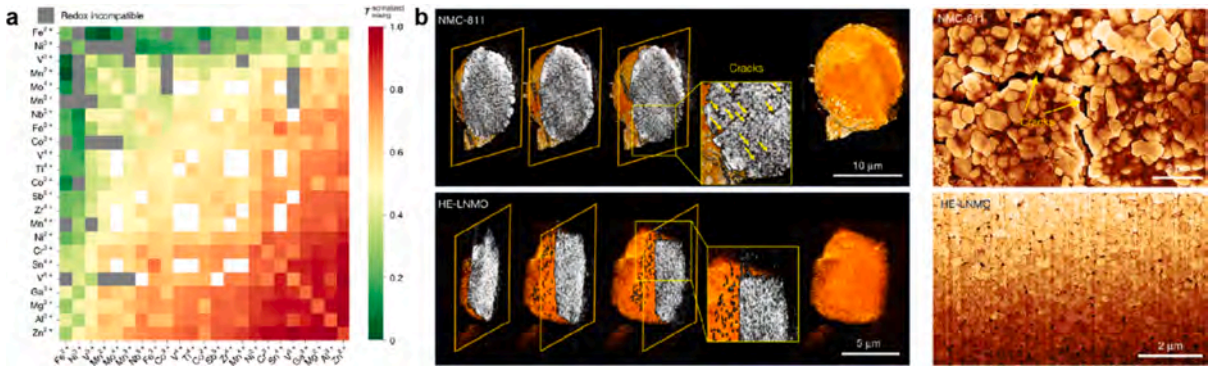

Fig. 22. (a) Normalized mixing temperature of different TM species in DRX compounds. From green to red represent increased incompatibility and grey means redox incompatible couples [12] Copyright © 2020 Springer Nature. (b) Comparison of structural and mechanical stability of HE-LNMO and NCM811 after 100 cycles [87]. Copyright © 2020 Springer Nature. (Reproduced). (For interpretation of the references to colour in this figure legend, the reader is referred to the web version of this article.)

cathodes by comparing rocksalt-type cathodes containing 2, 4 or 6 TM species. The results showed that as the TM species increased, same long-range order had been preserved with short-range order decreased, leading to higher energy density and rate capacity. A disordered rocksalt (DRX)-type cathode with a formula of $Li_{1.3}Mn_{0.1}Co_{0.1}Cr_{0.1}Mn_{0.1}Ti_{0.1}Nb_{0.1}O_{1.7}F_{0.3}$ was thus fabricated and achieved 955 $Wh \bullet kg^{-1}$ at 20 $mA \bullet g^{-1}$, and 170 $mAh \bullet g^{-1}$ when cycled at 2 $A \bullet g^{-1}$. They further used DRX-type materials as a platform to evaluate the compatibility and functions of 23 TM in high entropy cathodes (Fig. 22**(a)**) [12]. Double-redox centers, such as Mn^{2+}(Mn^{2+}/Mn^{4+}) and V^{3+} (V^{3+}/V^{5+}), are found to be highly preferred to corroborate into DRX-type cathodes for their good chemical compatibility and high electron capacity. Fe^{2+} and Ni^{3+} show outstanding compatibility with other TMs. However, large overlaps with oxygen oxidation cause them to become one-electron redox centers, which is not conducive to improving cathode capacity. In addition, high-valence non-redox-active species like Ti^{4+} and Nb^{5+} have promising potential to be introduced into HEO cathodes as charge compensators to further improve battery performance.

Except for choosing suitable cations and increasing species of TM, fluorine has been also introduced into the anionic sub-lattice of HEOs to improve the working potential of cathodes [12,310,20]. Because of similar ionic radius, partial occupation of oxygen sites by fluorine would bring in less strain into the structure, which is beneficial for maintaining good structure stability for long-term cycles. In addition, a rocksalt-type material, $Li_{0.94}(Co_{0.21}Ni_{0.21}Zn_{0.2}Mg_{0.2}Cu_{0.18})O_1F_{0.87}$, was synthesized by a facile ball-milling process with HEO and LiF, which showed a high working potential of 3.4 V vs Li^+/Li, compared to 1.0 V for the (CoMgCuNiZn)O [310,216].

Apart from rocksalt cathodes, layered structure cathodes like $LiNi_{1-x-y}Mn_xCo_yO_2$ (NMC) and $LiNi_{1-x-y}Co_xAl_yO$ with high Ni and low Co content have been long pursued. However, their chemo-mechanical and thermal instabilities, driven by irreversible phase transformations, transition metal dissolution, lattice oxygen loss, inter- and intra-granular cracking, and poor air stability, remain catastrophic issues for both battery performance and safety, especially in high state of charge (SOC) conditions [311]. In this case, HEOs have great advantages in suppressing anisotropy lattice strain and maintain the structural stability of cathodes, as well as improve thermal stability. For instance, layered O3-type HEOs have been investigated as intercalation-type cathodes for LIBs as the entropy stabilization can stabilize the O3-type structure and lattice [216]. Combining a new doping strategy with a typical co-precipitation method, Zhang et al. successfully fabricated a high-Ni, zero-Co layered cathode, $LiNi_{0.8}Mn_{0.13}Ti_{0.02}Mg_{0.02}Nb_{0.01}Mo_{0.02}O_2$ (HE-LNMO), which showed nearly zero strain and without cracks could be observed during the lithiation/de-lithiation process, whereas intergranular cracks were found in $LiNi_{0.8}Mn_{0.1}Co_{0.1}O_2$ (NCM811) after 100 cycles (Fig. 22**(b)**). Meanwhile, it exhibited enhanced superior thermal stability compared to $LiNi_{0.5}Mn_{0.3}Co_{0.2}O_2$. The improvement can be explained by the pinning effects of dopants, which further reduce oxygen loss and detrimental rock-salt transition [87]. Recently, Liang et al. developed an *in situ* high-entropy doping strategy combined with a single-crystalline design to fabricate the layered $LiNi_{0.88}Mn_{0.03}Mg_{0.02}Fe_{0.02}Ti_{0.02}Mo_{0.02}Nb_{0.01}O_2$ cathode. This design successfully reduced the lattice strain of the layered cathode with ultra-high Ni and zero Co content, and suppressed the H2-H3 transition, thus alleviating lattice oxygen loss and improving the structural stability. Accordingly, the assembled pouch cell exhibited exceptional cycling stability with a capacity retention of 80.6 % after 3500 cycles within 2.8 to 4.3 V, and 91.1 % after 1000 cycles with a high cut-off voltage of 4.5 V [312].

Considering that strain propagation and structural deterioration generally originate from surface reconstruction of cathodes, introducing high-entropy to modify the surface of layered cathodes has also been explored as an effective way to improve structural stability and enhance battery performance. For instance, Zhao et al. designed an epitaxial entropy-assisted coating strategy via a surface fusion process between Wadsley-Roth phase-based oxides and layered $LiNi_xCo_yMn_{1-x-y}O_2$ ($x \geq 0.9$) cathodes. Within the coating, the cathode exhibited suppressed lattice displacement and anisotropic volume change during the electrochemical process, enabling good stability of the cathode even when charging beyond 75 % SOC [311]. In addition, surface high-entropy strategies were also applied in Li-rich Mn-based layered cathodes to enhance cathode stability. Yang et al. induced Mg, Zn, Cu, and Nb elements into $Li_{1.2}Ni_{0.13}Co_{0.13}Mn_{0.54}O_2$ particles to fabricate the cathode with surface high-entropy architecture, which is beneficial for broadening the nonbonding O_{2p} bands. The improved overlap between the non-bonding O_{2p} and the (transition metal-O)* occupied state successfully suppressed the irreversibility of oxygen redox and enhanced lattice structural stability. With the surface high-entropy design of the Li-rich Mn-based layered cathode, the assembled battery exhibited good long-term cycling stability with 80.5 % capacity retention over 400 cycles [313].

Despite numerous efforts of adapting HEOs as cathodes of LIBs mentioned above, capacity fading mechanisms of both DRX and layered HEO cathodes need to be further investigated, as rapid capacity decay and initial capacity loss have been observed [12,314–316]. For instance, Zheng et al. revealed that the formation of M_3O_4 phase at the surface of layered $LiNi_{0.2}Co_{0.2}Mn_{0.2}Fe_{0.2}Al_{0.2}O_2$ impeded the intercalation of Li^+, which was responsible for low initial Coulombic efficiency and rapid capacity decay [316].

Besides the applications for LIBs, there are a few investigations of HEOs in lithium-metal batteries, which mainly focused on catalysts for lithium-sulfur batteries and solid electrolytes (SEs) for solid-state batteries (SSBs).

The “Shuttle effect”, one of the most serious issues to influence performance and impede the application of lithium-sulfur batteries, can be alleviated by modulating interactions between metal cation centers of catalysts and soluble polysulfides [317]. However, various intermediate polysulfides show different degrees of lithiation and solubilities, which pose great difficulties for rational mono metal-based catalysts [318]. Benefiting from multiple metal cations of HEOs, *d-p* orbital interactions between polysulfides and HEOs can be well modulated by synergistic effects of various metal cations. Perovskite HEOs (e.g. $La_{0.8}Sr_{0.2}(Cr_{0.2}Mn_{0.2}Fe_{0.2}Co_{0.2}Ni_{0.2})O_3$) [318], spinel HEO (e.g. $(Mg_{0.2}Mn_{0.2}Ni_{0.2}Co_{0.2}Zn_{0.2})Fe_2O_4$) [319] and rock-salt HEO [320] have been used as sulfur hosts to anchor polysulfides and facilitate redox reactions in lithium-sulfur batteries. However, the reaction mechanisms of HEO-based sulfur hosts need to be further explored as the redox processes become more complicated. Furthermore, fabricating pouch cells to simulate a more realistic battery operating condition is also crucial in investigating the application possibilities of HEO cathodes.

SSBs, considered as one of the possibilities for future commercialization, have become a hot topic in recent years. However, SEs

usually exhibit lower ionic conductivity compared to liquid electrolytes [321]. To this end, several strategies have been developed to increase ionic conductivity of SEs. For instance, Zeng et al. [236] proved the ability of HEOs to improve the ionic conductivity of lithium (Li)-sodium (Na) superionic conductor (Li-NASICON), sodium NASICON (Na-NASICON), and Li-garnet structures $Li_7La_3Zr_2O_{12}$ based framework. They drew a hypothesis that local distortions induced by the chemical disorder of high entropy would lead to an overlapping distribution of site energies, which was beneficial for ion hopping. Macroscopic diffusion would be further promoted by the disorder if percolation formed in the network of sites with similar energies [236]. Besides, oxygen vacancies which originate from charge compensation mechanisms of HEOs are considered to facilitate Li-ion transport in HEO based SEs [322,323]. The family of rock-salt structures $(MgCoNiCuZn)_{1-x-y}Ga_yA_xO$ (with A = Li) showed high ionic conductivity of 10^{-3} $S\ cm^{-1}$ at room temperature when x was 0.3. It was found plentiful surface oxygen vacancies involved in the HEO, which created abundant Li ion transport pathways [322]. Moreover, HEOs with plentiful oxygen vacancies are also used as fillers in composite SEs like Poly(ethylene oxide) (PEO) based SEs, which not only improve ionic conductivity but also extend potential windows of polymer matrix [324].

4.5. Catalytic property

High-entropy oxides have recently attracted intensive research attention due to their potential applications in diverse catalysis processes, due to their superior thermostability and variable chemical properties [325,326,18,327,328]. In particular, HEOs demonstrate huge potential for a broad application prospect in the field of catalysis. In heterogeneous catalytic applications, on one hand, HEOs can play a role in active catalysts, where the high entropy effect can result in unique properties such as active sites formation and adjustable electronic structures by the interaction of multiple elements. On the other hand, due to the excellent thermal stability and corrosion resistance of HEOs, one can apply HEOs as excellent supports for anchoring transition metal catalysts and noble metal species. Multiple elements with various oxidation states in HEOs lead to the formation of oxygen vacancies which can help to stabilize the metal species even under harsh environments. Besides, the combination of multiple metal cations can lead to cocktail effects, where the presence of one element might enhance the catalytic properties of another and thus result in improved activity, selectivity, and efficiency in catalytic processes.

(1) HEOs as active catalysts

HEO-based materials as active catalysts have been explored for other types of low-temperature thermal catalytic reactions. Li et al. [329] designed and synthesized single-phase denary multi-element oxide (Zr, Ce, Hf, Ti, La, Y, Gd, Ca, Mg, Mn)O_{2-x} nanoparticles (NPs) with tunable composition, size and structure using a rapid synthesis and screening approach (Fig. 23). These particles demonstrated superior high performance and stability for catalytic methane combustion over 100 h. In addition, a holey lamellar $Co_{0.2}Ni_{0.2}Cu_{0.2}Mg_{0.2}Zn_{0.2}O$ HEO catalyst was prepared using a straightforward anchoring-merging reaction route. This catalyst exhibited ultra-high efficiency for solvent-free aerobic atmospheric oxidation of benzyl alcohol [330]. The presence of rich oxygen vacancies and exposed catalytic sites in the HEOs catalysts resulted in a significantly enhanced catalytic efficiency, reaching a conversion rate as high as 98 % at 120 °C in 2 h.

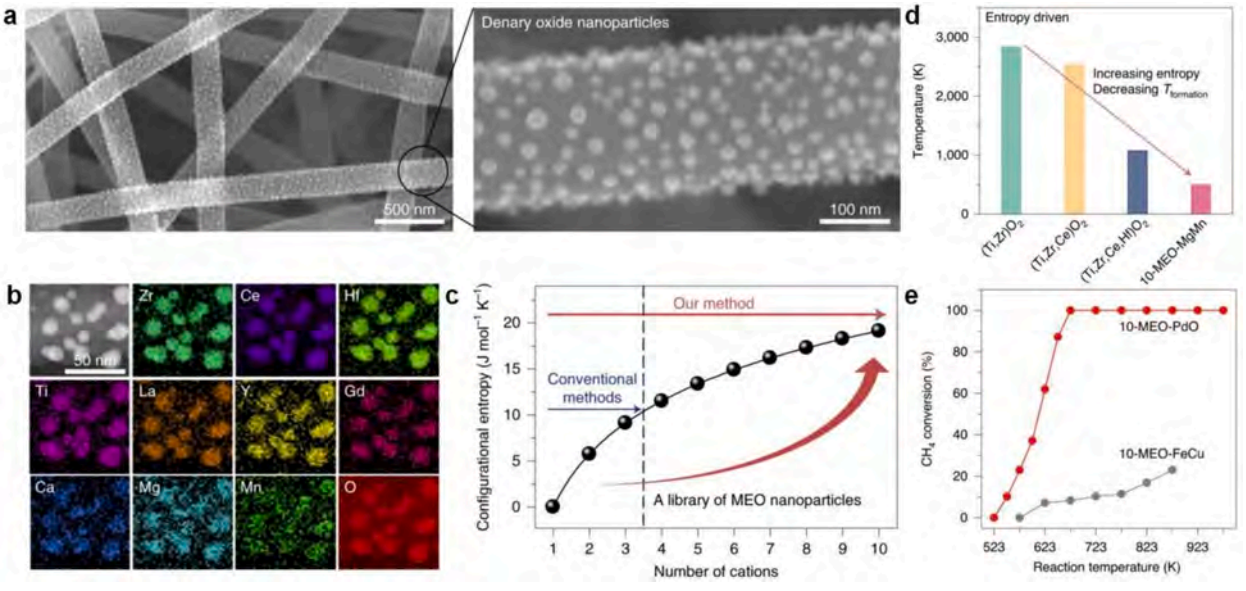

Fig. 23. (a) SEM images showing 10-MEO-MgMn NPs uniformly dispersed on conductive carbon nanofibres (CNFs). (b) Elemental maps of 10-MEO-MgMn NPs composed of ten cationic elements(Zr, Ce, Hf, Ti, La, Y, Gd, Ca, Mg and Mn) and oxygen. (c) configuration entropy as a function of the number of cations. (d) The formation temperature of $(Ti,Zr)O_2$, $(Ti,Zr,Ce)O_2$, $(Ti,Zr,Ce,Hf)O_2$ and 10-MEO-MgMn derived from DFT calculations. (e) CH_4 conversion of $(Zr,Ce)_{0.6}(Mg,La,Y,Hf,Ti,Cr,Mn)_{0.3}Pd_{0.1}O_{2-x}$ (10-MEO-PdO) and other control sample of $(Zr,Ce)_{0.6}(Mg,Hf,Ti,Cr,Mn,Fe,Cu)_{0.3}Pd_{0.1}O_x$ (10-MEO-FeCu). [329] (Reproduced). Copyright © 2021 Springer Nature.

Besides, recent studies have started to consider HEOs as catalysts in electrochemical water-splitting, which is regarded as a promising renewable technology to generate H_2 from water without carbon emissions. The widespread commercialization of electrochemical water-splitting faces obstacles due to the slow oxygen evolution reaction (OER) at the anode and the high cost of current noble metal-based electrocatalysts, such as RuO_2 and IrO_2. Related studies have shown that HEOs are promising candidates for future earth-abundant, robust, and efficient OER catalysts, exhibiting superior OER activity and excellent electrochemical stability due to the synergistic effects of the multiple cations and the high entropy configuration effect [137,73,100,331–342].

For instance, Tang et al. [332] employed a straightforward sol–gel method to prepare a high-entropy perovskite cobaltate, consisting of five equimolar metals (Mg, Mn, Fe, Co, and Ni) in the B-site, as an electrocatalyst for OER. The as-prepared cobaltate HEOs exhibited a lower overpotential (320 mV at 10 $mA \bullet cm^{-2}$) and a low Tafel slope (45 $mV \bullet dec^{-1}$), surpassing electrolytes with much higher cobalt concentrations (Fig. 24). Moreover, non-noble metal-based FeCoNiPB amorphous HEOs were utilized for OER in alkaline media [333], exhibiting overpotentials of 235 and 306 mV at current densities of 10 and 100 $mA \bullet cm^{-2}$, respectively. More recently, Kante et al. [169] revealed the (001) facet of $LaCr_{0.2}Mn_{0.2}Fe_{0.2}Co_{0.2}Ni_{0.2}O_{3-\delta}$ is highly active for catalyzing the OER, outperforming all of its parent compounds with 17 to 680 times higher currents at a fixed overpotential. These findings suggest that HEOs offer a new and promising type of earth-abundant and highly active materials for OER electrochemical catalysts, endowing the fine-tuning the activity beyond the scaling limits of traditional mono- or bimetallic oxides.

Furthermore, electrochemistry offers a simple and reliable method for the efficient utilization of ammonia, a promising energy carrier owing to its carbon neutral characteristics and low cost for long-range transportation. Despite the intense research efforts directed to electrocatalytic nitrogen reduction reaction (NRR), the NH_3 yield and selectivity are still relatively low for practical applications. The introduction of HEOs as NRR catalysts provides an exciting opportunity due to their multi-metal synergistic effects and entropy increase effects [343–345]. For instance, He et al. [343] reported high entropy (Mn, Fe, Co, Ni, Cu)$_3O_4$ oxides, which exhibited high electrocatalytic activity for NRR in non-aqueous solutions. The onset overpotential of (Mn, Fe, Co, Ni, Cu)$_3O_4$ is 0.70 V, which is nearly 0.2 V lower than their most active single metal cation counterpart. In addition, Sun et al. engineered urchin-shaped hollow $(Ni_{0.20}Co_{0.16}Fe_{0.24}Mn_{0.18}V_{0.22})_3O_4$ HEOs nanospheres assembled from 2D nanosheets [345], demonstrating excellent electrocatalytic activities of HEOs for NRR with a NH_3 yield rate of 47.58μg h^{-1} mg^{-1} and Faradaic efficiency (FE) of 10.74 %. Further mechanism studies are needed to reveal the relationship between high NRR performance and their unique electronic structures, multi-metal synergistic and entropy increase effects.

Additionally, the introduction of HEOs with entropy-stabilization features has shown promising potential photocatalytic

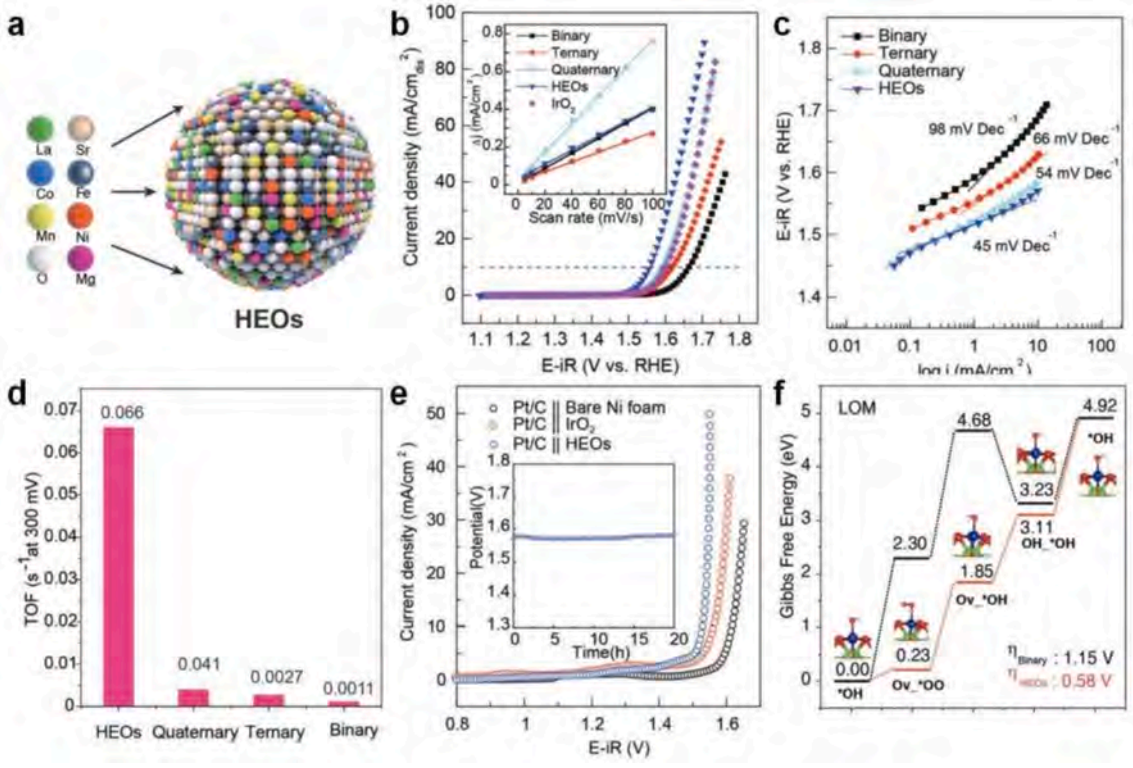

Fig. 24. (a) Schematic demonstration of the structure of perovskite HEOs NPs with uniformly dispersed elements. (b) Polarization curves of samples with different configuration entropy compared with IrO_2. (c) Tafel plots and (d) turnover frequency (TOF) values of various catalysts at an overpotential of 300 mV. (e) Stability test of HEOs in two-electrode configuration electrolyzer. (f) Lattice oxygen-participated mechanism (LOM) on HEOs and binary surface at a potential of 0 V. [332] (Reproduced) Copyright © 2022 Wiley-VCH GmbH.

applications in recent years [346–349]. Edalati et al. [346] firstly synthesized high-entropy photocatalyst $TiZrHfNbTaO_{11}$ with *d*0 electronic configuration by mechanical alloying followed by high-temperature oxidation. This material exhibited predominant photocatalytic hydrogen production [347] and CO_2 conversion activity [348], with high chemical stability, suggesting the high potential of high-entropy oxynitrides as advanced low-bandgap photocatalysts. Similarly, a five phase $TiZrNbTaWO_{12}$ with 10 heterojunctions together with an overall low bandgap realized in oxygen production of 12.1 $\mu molh^{-1}m^{-2}$ under visible light [350].

(2) HEOs as supports for metal-oxide catalysts

The extraordinary thermal stability and abundant oxygen vacancies in HEOs result in their potential to be candidates as catalyst supports for metal nanostructures, especially for noble metal species that are not stable in harsh environment of heterogeneous catalysis. Currently, HEOs have been used for stabilizing noble metals with the range from single metal sites, clusters consisting of several atoms, to nanoparticles.

Low-temperature CO oxidation has long been investigated as a model reaction in the catalysis field for applications in automotive exhaust treatment and air purification. Despite the advancements, developing catalysts with high CO oxidation activity at low-

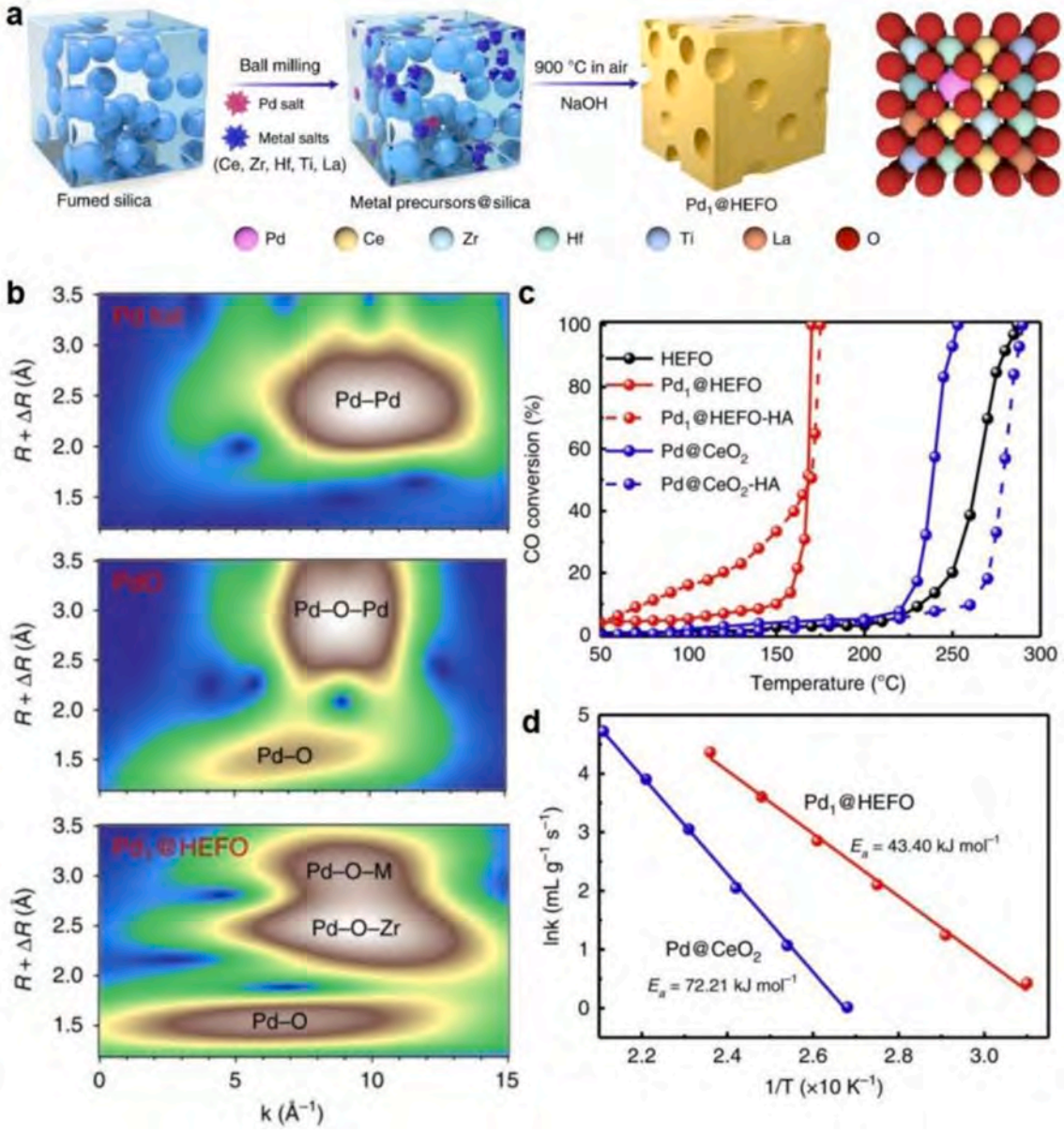

Fig. 25. (a) Schematic illustration of dispersion and incorporation of Pd single atoms on the surface and sub-lattice of HEOs after calcination. (b) The wavelet transforms from experimental data for Pd_1@HEOs, PdO, and Pd foil. (c) CO oxidation performance of different catalysts before (solid lines) and after (dashed lines) hydrothermal treatments.(d) Arrhenius plots of Pd_1@HEOs and Pd@CeO_2 [183]. (Reproduced). Copyright © 2020 U. S. Government Works.

temperature and high stability remains a great challenge. Recently, HEOs composing various transition metals with high oxidation states have been investigated for low-temperature CO oxidation, either as catalysts or supports [351,352]. For example, Chen et al. [352] developed a metal-tannin coordination assembly strategy to fabricate La(FeCoNiCrMn)O_3 HEOs nanoparticles (NPs) with 10 immiscible metal elements. The nanoparticles, ranging in sizes from 10-30 nm and featuring abundant oxygen vacancies, exhibited enhanced CO oxidation activity compared to single metal-oxide perovskites catalysts. In another noteworthy study, Xu et al. reported a novel entropy-driven strategy to stabilize Pd single-atom on (CeZrHfTiLa)O_x HEOs as the support. This was achieved through a combination of mechanical milling and calcination (Fig. 25), leading to the formation of stable Pd-O-M bonds (M = Ce/Zr/La). The resulting Pd/HEOs sample not only demonstrated superior low-temperature CO oxidation activity but also showed outstanding resistance to thermal and hydrothermal degradation [183].

In addition, HEOs have been also proven to be highly effective for CO_2 hydrogenation reactions when used as metal-supports [13,14]. A method for *in situ* generation of CuCoNi nanoalloys on $Co_3MnNiCuZnO_x$ HEOs matrix has been reported, wherein a sintering-resistant metal-oxide interface with a strong interaction was created by H_2 reduction treatment [13]. This resulted in enhanced CO_2 hydrogenation performance compared to the binary $CoMnO_x$ counterpart catalyst, with CO_2 conversion rate of 46 % vs. 30 % after 100 h at 500 °C. The study revealed that *in situ* grown transition-metal species on high-entropy $Co_3MnNiCuZnO_x$ were more thermally stable, owing to their maximum entropy motivation. Furthermore, Hou et al. [14] demonstrated that high entropy cubic $Zr_{0.5}(NiFeCuMnCo)_{0.5}O_x$, when used as a host model, could promote the *in situ* reversible exsolution-dissolution self-regeneration process of supported metallic species during multi-redox cycles.

From HEOs as active materials and supports for metal-oxide catalysis, the elements selected are mostly transition metal ions such as Mn, Fe, and Co, which can exhibit multiple oxidation states. Therefore, HEOs usually exhibit mixed valence states and benefit complex redox reactions. However, increasing elements involved adds to additional complexity in the reaction mechanism and the structure–activity-selectivity relationship. For hydrogen evolution reactions (HER), CO_2 reduction, and reforming reactions, Ni is a star element for absorption and activation of gas modules [353]. For OER, Co and Ni showed a dominating catalytic activity [354,355]. Zr and Zn usually contribute to structural stability. Besides, the diversified elements can induce subtle strain at the atomic level, altering metal–oxygen bond lengths and modulating the adsorption energies of reaction intermediates (e.g., *O, *OH), thereby improving the catalytic efficiency for OER. The combination of a series of elements to constitute a group of rather continuous overpotential and activity can realize an overall improved catalytic performance [120].

4.6. Magnetic property

Magnetism is a fundamental physical phenomenon that arises from the motion of electric charges and leads to a broad range of applications and manifestations, ranging from traditional magnetic memory storage devices to advanced applications in spintronics and emerging quantum sensing and computing technologies [356–358]. At the atomic level, the magnetic properties of materials are governed by the behavior of electrons, particularly their spins, which are quantum entities that have no classical analog.

The emerging studies on entropy in magnetism start from HEAs, showing great scope to tune magnetic properties with excellent mechanical behaviors [359]. Different from HEAs whose magnetic properties are largely dictated by metallic bonding and exchange interactions between delocalized *d*-electrons of transition metals, the magnetism of HEOs is more complex in electronic structures due to the presence of oxygen. Compositionally disordered but positionally ordered lattices of HEOs greatly simplify the ability to create stable materials with very specific macroscopic magnetic responses and randomly distributed strengths of magnetic exchanges, which means the coexistence of shifting local variances in spin and coupling types as well as maintained position symmetries. The coordination geometry, valence, spin state and type of the metal cations hybridized with the bridging oxygen in HEOs are strongly correlated with the diversity of neighboring ionic configurations, thus allowing a greater access to functional diversity.

$(Co_{0.2}Cu_{0.2}Mg_{0.2}Ni_{0.2}Zn_{0.2})O$ was firstly synthesized with long-range ordered antiferromagnetic behavior below T_{Neel}, which can be understood by super-exchange interactions [360,361]. By substituting magnetic elements with other non-magnetic elements, the HEOs host either an antiferromagnetic order or spin-glass state depending on the amount of magnetic ions. The HEO with two magnetic ions, $(MgNiCuZn)_{0.8}(LiGa)_{0.2}O$, $(MgCoCuZn)_{0.8}(LiGa)_{0.2}O$, and $(MgCoNiZn)_{0.8}(LiGa)_{0.2}O$, exhibited a glassy state which can be attributed to the disconnected magnetic exchange paths because of the reduced content of magnetic ions. The isolated magnetic domains likely gave rise to a magnetic cluster-glass behavior. The magnetic transition temperatures were also substantially reduced. These results demonstrated the ability to tune the degree of glassiness in the antiferromagnetic structure of HEOs [362]. Among all elements, change in the concentration of Cu^{2+}, unique among other elements in this case, usually results in a significant change in the crystal structure due to its pronounced Jahn-Teller effect and the valence of Co sites, which extends to dilution and disorder of the magnetic lattice [363]. For other studies of rock-salt HEOs, (Mg,Mn,Fe,Co,Ni)O can realize a stabilization of Mn^{2+} and Fe^{2+} ions [364].

For spinel structure HEOs, it is more capable of supporting a diverse range of magnetic interactions (e.g., ferromagnetic, antiferromagnetic, and ferrimagnetic) between cations at different sites. The optical floating zone growth technique was applied to synthesize $(MgMnFeCoNi)Al_2O_4$ in a cluster spin glass state by Mao et.al. [365]. $Mn_{0.2}Co_{0.2}Ni_{0.2}Cu_{0.2}Zn_{0.2}Fe_2O_4$ synthesized by a solution-combustion method exhibited ferri- or ferromagnetic properties with a high saturation magnetization at low temperatures (up to 108 emu/g at 5 K) while a magnetic hysteresis for a sample calcined at 500 °C. In this material, Mn and Fe showed the coexistence of both 2 + and 3 + valence states [366]. A case study of $(CrFeMnCoZn)_3O_4$ and $(CoCrFeNiZn)_3O_4$ nanocrystalline powders showed that nonmagnetic Zn^{2+} substitution for either magnetic Co^{2+} or Ni^{2+} would weaken the ferromagnetic ordering and magnetic moments [140].

For perovskite structure HEOs, $(La_{0.2}Nd_{0.2}Pr_{0.2}Sm_{0.2}Eu_{0.2})_{1-x}Sr_xMnO_3$ ($0 \leq x \leq 0.5$) exhibited a structural transformation from *Pbnm* to *R-3c* with increasing Sr substitution and a prominent ferromagnetic ordering for $x \geq 0.3$ [367]. $(La_{0.2}Y_{0.2}Pr_{0.2}Nd_{0.2}Sm_{0.2})CrO_3$

showed an antiferromagnetic transition at about 210 K, and an interesting magnetization reversal and exchange bias effect at low temperatures [368]. Studies on La(Cr,Mn,Fe,Co,Ni)O_3 thin film proved continuously tunable critical temperatures of the dominant magnetic phase and the emergence of exchange bias responses. By varying the ratios of the elements (e.g., Mn) and their associated spin (*S*) and exchange (*J*) values, a range of magnetic phases could be achieved, including antiferromagnetic and ferromagnetic orderings, and even induce an exchange bias effect traditionally seen in heterostructured or nanocomposite materials [63].

Ionic and covalent bonding between cations and anions in HEOs can effectively maximize the number of microstates and thereby host homogeneous distributed multiple cations without disturbing overall crystallinity might be beneficial for magnetic insulator design. Sharma et.al. [369] highlighted the impact of strain on magnetic properties by epitaxial growth of single-crystal $(Mg_{0.2}Ni_{0.2}Fe_{0.2}Co_{0.2}Cu_{0.2})Fe_2O_4$ (which is based on nickel ferrites, a ferrimagnetic material commonly used) on various substrates (MgO, $SrTiO_3$, and $MgAl_2O_4$) to realize three states of strain modulation: compressive, tensile and relaxed. Compressive strain (on $MgAl_2O_4$ substrate) aligns the magnetic easy axis in-plane along with a reduced out-of-plane hysteresis loop, while tensile strain (on MgO substrate) aligns it out-of-plane with a pronounced out-of-plane hysteresis loop and higher coercivity in the out-of-plane direction compared to the in-plane direction. Room-temperature magnetic force microscopy (MFM) revealed that strained films on $MgAl_2O_4$ and MgO substrates exhibit stripe domain patterns. Besides, Jin et.al. reported a high-quality ultrathin 10 nm HEO epitaxial film $(CrMnFeCoNi)_3O_4$ for high-performance ferrimagnetic insulator (FMIs) that exhibited concurrently a superior saturation magnetization M_S (1198 $emu \bullet cm^{-3}$), low coercivity H_C (90 *Oe*), and excellent resistivity ρ (1233Ω• *cm*) as well as readily tunable magnetic anisotropy (as shown in Fig. 26 (**b**)). The huge lattice strain in the HEO thin film was believed to change the bond length and bond angle of chemical bonding between different ions, resulting in tilting the original 180° collinear antiferromagnetic moment and generating the net magnetic moment (Fig. 26 (**g**)). The lattice distortion also led to cation inversion and might improved M_S [370].

Studying the effect of a single element on overall magnetic behaviors is crucial yet studies are relatively deficient. A study by Ke et. al. [371] on $(Fe,Co,Ni,Cr,Mn)_3O_4$ oxide thin films showed that magnetic behavior is primarily driven by Mn^{3+} ions, whose orbital occupations are significantly influenced by the strain states. The strain modifies the energy levels of the eg orbitals of Mn^{3+}, affecting their preferred electron occupancy and driving the observed magnetic anisotropy. Studies of $(Mg,Cr,Mn,Co,Fe,Ni,Cu,Zn)(Cr,Fe,Al)_2O_4$ highlighted Cr^{4+} in some samples occurring at 300 K, indicating complex spinel configurations [372]. Oxygen vacancy may also significantly affect the magnetic coupling and further studies are still needed.

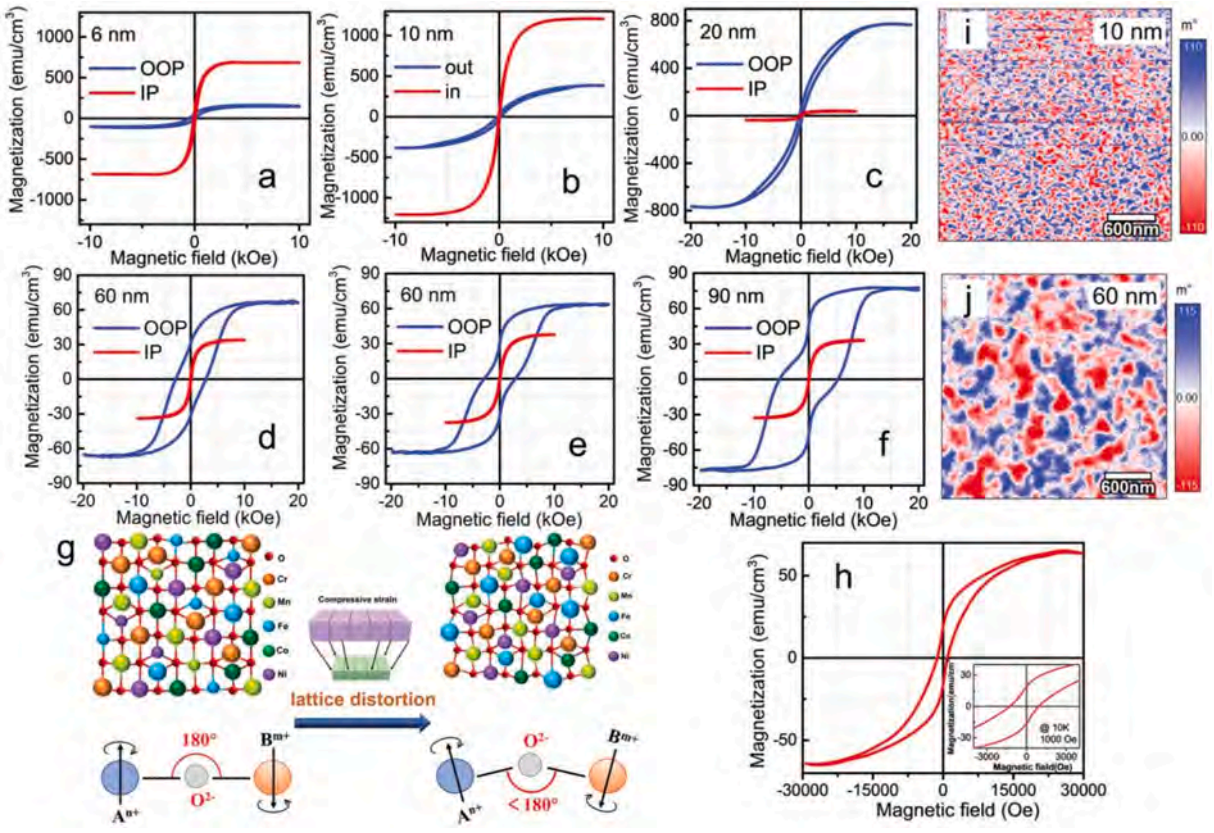

Fig. 26. Macroscale and mesoscale of magnetic properties characterization of a series of $(CrMnFeCoNi)_3O_4$ thin film with different thickness, from (a) 6 nm to (f) 90 nm. (g) Schematic illustration of antiferromagnetic moment tilting due to lattice distortion. (h) The exchange Bias curve of 60 nm films at 10 K. (i) and (j) MFM image of the 10-nm-thin and 60-nm-thick CMFCN film at 0 Oe, respectively [369]. Copyright © 2023 Wiley-VCH GmbH.

4.7. Supercapacitive property

Supercapacitors are widely used in various scenarios that require fast charging and discharging, such as hybrid electric/electric vehicles [373], renewable energy systems [374], and regenerative braking systems in hybrid and electric vehicles [375] as an electrochemical capacitor energy storage device with high power density, long cycle life and high safety. On the basis of their charge storage mechanism, supercapacitors can be classified as electrostatic double-layer capacitors (EDLCs), pseudo-capacitors and hybrid capacitors. EDLCs work on the charge storage mechanism and exhibit electrostatic capacitance, hence creating a double-layer structure at each electrode–electrolyte interface, while pseudo-capacitors work on reversible faradaic reaction mechanisms and exhibit electrochemical capacitance. Hybrid capacitors adopt both the mechanisms of EDLCs and pseudo capacitors, which are composed of electrodes with different characteristics based on both chemical and electrical mechanisms. The storage mechanism greatly depends on the nature of the materials used, either carbon based or redox active metal-based materials.

EDLCs usually consist of active porous electrodes, electrolytes and a dielectric substance that acts as an insulator and possesses electrical properties [376]. Pseudo-capacitors on the other hand, use electrodes made up of redox-active materials and conducting polymers, and electrolytes similar to EDLCs. Hybrid capacitors are composed of asymmetric capacitors and composite materials, with one electrode made from EDLC materials (e.g., activated carbon) and another from pseudocapacitive materials (e.g., metal oxides or conducting polymers).

High entropy alloys have been widely reported to fabricate supercapacitors with and also other high-entropy materials, such as carbides [377], antimonide [378], and hydroxide [379]. For HEOs, the entropy stabilization effect contributed to the high stability and thus prevent segregations, corrosion and degradation, and extend the cycle life. Besides, by structural design and selecting multiple divalent and trivalent metallic cations in a single unit cell broaden the space of tunning electrochemical energy storage performances. Different synthesis methods also lead to multi-diversified microstructures of HEOs, thus realizing tunable porosity for improved electrochemical energy storage performance. As a result, HEOs pave the way for future supercapacitors, maintaining a high specific capacitance with relative high conductivity and less structural collapse in the process of charging and discharging. The multivalent elements produce *d*-band states near the Fermi level and thus provide favorable intermediate intercalation/deintercalation kinetics, demonstrating promising performance on asymmetric supercapacitors [380]. Based on the characteristics above, HEOs are mostly applied as electrodes or active material in electrodes in supercapacitors, specifically for pseudo-capacitors and hybrid capacitors. The HEOs are battery-type materials, where the performance relies on accelerating the electrochemical kinetics processes via nanocrystallization and elemental doping. The stability deterioration caused by irreversible phase transitions is one of the factors limiting the application of those materials.

As for electrodes or active material in electrodes, spinel structure is one of the most studied since it supports the coexistence of divalent and trivalent ions, which enables a variety of redox reactions during the charge–discharge processes. Inverse spinel $(CuNiZnAlFe)_3O_4$ synthesized through sol–gel method and additional combustion realized a maximum specific capacitance of 2.02 $F \bullet g^{-1}$ at a scan rate of 5 $mV \bullet s^{-1}$ [381]. Inverse spinel electrode $(CuNiFeMnCo)_3O_4$ synthesized by sol–gel method realized a maximum specific capacitance of 34.24 $F \bullet g^{-1}$ at a scan rate of 5 $mV \bullet s^{-1}$ [382]. Pristine spinel $(CrMnFeCoNi)_3O_4$ nanoparticles synthesized using a facile soft-chemical approach were coated on nickel foam as a working electrode and the supercapacitor assembled showed an enhanced capacitance of 239$F \bullet g^{-1}$at a current density of 0.5 $A \bullet g^{-1}$ [383]. Additionally, new attempts of perovskite exploration emerge, such as $La(CoCrFeMnNiAl_x)_{1/(5+x)}O_{3-\delta}$ [384].

The electrochemical performance is highly dependent on crystallite size, pore size and morphology. Therefore, low-temperature methods such as RCP [385] and sol–gel method [381,382] are preferred to realize a porous structure with a relatively high crystallinity. A novel polyacrylamide gel method realized particle size of tens of nanometers and the mole ratio of acrylamide to metal cations (A/M) significantly influenced the average particle size of the nanopowders [386]. A single-step thermal plasma process also yielded synthesized particles with an average size of about 24 nm in a fast production rate of 1.5 $g \bullet \text{min}^{-1}$ and at a low discharge power (11 kW) [387]. The $(MnNiMoCoFe)_3O_4$ NPs with crystalline size ranging from 13 to 29 nm was prepared by the same method, exhibiting a specific capacitance of 215$F.g^{-1}$/26.9 $mA \bullet h \bullet g^{-1}$ at a current density of 2 $A \bullet g^{-1}$ in KOH electrolyte [388]. The polyethylene glycol as a sacrificial template was used to control the pore structure of HEO $(FeCoCrMnNi)_3O_4$ [389]. The HEO-based electrode with the highest surface area demonstrated the optimal electrochemical performance with an energy density of 53 $W \bullet h \bullet kg^{-1}$ and a power density of 400.8 $W \bullet kg^{-1}$. The effect of microstructure design was also demonstrated in $(FeCoCrMnNi)_3O_4$ electrode, in which the material synthesized via sol–gel methods exhibited improved energy density than the one prepared under reverse co-precipitation [390,383].

However, further understanding of element selection still needs to be deepened. The basic idea is to select elements with multiple oxidation states and thus provide rich redox-active sites that benefit pseudocapacitive capacitance. To further improve energy density, Yin et.al. [390] selected transition metal elements of Fe, Co, Cr, Mn and Ni to prepare spinel $(FeCoCrMnNi)_3O_4$ with a high specific surface area of 63.1 $m^2 \bullet g^{-1}$ via sol–gel method at a low calcination temperature of 450 °C. A wider potential window of (−1, 0.6) V was realized for the supercapacitor to operate safely, achieving a maximum capacitance of 332.2$F \bullet g^{-1}$ with an energy density of 103.8 $W \bullet h \bullet kg^{-1}$ and a power density of 225 $W \bullet kg^{-1}$ was obtained at a current density of 0.3 $A \bullet g^{-1}$.

The introduction of low-valence metal ions can facilitate the formation of abundant oxygen vacancies and active sites [391]. The $(FeCoCrMnZn)_3O_4$/Nickel Foam (NF) composite electrode was evaluated in a supercapacitor and the overall capacitance reached 340.3$F \bullet g^{-1}$ at a current density of 1 $A \bullet g^{-1}$ in a 1 M KOH electrolyte [392]. Oxygen vacancy was served as the electroactive center of the redox reaction with an increased concentration of charge carriers for O–H bond adsorption, leading to improved conductivity and specific capacitance [390].

HEOs composited with graphene fiber electrode presents promising performance in alkaline electrolytes for wearable

supercapacitors. Due to the poor conductivity, the conducting materials were compared to investigate the effect under different potential windows [393]. It seems that the intergrain/interparticle connection plays a crucial role in the performance of supercapacitors.

In addition, the distinct diffusion effects during cyclic test results in stability behaviors. Nan et. al. studied the ions intercalation reversibility of $La_{0.7}Bi_{0.3}Mn_{0.4}Fe_{0.3}Cu_{0.3}O_3$ electrode in an aqueous alkaline supercapacitor during the cyclic test [394]. The conductivity is another factor that determines the performance of supercapacitors [395]. The DFT calculation results suggested high-entropy material possessed a narrow energy band gap, thus a low energy barrier for electron transport.

Inspired by high-entropy materials, a multi-phase material was used to fabricate supercapacitors [396]. The nanoscale multi-phase electrodes present high specific capacity due to their high electrical conductivities and good ion transport abilities. In summary, HEOs in the application of supercapacitors could pave the way of balancing between the improvement in capacitance and overall stabilities, though it might sound contradictory to become active materials and contribute to structural stability. The metallic ions in HEOs constitute a relatively wide range of oxidation states and thus can be leveraged to form active sites. The oxygen matrix and the ionic difference between metallic ions contribute to resistance in structural collapse and corrosion since the overall distortion is much more modulable.

4.8. Structural perspective of the structure–property correlations

The fundamental aspects and applications of HEOs are intrinsically shaped by the high entropy effect on the structure–property relationship. It is challenging, however, to pinpoint the most impactful aspect of the high entropy effect on specific applications due to the complexity of their interrelations. For example, thermal conductivity stems from phonon scattering, which are quantized lattice vibrations [397] and thus has a strong correlation with lattice structures. The entropy stabilization aspect of the high entropy effect reduces phonon scattering time rather than velocities, and thus facilitates the reduction of thermal conductivity. Furthermore, the lattice distortion, another aspect of the high entropy effect, creates local stress fields and promotes a wide spectrum of lattice phonons. The thermal conductivity reduction does not necessarily correlate positively with an increase in entropy. However, regarding electrical properties, HEOs generally do not exhibit significant improvement in electrical conductivity, as a reduction in photon MFP often coincides with a decrease in carrier mobility. Nevertheless, HEOs inherently display colossal permittivity, which contributes to their high-level dielectric behaviors.

Detailed examinations of physical/chemical parameters such as scattering factors for thermal properties and their associated mechanism could provide valuable insight into the contributing factors' relative importance.

Besides, several applications of HEOs exhibit striking correlations, all rooted in a common structural origin. A notable example is the significant lattice distortion, which is primarily caused by atomic size mismatch. This distortion can trigger the symmetry transformation of average structures and create uneven local structures, promoting the formation of nanostructures such as grains, domains, and atomic displacements. Moreover, substantial lattice distortion can increase metal and oxygen vacancies, favoring unsaturated active site exposure for reactant adsorption and electron transfer in catalysis. The structure of HEOs, both in the short and long range, significantly impacts their functional performance. However, the mechanisms underlying structure features and functional behaviors still require further investigation. For thermoelectric and dielectric properties, the short-range high atomic disorder disrupts the long-range domain structure and simplistic phonon vibration, reducing both the polarization value and thermal conductivity. Specific HEO structure series exhibit relatively superior behavior in certain areas. For instance, pyrochlore structures are promising candidates for dielectric, energy storage, and thermal resistive properties due to their site complexity and stability. The unique features of pyrochlores compared to other structures warrant further exploration.

In addition to property-property correlations tied to structural origins, similar chemical processes drive structure–property optimization across diverse application fields. In lithium batteries and catalytic properties, for instance, local distortions, prompted by high entropy's chemical disorder, lead to a complex and adaptable site energy distribution that serves as the foundation for ion hopping, ion transport, and molecular binding. The lithiation and de-lithiation mechanisms of SSBs and LIBs are redox reactions akin to a self-regenerative catalyst. Notably, during lithiation, specific divalent metals in the transition metal HEO (TM-HEO) react with Li to form nano-Li_2O and nano-M nuclei trapped in the host matrix via a conversion reaction, disrupting long-range order. During de-lithiation, nano-Li_2O and nano-M nuclei diffuse back and metal ions re-incorporate into the crystal structure, aided by entropy's driving force [123].

Similarly, supported metal catalysts also require transition metal ions and noble metals to serve as active sites for catalytic reactions. These are typically designed as components of specific sub-lattice. Nanoparticles, synthesized via the exsolution process, transform into exsolutions or segregations socketed in the host oxides. The migration of active sites to the surface is a focal point in catalysis studies. Both the exsolution and dissolution can be voltage-controlled, aligning the reversible charge and discharge processes.

Lastly, particular elements play crucial roles in the design of compositions and structures. The mentioned characteristics of structures are ultimately attributed to the nature of certain compositions and the interaction of compositions arranged according to general crystal structures and symmetry. Except for general disorder introduced via elemental diversities, small differences in compositions and structures (varies from as small as an atom or cation to clusters containing several atoms or cations) and interactions of multiple sites with vastly different structures can also behave as crucial contributors to exhibit exceptionally high performance different from other oxides. For example, Co is proven to play a significant role in achieving high capacity and good cycling stability in LIBs. Similarly, enhancing the covalency of specific metal–oxygen bonds (e.g. Co-O bond) [73], by introducing elements with less electronegativity is beneficial for OER catalysis. Another more general example is that the compositional diversity and abundant oxygen vacancies introduced into the system can lead to variable valence states, which open opportunities for creating complex three-dimensional lithium-ion transport channels. Additionally, HEOs demonstrated high stability in electrochemical processes, such as de-

lithiation process and OER, and are gaining attraction in applications such as thermal catalysis, electrocatalysis and photocatalysis as a host for reactive sites such as nano metallic particles or defects.

5. Summary and outlook

Research interest in HEOs has emerged endlessly in the past decade and HEOs have shown immense potential across various functionalities and applications, including thermoelectrics, dielectrics and energy storage, thermal barrier coatings, lithium batteries, catalysis, magnetics, and supercapacitors, etc. Generally, descriptions of these effects are based on the thermodynamics of HEOs formation and the structural disorder of HEOs introduced by configuration diversity, with the most common reference being the classical simple Eq. (1).

The high entropy effect plays a crucial role in modifying structures and tuning properties in all high-entropy systems and can be classified into four aspects: entropy stabilization, lattice distortion, sluggish diffusion, and cocktail effect. Charge compensation further widens the phase space of HEOs to a huge number of possible compositions. Dislocations, oxygen vacancies and other defects may naturally exist due to the introduction of metallic species with varying preferred or mixed valence states, constituting the structural root of diversified properties. At the charge level, oxygen polyhedron distortion and oxygen vacancy affect local metal–oxygen bonding and charge localization status, depending on the specific valence electron shells of the species involved. At the orbital and band level, the hybridization of *d-p* or *f-p* orbitals determines the band structures of HEOs, such as high bandwidth. The ability of certain metallic species to adopt mixed valence states enables reversible band structures.

Numerous applied synthesis methods have been applied and developed for fast, efficient and high-quality preparation of HEOs. For certain fields of applications, there are already a series of nominated methods that have been practiced, depending on different targeted forms or structure needed. On the basis of solid-state reactions method, advanced methods with the assistance of plasma and flash have been developed to realize a fast production of dense bulks with a controllable grain size and distribution. While for crystalline thin film, either PLD or magnetron sputtering is capable of realizing the epitaxial growth. Spin coating of a precursor solution followed by thermal treatment can also produce thin films but rather textured ones. For nanoparticles in applications such as electrochemistry, sol–gel method, (reverse) co-precipitation and hydrothermal method, etc. are preferred. As for characterizations in experiments and computations, lattice distortion can be confirmed through a series of experimental characterization methods such as XRD, Raman and X-band EPR spectroscopy. For further probing at the polyhedron level, geometric analysis considering elemental occupying preference and unique characteristics at the short range can be based on high-resolution HAADF-STEM images, EXAFS and XMCD.

While studies of complex HEOs have shown enlightening for several potential applications for property enhancement, numerous unresolved issues of a very fundamental nature related to structure–property relations demand further investigations. Primarily, the structure–property correlations discussed to date remain largely qualitative and typically apply to specific material systems. Semi-qualitative and ultimately quantitative descriptions of certain structural parameters, such as valence bonding, are needed to correlate certain properties and identify optimal HEO candidates for specific application fields. The potential fundamental relationship between configuration entropy and the underlying mechanism of a series of properties (such as thermoelectric, dielectric, energy storage, and catalysis) is still not well understood or established. Furthermore, to what extent can the degree of disorder be controlled and the property be tuned flexibly still remains unclear. Existing research results suggest that a homogeneously random distribution of introduced compositions can be achieved through suitable composition design. However, the realization and influence of topological order in the short-to-mid range on a series of structure-property behaviors still require further studies. Secondary effects such as octahedral tilting and atom displacements caused by introducing elemental diversity at certain sub-lattice sites have not been systematically studied, but could provide valuable insights into the influence of high entropy effect on specific systems.

Therefore, to understand the role of entropy deeply and comprehensively in HEOs, more efforts should be devoted to the mechanism study, including visualizing the short-range and long-range structure, exploring the interaction between multiple components, and discovering more descriptors of both structures and properties rather than only focusing on the synthesis of novel high-entropy material systems. To be more specific, challenges and opportunities for developing and understanding HEOs can be summarized as follows:

(1) The current understanding of the high entropy effect largely focuses on configuration entropy, with other potential contributors demanding further study. More descriptors should be discovered and considered as crucial parameters for interpreting the high entropy effect on the structure formation, physiochemical properties, and applications for HEOs.

(2) Established criteria for the synthesis of HEOs are still empirical and qualitative, calling for further thermodynamic guidance. A library is needed to be built, which should contain the synthetic methods and the physical and chemical parameters of the systems with multiple elements.

(3) Advanced characterization techniques including diffraction, spectroscopy, and microscopy would be of great importance to further improve our understanding of the short range and long-range structures in HEOs. Nevertheless, characterizations of HEO structures in the shor -range, especially for the oxygen polyhedron distortion and bond length distribution, are still relatively time-consuming. Moreover, insights of disorder across different ranges mainly focus on long-range homogeneity of element distribution at certain sub-lattice sites and short-range clustering behaviors of certain elements. The degree of disorder, which typically covers a few hundred atoms, is not well understood yet. While clustering of certain elements has been identified via EXAFS at the nearest neighboring shell, and increased doping elements seem to reduce short-range order while preserving long-range order, the mid-range behavior (potentially acting as a transition from short-range to long-range) needs additional characterizations and simulations.

(4) The computational complexity involved in thermodynamic studies of HEOs leads to challenges in understanding the solubility

of each metallic element, energy fluctuation in different phase statuses and atomic ranges, as well as the associated chemical potential of component mixing, among others. Big data or artificial intelligence assisted computation methods should be applied in more systems to accelerate the identification and mapping of the structures and properties for various HEOs systems.

CRediT authorship contribution statement

Chang Liu: Conceptualization, Investigation, Methodology, Supervision, Validation, Visualization, Writing – original draft, Writing – review & editing. **Shun Li:** Funding acquisition, Methodology, Supervision, Writing – original draft, Writing – review & editing, Investigation. **Yunpeng Zheng:** Investigation, Supervision, Writing – original draft, Writing – review & editing. **Min Xu:** Investigation, Visualization, Writing – original draft, Writing – review & editing. **Hongyang Su:** Methodology, Writing – review & editing. **Xiang Miao:** Investigation, Writing – original draft, Writing – review & editing. **Yiqian Liu:** Investigation, Writing – original draft. **Zhifang Zhou:** Funding acquisition, Investigation, Writing – original draft, Writing – review & editing. **Junlei Qi:** Investigation, Writing – original draft, Funding acquisition. **Bingbing Yang:** Funding acquisition, Investigation, Writing – original draft. **Di Chen:** Funding acquisition, Investigation, Supervision, Validation, Writing – review & editing. **Ce-Wen Nan:** Conceptualization, Funding acquisition, Supervision. **Yuan-Hua Lin:** Conceptualization, Funding acquisition, Investigation, Methodology, Project administration, Supervision, Validation, Writing – review & editing.

Declaration of competing interest

The authors declare that they have no known competing financial interests or personal relationships that could have appeared to influence the work reported in this paper.

Data availability

Data will be made available on request.

Acknowledgement

This work was supported by the National Key Research and Development Program of China [grant number 2021YFB3800601], the Basic Science Center Project of the National Natural Science Foundation of China [grant number 52388201], the State Key Laboratory of New Ceramic and Fine Processing Tsinghua University [grant number KF202101], the National Natural Science Foundation of China [grant number 22075126, 52102137, 523B2021, 12474095 and 52402323], the Guangdong Basic and Applied Basic Research Foundation [grant number 2022A1515110048, B.Y.], and the China Postdoctoral Science Foundation [grant number 2024T170479 and 2022M710073].

References

[1] Yeh J-W, Chen S-K, Lin S-J, Gan J-Y, Chin T-S, Shun T-T, et al. Nanostructured high-entropy alloys with multiple principal elements: novel alloy design concepts and outcomes. Adv Eng Mater 2004;6:299–303.
[2] Oses C, Toher C, Curtarolo S. High-entropy ceramics. Nat Rev Mater 2020;5:295–309.
[3] Rost CM, Sachet E, Borman T, Moballegh A, Dickey EC, Hou D, et al. Entropy-stabilized oxides. Nat Commun 2015;6:8485.
[4] Jana SS, Maiti T. Designing rare earth-free high entropy oxides with a tungsten bronze structure for thermoelectric applications. Mater Horiz 2023;10:1848–55.
[5] Vinnik DA, Trofimov EA, Zhivulin VE, Zaitseva OV, Gudkova SA, Starikov AY, et al. High-entropy oxide phases with magnetoplumbite structure. Ceram Int 2019;45:12942–8.
[6] Wang K, Nishio K, Horiba K, Kitamura M, Edamura K, Imazeki D, et al. Synthesis of high-entropy layered oxide epitaxial thin films: LiCr1/6Mn1/6Fe1/6Co1/6Ni1/6Cu1/6O2. Cryst Growth Des 2022;22:1116–22.
[7] Zhang W, Mazza AR, Skoropata E, Mukherjee D, Musico B, Zhang J, et al. Applying configurational complexity to the 2D Ruddlesden-popper crystal structure. ACS Nano 2020;14:13030–7.
[8] Sharma Y, Musico BL, Gao X, Hua C, May AF, Herklotz A, et al. Single-crystal high entropy perovskite oxide epitaxial films. Phys Rev Mater 2018;2:060404.
[9] Gu K, Wang D, Xie C, Wang T, Huang G, Liu Y, et al. Defect-rich high-entropy oxide nanosheets for efficient 5-hydroxymethylfurfural electrooxidation. Angew Chem Int Ed 2021;60:20253–8.
[10] Nguyen TX, Patra J, Chang J-K, Ting J-M. High entropy spinel oxide nanoparticles for superior lithiation–delithiation performance. J Mater Chem A 2020;8:18963–73.
[11] Gu Y, Bao A, Wang X, Chen Y, Dong L, Liu X, et al. Engineering the oxygen vacancies of rocksalt-type high-entropy oxides for enhanced electrocatalysis. Nanoscale 2022;14:515–24.
[12] Lun Z, Ouyang B, Kwon D-H, Ha Y, Foley EE, Huang T-Y, et al. Cation-disordered rocksalt-type high-entropy cathodes for Li-ion batteries. Nat Mater 2021;20:214–21.
[13] Zhao J, Bao J, Yang S, Niu Q, Xie R, Zhang Q, et al. Exsolution-dissolution of supported metals on high-entropy Co_3MnNiCuZnOx: toward sintering-resistant catalysis. ACS Catal 2021;11:12247–57.
[14] Hou S, Ma X, Shu Y, Bao J, Zhang Q, Chen M, et al. Self-regeneration of supported transition metals by a high entropy-driven principle. Nat Commun 2021;12:5917.
[15] Zhang P, Lou Z, Hu G, Wu Z, Xu J, Gong L, et al. In-situ construction of all-scale hierarchical microstructure and thermoelectric properties of (Sr0.25Ca0.25Ba0.25La0.25)TiO3/Pb@Bi composite oxide ceramics. J Materiomics 2023.
[16] Toher C, Oses C, Esters M, Hicks D, Kotsonis GN, Rost CM, et al. High-entropy ceramics: propelling applications through disorder. MRS Bull 2022;47:194–202.
[17] Xiang H, Xing Y, Dai F-z, Wang H, Su L, Miao L, et al. High-entropy ceramics: present status, challenges, and a look forward. J Adv Ceram 2021;10:385–441.
[18] Sun Y, Dai S. High-entropy materials for catalysis: a new frontier. Sci Adv 2021;7:eabg1600.
[19] Zhang R-Z, Reece MJ. Review of high entropy ceramics: design, synthesis, structure and properties. J Mater Chem A 2019;7:22148–62.

[20] Wang Q, Velasco L, Breitung B, Presser V. High-entropy energy materials in the age of big data: a critical guide to next-generation synthesis and applications. Adv Energy Mater 2021;11:2102355.
[21] Aamlid SS, Oudah M, Rottler J, Hallas AM. Understanding the role of entropy in high entropy oxides. J Am Chem Soc 2023.
[22] Qi H, Chen L, Deng S, Chen J. High-entropy ferroelectric materials. Nat Rev Mater 2023;8:355–6.
[23] Sarkar A, Wang Q, Schiele A, Chellali MR, Bhattacharya SS, Wang D, et al. High-entropy oxides: fundamental aspects and electrochemical properties. Adv Mater 2019;31:1806236.
[24] Albedwawi SH, AlJaberi A, Haidemenopoulos GN, Polychronopoulou K. High entropy oxides-exploring a paradigm of promising catalysts: a review. Mater Des 2021;202:109534.
[25] Liu Z-Y, Liu Y, Xu Y, Zhang H, Shao Z, Wang Z, et al. Novel high-entropy oxides for energy storage and conversion: from fundamentals to practical applications. Green Energy Environ 2023;8:1341–57.
[26] Zhang Q, You J, Zhang X, Yi B, Zhao Y, Li Y, et al. Research progress of high-entropy oxides as oxygen evolution reaction catalysts. Energy Fuel 2024;38:6659–78.
[27] Sarkar A, Kruk R, Hahn H. Magnetic properties of high entropy oxides. Dalton Trans 2021;50:1973–82.
[28] Zhong Y, Sabarou H, Yan X, Yang M, Gao MC, Liu X, et al. Exploration of high entropy ceramics (HECs) with computational thermodynamics - a case study with LaMnO3±δ. Mater Des 2019;182:108060.
[29] Zheng Y, Zou M, Zhang W, Yi D, Lan J, Nan C-W, et al. Electrical and thermal transport behaviours of high-entropy perovskite thermoelectric oxides. J Adv Ceram 2021;10:377–84.
[30] Brahlek M, Gazda M, Keppens V, Mazza AR, McCormack SJ, Mielewczyk-Gryń A, et al. What is in a name: Defining "high entropy" oxides. APL Mater 2022;10.
[31] Otto F, Yang Y, Bei H, George EP. Relative effects of enthalpy and entropy on the phase stability of equiatomic high-entropy alloys. Acta Mater 2013;61:2628–38.
[32] Hume-Rothery W, Haworth CW, Smallman RE. The structure of metals and alloys [by]. [5th ed.] ed. London: Institute of Metals and the Institution of Metallurgists; 1969.
[33] Lin L, Wang K, Azmi R, Wang J, Sarkar A, Botros M, et al. Mechanochemical synthesis: route to novel rock-salt-structured high-entropy oxides and oxyfluorides. J Mater Sci 2020;55:16879–89.
[34] Yang B, Liu Y, Gong C, Lan S, Zhou Z, Zhu X, et al. Design of high-entropy relaxor ferroelectrics for comprehensive energy storage enhancement. Adv Funct Mater. n/a: 2409344.
[35] Wright AJ, Wang Q, Huang C, Nieto A, Chen R, Luo J. From high-entropy ceramics to compositionally-complex ceramics: a case study of fluorite oxides. J Eur Ceram Soc 2020;40:2120–9.
[36] Lökçü E, Anik M. Investigating the structural and lithium storage properties of high-entropy oxides in the Mg-Co-Ni-Cu-Zn-O system. Scr Mater 2024;240:115840.
[37] Han Y, Liu X, Zhang Q, Huang M, Li Y, Pan W, et al. Ultra-dense dislocations stabilized in high entropy oxide ceramics. Nat Commun 2022;13:2871.
[38] Friedrich F, Pieper S, Gasteiger HA. Entropy measurements of Li-Ion battery cells with Li- and Mn-Rich layered transition metal oxides via linear temperature variation. J Electrochem Soc 2021;168:120502.
[39] Sarkar A, Eggert B, Witte R, Lill J, Velasco L, Wang Q, et al. Comprehensive investigation of crystallographic, spin-electronic and magnetic structure of $(Co_{0.2}Cr_{0.2}Fe_{0.2}Mn_{0.2}Ni_{0.2})_3O_4$: unraveling the suppression of configuration entropy in high entropy oxides. Acta Mater 2022;226:117581.
[40] Acharya S, Hwang J, Kim K, Kim J, Hwang W, Soon A, et al. Quasi-random distribution of distorted nanostructures enhances thermoelectric performance of high-entropy chalcopyrite. Nano Energy 2023;112:108493.
[41] van de Walle A, Ceder G. The effect of lattice vibrations on substitutional alloy thermodynamics. Rev Mod Phys 2002;74:11–45.
[42] Wang Y, Li X, Luo J, Woodfield BF, Wang X, Feng T, et al. An unexpected decrease in vibrational entropy of multicomponent rutile oxides. J Am Chem Soc 2024;146:14493–504.
[43] Pitike KC, Kc S, Eisenbach M, Bridges CA, Cooper VR. Predicting the phase stability of multicomponent high-entropy compounds. Chem Mater 2020;32:7507–15.
[44] Sarker P, Harrington T, Toher C, Oses C, Samiee M, Maria J-P, et al. High-entropy high-hardness metal carbides discovered by entropy descriptors. Nat Commun 2018;9:4980.
[45] Liu R, Chen H, Zhao K, Qin Y, Jiang B, Zhang T, et al. Entropy as a gene-like performance indicator promoting thermoelectric materials. Adv Mater 2017;29:1702712.
[46] Zhang C, Yang Y. The CALPHAD approach for HEAs: challenges and opportunities. MRS Bull 2022;47:158–67.
[47] McCormack SJ, Navrotsky A. Thermodynamics of high entropy oxides. Acta Mater 2021;202:1–21.
[48] Hack K, Wu G, Yazhenskikh E, Jantzen T, Müller M. A CALPHAD approach to modelling of slag viscosities. Calphad 2019;65:101–10.
[49] Hossain MD, Borman T, Oses C, Esters M, Toher C, Feng L, et al. Entropy landscaping of high-entropy carbides. Adv Mater 2021;33:2102904.
[50] Divilov S, Eckert H, Hicks D, Oses C, Toher C, Friedrich R, et al. Disordered enthalpy–entropy descriptor for high-entropy ceramics discovery. Nature 2024;625:66–73.
[51] Dey D, Liang L, Yu L. Mixed enthalpy-entropy descriptor for the rational design of synthesizable high-entropy materials over vast chemical spaces. J Am Chem Soc 2024;146:5142–51.
[52] Wright AJ, Wang Q, Ko S-T, Chung KM, Chen R, Luo J. Size disorder as a descriptor for predicting reduced thermal conductivity in medium- and high-entropy pyrochlore oxides. Scr Mater 2020;181:76–81.
[53] Spiridigliozzi L, Ferone C, Cioffi R, Dell'Agli G. A simple and effective predictor to design novel fluorite-structured High Entropy Oxides (HEOs). Acta Mater 2021;202:181–9.
[54] Liu J, Wang A, Gao P, Bai R, Liu J, Du B, et al. Machine learning-based crystal structure prediction for high-entropy oxide ceramics. J Am Ceram Soc 2024;107:1361–71.
[55] Jiang S, Hu T, Gild J, Zhou N, Nie J, Qin M, et al. A new class of high-entropy perovskite oxides. Scr Mater 2018;142:116–20.
[56] Su L, Huyan H, Sarkar A, Gao W, Yan X, Addiego C, et al. Direct observation of elemental fluctuation and oxygen octahedral distortion-dependent charge distribution in high entropy oxides. Nat Commun 2022;13:2358.
[57] Mouta R, Silva RX, Paschoal CW. Tolerance factor for pyrochlores and related structures. Acta Crystallogr B Struct Sci Cryst Eng Mater 2013;69:439–45.
[58] Teng Z, Zhu L, Tan Y, Zeng S, Xia Y, Wang Y, et al. Synthesis and structures of high-entropy pyrochlore oxides. J Eur Ceram Soc 2020;40:1639–43.
[59] Akrami S, Edalati P, Fuji M, Edalati K. High-entropy ceramics: review of principles, production and applications. Mater Sci Eng R Rep 2021;146:100644.
[60] Fracchia M, Coduri M, Manzoli M, Ghigna P, Tamburini UA. Is configurational entropy the main stabilizing term in rock-salt $Mg_{0.2}Co_{0.2}Ni_{0.2}Cu_{0.2}Zn_{0.2}O$ high entropy oxide? Nat Commun 2022;13:2977.
[61] Koshibae W, Tsutsui K, Maekawa S. Thermopower in cobalt oxides. Phys Rev B 2000;62:6869–72.
[62] Sauerwein RA, de Oliveira MJ. Entropy of spin models by the Monte Carlo method. Phys Rev B 1995;52:3060–2.
[63] Mazza AR, Skoropata E, Sharma Y, Lapano J, Heitmann TW, Musico BL, et al. Designing magnetism in high entropy oxides. Adv Sci 2022;9:2200391.
[64] Berlijn T, Alvarez G, Parker DS, Hermann RP, Fishman RS. Simulating spin waves in entropy stabilized oxides. Phys Rev Res 2021;3:033273.
[65] Smith HL, Li CW, Hoff A, Garrett GR, Kim DS, Yang FC, et al. Separating the configurational and vibrational entropy contributions in metallic glasses. Nat Phys 2017;13:900–5.
[66] Esters M, Oses C, Hicks D, Mehl MJ, Jahnátek M, Hossain MD, et al. Settling the matter of the role of vibrations in the stability of high-entropy carbides. Nat Commun 2021;12:5747.
[67] Chellali MR, Sarkar A, Nandam SH, Bhattacharya SS, Breitung B, Hahn H, et al. On the homogeneity of high entropy oxides: an investigation at the atomic scale. Scr Mater 2019;166:58–63.
[68] Dupuy AD, Chellali MR, Hahn H, Schoenung JM. Multiscale phase homogeneity in bulk nanocrystalline high entropy oxides. J Eur Ceram Soc 2021;41:4850–8.

[69] Yao Y, Yang F, Zhao X. Multicomponent high-entropy Zr-Y-Yb-Ta-Nb-O oxides for next-generation thermal barrier coating applications. J Am Ceram Soc 2022; 105:35–43.
[70] Wang X, Cortez J, Dupuy AD, Schoenung JM, Bowman WJ. High entropy oxide (Co, Cu, Mg, Ni, Zn)O exhibits grain size dependent room temperature deformation. Mater Res Lett 2023;11:196–204.
[71] Johnstone GHJ, González-Rivas MU, Taddei KM, Sutarto R, Sawatzky GA, Green RJ, et al. Entropy engineering and tunable magnetic order in the spinel high-entropy oxide. J Am Chem Soc 2022;144:20590–600.
[72] Liu Y, Yang J, Deng S, Zhang Y, Zhang Y, Sun S, et al. Flexible polarization configuration in high-entropy piezoelectrics with high performance. Acta Mater 2022;236:118115.
[73] Liu F, Yu M, Chen X, Li J, Liu H, Cheng F. Defective high-entropy rocksalt oxide with enhanced metal-oxygen covalency for electrocatalytic oxygen evolution. Chin J Catal 2022;43:122–9.
[74] Chen J, Liu W, Liu J, Zhang X, Yuan M, Zhao Y, et al. Stability and compressibility of cation-doped high-entropy oxide $MgCoNiCuZnO_5$. J Phys Chem C 2019; 123:17735–44.
[75] Tsai KY, Tsai MH, Yeh JW. Sluggish diffusion in Co–Cr–Fe–Mn–Ni high-entropy alloys. Acta Mater 2013;61:4887–97.
[76] Teng Z, Tan Y, Zhang H. High-entropy pyrochlore A(2)B(2)O(7) with both heavy and light rare-earth elements at the a site. Materials (Basel) 2021;15.
[77] Aamlid SS, Oudah M, Rottler J, Hallas AM. Understanding the role of entropy in high entropy oxides. J Am Chem Soc 2023;145:5991–6006.
[78] Zhou L, Li F, Liu J-X, Hu Q, Bao W, Wu Y, et al. High-entropy thermal barrier coating of rare-earth zirconate: a case study on (La0.2Nd0.2Sm0.2Eu0.2Gd0.2) 2Zr2O7 prepared by atmospheric plasma spraying. J Eur Ceram Soc 2020;40:5731–9.
[79] Zhao Z, Xiang H, Dai F-Z, Peng Z, Zhou Y. $(La_{0.2}Ce_{0.2}Nd_{0.2}Sm_{0.2}Eu_{0.2})_2Zr_2O_7$: a novel high-entropy ceramic with low thermal conductivity and sluggish grain growth rate. J Mater Sci Technol 2019;35:2647–51.
[80] Su L, Chen X, Xu L, Eldred T, Smith J, DellaRova C, et al. Visualizing the formation of high-entropy fluorite oxides from an amorphous precursor at atomic resolution. ACS Nano 2022;16:21397–406.
[81] Zhou L, Liu J-X, Tu T-Z, Wu Y, Zhang G-J. Fast grain growth phenomenon in high-entropy ceramics: a case study in rare-earth hexaaluminates. J Adv Ceram 2023;12:111–21.
[82] Grzesik Z, Smola G, Stygar M, Dabrowa J, Zajusz M, Mroczka K, et al. Defect structure and transport properties in (Co, Cu, Mg, Ni, Zn)O high entropy oxide. J Eur Ceram Soc 2019;39:4292–8.
[83] Lou Z, Zhang P, Zhu J, Gong L, Xu J, Chen Q, et al. A novel high-entropy perovskite ceramics $Sr_{0.9}La_{0.1}(Zr_{0.25}Sn_{0.25}Ti_{0.25}Hf_{0.25})O_3$ with low thermal conductivity and high Seebeck coefficient. J Eur Ceram Soc 2022;42:3480–8.
[84] Djenadic R, Sarkar A, Clemens O, Loho C, Botros M, Chakravadhanula VSK, et al. Multicomponent equiatomic rare earth oxides. Mater Res Lett 2017;5:102–9.
[85] Ye YF, Wang Q, Lu J, Liu CT, Yang Y. High-entropy alloy: challenges and prospects. Mater Today 2016;19:349–62.
[86] Dragoe N. Entropy driven synthesis of new materials. Materials Lab 2002.
[87] Zhang R, Wang C, Zou P, Lin R, Ma L, Yin L, et al. Compositionally complex doping for zero-strain zero-cobalt layered cathodes. Nature 2022;610:67–73.
[88] Kim SJ, Yoon KN, Ko W-S, Park ES. Entropy-stabilized silicides: expanding the B20 single-phase region from mono-silicide to high-entropy silicide. APL Mater 2022;10.
[89] Song H, Tian F, Hu Q-M, Vitos L, Wang Y, Shen J, et al. Local lattice distortion in high-entropy alloys. Phys Rev Mater 2017;1:023404.
[90] Lee C, Song G, Gao MC, Feng R, Chen P, Brechtl J, et al. Lattice distortion in a strong and ductile refractory high-entropy alloy. Acta Mater 2018;160:158–72.
[91] Dąbrowa J, Danielewski M. State-of-the-art diffusion studies in the high entropy alloys. Metals 2020;10:347.
[92] Chroneos A. Oxygen self-diffusion in fluorite high entropy oxides. Appl Sci 2024;14:5309.
[93] Grzesik Z, Smoła G, Stygar M, Dąbrowa J, Zajusz M, Mroczka K, et al. Defect structure and transport properties in (Co, Cu, Mg, Ni, Zn)O high entropy oxide. J Eur Ceram Soc 2019;39:4292–8.
[94] Rost CM, Rak Z, Brenner DW, Maria J-P. Local structure of the MgxNixCoxCuxZnxO(x=0.2) entropy-stabilized oxide: an EXAFS study. J Am Ceram Soc 2017; 100:2732–8.
[95] Anand G, Wynn AP, Handley CM, Freeman CL. Phase stability and distortion in high-entropy oxides. Acta Mater 2018;146:119–25.
[96] Dupuy AD, Chiu IT, Shafer P, Arenholz E, Takamura Y, Schoenung JM. Hidden transformations in entropy-stabilized oxides. J Eur Ceram Soc 2021;41:6660–9.
[97] Yu Y, Liu S, Ren Y, Xia Z, Zhang S, Wang N, et al. Composition-constrained rocksalt structure high entropy oxides with non-equimolar cations: design and synthesis based on cluster-plus-glue-atom model. Ceram Int 2022;48:25647–50.
[98] Sahinovic A, Geisler B. Quantifying transfer learning synergies in infinite-layer and perovskite nitrides, oxides, and fluorides. J Phys Condens Matter 2022;34: 214003.
[99] Leong Z, Desai P, Morley N. Can empirical biplots predict high entropy oxide phases? J Compos Sci 2021;5:311.
[100] Nguyen TX, Liao Y-C, Lin C-C, Su Y-H, Ting J-M. Advanced high entropy perovskite oxide electrocatalyst for oxygen evolution reaction. Adv Funct Mater 2021; 31:2101632.
[101] Yan J, Wang D, Zhang X, Li J, Du Q, Liu X, et al. A high-entropy perovskite titanate lithium-ion battery anode. J Mater Sci 2020;55:6942–51.
[102] Dąbrowa J, Olszewska A, Falkenstein A, Schwab C, Szymczak M, Zajusz M, Moździerz M, Mikuła A, Zielińska K, Berent K, Czeppe T. An innovative approach to design SOFC air electrode materials: high entropy La 1− x Sr x (Co, Cr, Fe, Mn, Ni) O 3− δ (x= 0, 0.1, 0.2, 0.3) perovskites synthesized by the sol–gel method. J Mater Chem A 2020;8(46):24455–68.
[103] Yashima M, Tsujiguchi T, Sakuda Y, Yasui Y, Zhou Y, Fujii K, et al. High oxide-ion conductivity through the interstitial oxygen site in Ba7Nb4MoO20-based hexagonal perovskite related oxides. Nat Commun 2021;12:556.
[104] Xia C, Mi Y, Wang B, Lin B, Chen G, Zhu B. Shaping triple-conducting semiconductor BaCo0.4Fe0.4Zr0.1Y0.1O3-δ into an electrolyte for low-temperature solid oxide fuel cells. Nature. Communications 2019;10:1707.
[105] Park J, Xu B, Pan J, Zhang D, Lany S, Liu X, et al. Accurate prediction of oxygen vacancy concentration with disordered A-site cations in high-entropy perovskite oxides. npj Comput Mater 2023;9:29.
[106] Chen Y, Qi J, Zhang M, Luo Z, Lin Y-H. Pyrochlore-based high-entropy ceramics for capacitive energy storage. J Adv Ceram 2022;11:1179–85.
[107] Vayer F, Decorse C, Bérardan D, Dragoe N. New entropy-stabilized oxide with pyrochlore structure: Dy2(Ti0.2Zr0.2Hf0.2Ge0.2Sn0.2)2O7. J Alloy Compd 2021;883:160773.
[108] Jiang B, Bridges CA, Unocic RR, Pitike KC, Cooper VR, Zhang Y, et al. Probing the local site disorder and distortion in pyrochlore high-entropy oxides. J Am Chem Soc 2021;143:4193–204.
[109] Pitike KC, Macias A, Eisenbach M, Bridges CA, Cooper VR. Computationally accelerated discovery of high entropy pyrochlore oxides. Chem Mater 2022;34: 1459–72.
[110] Wright AJ, Wang Q, Hu C, Yeh Y-T, Chen R, Luo J. Single-phase duodenary high-entropy fluorite/pyrochlore oxides with an order-disorder transition. Acta Mater 2021;211:116858.
[111] Tan L, Su X, Yang J, Ji P, Sun F, Tian Q, et al. Facile synthesis of high-entropy zirconate nanopowders and their sintering behaviors. J Adv Ceram 2023;12: 498–509.
[112] Jia H, Li C, Chen G, Li H, Li S, An L, et al. Design and synthesis of high-entropy pyrochlore ceramics based on valence combination. J Eur Ceram Soc 2022;42: 5973–83.
[113] Kocevski V, Pilania G, Uberuaga BP. Modeling disorder in pyrochlores and other anion-deficient fluorite structural derivative oxides. Front Chem 2021;9.
[114] Talanov MV, Talanov VM. Structural diversity of ordered pyrochlores. Chem Mater 2021;33:2706–25.
[115] Sarkar A, Eggert B, Velasco L, Mu X, Lill J, Ollefs K, et al. Role of intermediate 4f states in tuning the band structure of high entropy oxides. APL Mater 2020;8.
[116] Chang TC, Lu YT, Lee CH, Gupta JK, Hardwick LJ, Hu CC, et al. The effect of degrees of inversion on the electronic structure of spinel $NiCo_2O_4$: a density functional theory study. ACS Omega 2021;6:9692–9.

[117] Andreozzi GB, Princivalle F, Skogby H, Giusta AD. Cation ordering and structural variations with temperature in $MgAl_2O_4$ spinel: an X-ray single-crystal study. Am Mineral 2000;85:1164–71.
[118] Triolo C, Moulaee K, Ponti A, Pagot G, Di Noto V, Pinna N, et al. Spinel-structured high-entropy oxide nanofibers as electrocatalysts for oxygen evolution in alkaline solution: effect of metal combination and calcination temperature. Adv Funct Mater 2024;34:2306375.
[119] Nam K-H, Wang Z, Luo J, Huang C, Millares MF, Pace A, et al. High-entropy spinel oxide ferrites for battery applications. Chem Mater 2024;36:4481–94.
[120] Baek J, Hossain MD, Mukherjee P, Lee J, Winther KT, Leem J, et al. Synergistic effects of mixing and strain in high entropy spinel oxides for oxygen evolution reaction. Nat Commun 2023;14:5936.
[121] Usharani NJ, Sanghavi H, Bhattacharya SS. Factors influencing phase formation and band gap studies of a novel multicomponent high entropy (Co, Cu, Mg, Ni, Zn)$_2TiO_4$ orthotitanate spinel. J Alloy Compd 2021;888:161390.
[122] Biesuz M, Spiridigliozzi L, Dell'Agli G, Bortolotti M, Sglavo VM. Synthesis and sintering of (Mg Co, Ni, Cu, Zn)O entropy-stabilized oxides obtained by wet chemical methods. J Mater Sci 2018;53:8074–85.
[123] Sarkar A, Velasco L, Wang D, Wang Q, Talasila G, de Biasi L, et al. High entropy oxides for reversible energy storage. Nat Commun 2018;9:3400.
[124] Jacobson V, Diercks D, To B, Zakutayev A, Brennecka G. Thin film growth effects on electrical conductivity in entropy stabilized oxides. J Eur Ceram Soc 2021; 41:2617–24.
[125] Guo H, Wang X, Dupuy AD, Schoenung JM, Bowman WJ. Growth of nanoporous high-entropy oxide thin films by pulsed laser deposition. J Mater Res 2022;37: 124–35.
[126] Chen K, Pei X, Tang L, Cheng H, Li Z, Li C, et al. A five-component entropy-stabilized fluorite oxide. J Eur Ceram Soc 2018;38:4161–4.
[127] Zhang F, Cheng F, Cheng C, Guo M, Liu Y, Miao Y, et al. Preparation and electrical conductivity of (Zr, Hf, Pr, Y, La) O high entropy fluorite oxides. J Mater Sci Technol 2022;105:122–30.
[128] Gild J, Samiee M, Braun JL, Harrington T, Vega H, Hopkins PE, et al. High-entropy fluorite oxides. J Eur Ceram Soc 2018;38:3578–84.
[129] Kirnbauer A, Spadt C, Koller CM, Kolozsvári S, Mayrhofer PH. High-entropy oxide thin films based on Al–Cr–Nb–Ta–Ti. Vacuum 2019;168:108850.
[130] Liu J, Ren K, Ma C, Du H, Wang Y. Dielectric and energy storage properties of flash-sintered high-entropy $(Bi_{0.2}Na_{0.2}K_{0.2}Ba_{0.2}Ca_{0.2})TiO_3$ ceramic. Ceram Int 2020;46:20576–81.
[131] Banerjee R, Chatterjee S, Ranjan M, Bhattacharya T, Mukherjee S, Jana SS, et al. High-entropy perovskites: an emergent class of oxide thermoelectrics with ultralow thermal conductivity. ACS Sustain Chem Eng 2020;8:17022–32.
[132] Yang W, Zheng G. High energy storage density and efficiency in nanostructured $(Bi_{0.2}Na_{0.2}K_{0.2}La_{0.2}Sr_{0.2})TiO_3$ high-entropy ceramics. J Am Ceram Soc 2022; 105:1083–94.
[133] Schweidler S, Tang Y, Lin L, Karkera G, Alsawaf A, Bernadet L, et al. Synthesis of perovskite-type high-entropy oxides as potential candidates for oxygen evolution. Front Energy Res 2022;10.
[134] Krawczyk PA, Jurczyszyn M, Pawlak J, Salamon W, Baran P, Kmita A, et al. High-entropy perovskites as multifunctional metal oxide semiconductors: synthesis and characterization of $(Gd_{0.2}Nd_{0.2}La_{0.2}Sm_{0.2}Y_{0.2})$CoO3. ACS Appl Electron Mater 2020;2:3211–20.
[135] Patel RK, Ojha SK, Kumar S, Saha A, Mandal P, Freeland JW, et al. Epitaxial stabilization of ultra thin films of high entropy perovskite. Appl Phys Lett 2020; 116.
[136] Sun Z, Zhao Y, Sun C, Ni Q, Wang C, Jin H. High entropy spinel-structure oxide for electrochemical application. Chem Eng J 2022;431:133448.
[137] Fereja SL, Zhang Z, Fang Z, Guo J, Zhang X, Liu K, et al. High-entropy oxide derived from metal-organic framework as a bifunctional electrocatalyst for efficient urea oxidation and oxygen evolution reactions. ACS Appl Mater Interfaces 2022;14:38727–38.
[138] Chen H, Qiu N, Wu B, Yang Z, Sun S, Wang Y. A new spinel high-entropy oxide $(Mg_{0.2}Ti_{0.2}Zn_{0.2}Cu_{0.2}Fe_{0.2})_3O_4$ with fast reaction kinetics and excellent stability as an anode material for lithium ion batteries. RSC Adv 2020;10:9736–44.
[139] Parida T, Karati A, Guruvidyathri K, Murty BS, Markandeyulu G. Novel rare-earth and transition metal-based entropy stabilized oxides with spinel structure. Scr Mater 2020;178:513–7.
[140] Mao A, Xiang H-Z, Zhang Z-G, Kuramoto K, Zhang H, Jia Y. A new class of spinel high-entropy oxides with controllable magnetic properties. J Magn Magn Mater 2020;497:165884.
[141] Matović B, Zagorac D, Cvijović-Alagić I, Zagorac J, Butulija S, Erčić J, et al. Fabrication and characterization of high entropy pyrochlore ceramics. Bol SECV 2023;62:66–76.
[142] Yang K, Bryce K, Zhu W, Zhao D, Lian J. Multicomponent pyrochlore solid solutions with uranium incorporation – a new perspective of materials design for nuclear applications. J Eur Ceram Soc 2021;41:2870–82.
[143] Park T, Javadinejad HR, Kim Y-K, Chang HJ, Choi H, Woong C, et al. Effect of processing route on the crystal structure and physical properties of bixbyite high-entropy oxides. J Alloy Compd 2022;893:162108.
[144] Tseng K-P, Yang Q, McCormack SJ, Kriven WM. High-entropy, phase-constrained, lanthanide sesquioxide. J Am Ceram Soc 2020;103:569–76.
[145] Ding F, Zhao C, Xiao D, Rong X, Wang H, Li Y, et al. Using high-entropy configuration strategy to design na-ion layered oxide cathodes with superior electrochemical performance and thermal stability. J Am Chem Soc 2022;144:8286–95.
[146] Zhao C, Ding F, Lu Y, Chen L, Hu Y-S. High-entropy layered oxide cathodes for sodium-ion batteries. Angew Chem Int Ed 2020;59:264–9.
[147] Kirsch A BE, Lefeld N, Larsen R, Mathiesen JK, Skjærvø SL. High-entropy oxides in the mullite-type structure. ChemRxiv Cambridge: Cambridge Open Engage. 2022.
[148] Sarkar A, Djenadic R, Wang D, Hein C, Kautenburger R, Clemens O, et al. Rare earth and transition metal based entropy stabilised perovskite type oxides. J Eur Ceram Soc 2018;38:2318–27.
[149] Pianassola M, Loveday M, McMurray JW, Koschan M, Melcher CL, Zhuravleva M. Solid-state synthesis of multicomponent equiatomic rare-earth oxides. J Am Ceram Soc 2020;103:2908–18.
[150] Petrovičovà B, Xu W, Musolino MG, Pantò F, Patanè S, Pinna N, et al. High-entropy spinel oxides produced via sol-gel and electrospinning and their evaluation as anodes in Li-Ion batteries. Appl Sci 2022;12:5965.
[151] Teng Z, Tan Y, Zeng S, Meng Y, Chen C, Han X, et al. Preparation and phase evolution of high-entropy oxides $A_2B_2O_7$ with multiple elements at A and B sites. J Eur Ceram Soc 2021;41:3614–20.
[152] Biesuz M, Fu S, Dong J, Jiang A, Ke D, Xu Q, et al. High entropy $Sr((Zr_{0.94}Y_{0.06})_{0.2}Sn_{0.2}Ti_{0.2}Hf_{0.2}Mn_{0.2})O_3$–x perovskite synthesis by reactive spark plasma sintering. J Asian Ceram Soc 2019;7:127–32.
[153] Yan N, Zhu Y, Cai M, Li B, Xu B, Li Y, et al. Reactive flash sintering of high-entropy oxide (Mg, Co, Ni, Cu, Zn)(1-x)Li(x)O at room temperature. Mater (Basel) 2022:15.
[154] Mao H-R, Guo R-F, Cao Y, Jin S-B, Qiu X-M, Shen P. Ultrafast densification of high-entropy oxide $(La_{0.2}Nd_{0.2}Sm_{0.2}Eu_{0.2}Gd_{0.2})_2Zr_2O_7$ by reactive flash sintering. J Eur Ceram Soc 2021;41:2855–60.
[155] Wang K, Ma B, Li T, Xie C, Sun Z, Liu D, et al. Fabrication of high-entropy perovskite oxide by reactive flash sintering. Ceram Int 2020;46:18358–61.
[156] Messing GL, Zhang S-C, Jayanthi GV. Ceramic powder synthesis by spray pyrolysis. J Am Ceram Soc 1993;76:2707–26.
[157] Sarkar A, Djenadic R, Usharani NJ, Sanghvi KP, Chakravadhanula VSK, Gandhi AS, et al. Nanocrystalline multicomponent entropy stabilised transition metal oxides. J Eur Ceram Soc 2017;37:747–54.
[158] Anandkumar M, Bhattacharya S, Deshpande AS. Low temperature synthesis and characterization of single phase multi-component fluorite oxide nanoparticle sols. RSC Adv 2019;9:26825–30.
[159] Wang G, Qin J, Feng Y, Feng B, Yang S, Wang Z, et al. Sol-Gel synthesis of spherical mesoporous high-entropy oxides. ACS Appl Mater Interfaces 2020;12: 45155–64.
[160] Yang X, Wang H, Song Y, Liu K, Huang T, Wang X, et al. Low-temperature synthesis of a porous high-entropy transition-metal oxide as an anode for high-performance lithium-ion batteries. ACS Appl Mater Interfaces 2022;14:26873–81.

[161] Sun Y, Wu T, Bao Z, Moon J, Huang Z, Chen Z, et al. Defect engineering of ceria nanocrystals for enhanced catalysis via a high-entropy oxide strategy. ACS Cent Sci 2022;8:1081–90.
[162] Rudin T, Wegner K, Pratsinis SE. Uniform nanoparticles by flame-assisted spray pyrolysis (FASP) of low cost precursors. J Nanopart Res 2011;13:2715–25.
[163] Punginsang M, Wisitsoraat A, Tuantranont A, Phanichphant S, Liewhiran C. Ultrafine Bi_2WO_6 nanoparticles prepared by flame spray pyrolysis for selective acetone gas-sensing. Mater Sci Semicond Process 2019;90:263–75.
[164] Phakatkar AH, Saray MT, Rasul MG, Sorokina LV, Ritter TG, Shokuhfar T, et al. Ultrafast synthesis of high entropy oxide nanoparticles by flame spray pyrolysis. Langmuir 2021;37:9059–68.
[165] Wu H, Lu Q, Li Y, Wang J, Li Y, Jiang R, et al. Rapid joule-heating synthesis for manufacturing high-entropy oxides as efficient electrocatalysts. Nano Lett 2022;22:6492–500.
[166] Colombo R, Garino N, Versaci D, Amici J, Para ML, Quartarone E, et al. Designing a double-coated cathode with high entropy oxides by microwave-assisted hydrothermal synthesis for highly stable Li–S batteries. J Mater Sci 2022;57:15690–704.
[167] Yang B, Zhang Q, Huang H, Pan H, Zhu W, Meng F, et al. Engineering relaxors by entropy for high energy storage performance. Nat Energy 2023;8:956–64.
[168] Raza H, Cheng J, Lin C, Majumder S, Zheng G, Chen G. High-entropy stabilized oxides derived via a low-temperature template route for high-performance lithium-sulfur batteries. EcoMat 2023;5:e12324.
[169] Kante MV, Weber ML, Ni S, van den Bosch ICG, van der Minne E, Heymann L, et al. A high-entropy oxide as high-activity electrocatalyst for water oxidation. ACS Nano 2023;17:5329–39.
[170] Strotkötter V, Krysiak OA, Zhang J, Wang X, Suhr E, Schuhmann W, et al. Discovery of high-entropy oxide electrocatalysts: from thin-film material libraries to particles. Chem Mater 2022;34:10291–303.
[171] Farhan A, Cocconcelli M, Stramaglia F, Kuznetsov N, Flajšman L, Wyss M, et al. Element-sensitive x-ray absorption spectroscopy and magnetometry of Lu ($Fe_{0.2}$ $Mn_{0.2}$ $Co_{0.2}$ $Cr_{0.2}$ $Ni_{0.2}$) O_3 high-entropy oxide perovskite thin films. Phys Rev Mater 2023;7:044402.
[172] Cheng B, Lou H, Sarkar A, Zeng Z, Zhang F, Chen X, et al. Lattice distortion and stability of ($Co_{0.2}Cu_{0.2}Mg_{0.2}Ni_{0.2}Zn_{0.2}$)O high-entropy oxide under high pressure. Mater Today Adv 2020;8:100102.
[173] Cheng B, Lou H, Sarkar A, Zeng Z, Zhang F, Chen X, et al. Pressure-induced tuning of lattice distortion in a high-entropy oxide. Commun Chem 2019;2:114.
[174] Wang J, Stenzel D, Azmi R, Najib S, Wang K, Jeong J, et al. Spinel to rock-salt transformation in high entropy oxides with li incorporation. Electrochem 2020;1:60–74.
[175] Ding F, Ji P, Han Z, Hou X, Yang Y, Hu Z, et al. Tailoring planar strain for robust structural stability in high-entropy layered sodium oxide cathode materials. Nat Energy 2024.
[176] Okunishi E, Sawada H, Kondo Y. Experimental study of annular bright field (ABF) imaging using aberration-corrected scanning transmission electron microscopy (STEM). Micron 2012;43:538–44.
[177] High-Resolution STEM Imaging. In: Fultz B, Howe JM, editors. Transmission Electron Microscopy and Diffractometry of Materials. Berlin, Heidelberg: Springer Berlin Heidelberg; 2008. p. 583-609.
[178] Nellist PD, Chisholm MF, Dellby N, Krivanek OL, Murfitt MF, Szilagyi ZS, et al. Direct sub-angstrom imaging of a crystal lattice. Science 2004;305:1741 -.
[179] Guo H-X, Wang W-M, He C-Y, Liu B-H, Yu D-M, Liu G, et al. Entropy-assisted high-entropy oxide with a spinel structure toward high-temperature infrared radiation materials. ACS Appl Mater Interfaces 2022;14:1950–60.
[180] Ghigna P, Airoldi L, Fracchia M, Callegari D, Anselmi-Tamburini U, D'Angelo P, et al. Lithiation mechanism in high-entropy oxides as anode materials for Li-Ion batteries: an operando XAS study. ACS Appl Mater Interfaces 2020;12:50344–54.
[181] Zheng Y, Wu X, Lan X, Hu R. A spinel $(FeNiCrMnMgAl)_3O_4$ high entropy oxide as a cycling stable anode material for Li-Ion batteries. Processes 2022;10:49.
[182] Titus D, James Jebaseelan Samuel E, Roopan SM. Chapter 12 - Nanoparticle characterization techniques. In: Shukla AK, Iravani S, editors. Green Synthesis, Characterization and Applications of Nanoparticles: Elsevier; 2019. p. 303-19.
[183] Xu H, Zhang Z, Liu J, Do-Thanh C-L, Chen H, Xu S, et al. Entropy-stabilized single-atom Pd catalysts via high-entropy fluorite oxide supports. Nat Commun 2020;11:3908.
[184] Le Gal A, Vallès M, Julbe A, Abanades S. Thermochemical properties of high entropy oxides used as redox-active materials in two-step solar fuel production cycles. Catalysts 2022;12:1116.
[185] Sarkar A, Mannava PK, Velasco L, Das C, Breitung B, Bhattacharya SS, et al. Determining role of individual cations in high entropy oxides: structure and reversible tuning of optical properties. Scr Mater 2022;207:114273.
[186] Phakatkar A, Shahbazian-Yassar R, Shokuhfar T. STEM-EELS analysis of high entropy oxide nanoparticles. Microsc Microanal 2021;27:884–6.
[187] Braun JL, Rost CM, Lim M, Giri A, Olson DH, Kotsonis GN, et al. Charge-induced disorder controls the thermal conductivity of entropy-stabilized oxides. Adv Mater 2018;30:1805004.
[188] Iglesias-Juez A, Chiarello GL, Patience GS, Guerrero-Pérez MO. Experimental methods in chemical engineering: X-ray absorption spectroscopy—XAS, XANES, EXAFS. Can J Chem Eng 2022;100:3–22.
[189] Hu C, Yue K, Han J, Liu X, Liu L, Liu Q, et al. Misoriented high-entropy iridium ruthenium oxide for acidic water splitting. Sci Adv 2023;9:eadf9144.
[190] Wang K, Hua W, Huang X, Stenzel D, Wang J, Ding Z, et al. Synergy of cations in high entropy oxide lithium ion battery anode. Nat Commun 2023;14:1487.
[191] Timoshenko J, Kuzmin A. Wavelet data analysis of EXAFS spectra. Comput Phys Commun 2009;180:920–5.
[192] Usharani NJ, Shringi R, Sanghavi H, Subramanian S, Bhattacharya SS. Role of size, alio-/multi-valency and non-stoichiometry in the synthesis of phase-pure high entropy oxide (Co, Cu, Mg, Na, Ni, Zn)O. Dalton Trans 2020;49:7123–32.
[193] Dąbrowa J, Stygar M, Mikuła A, Knapik A, Mroczka K, Tejchman W, et al. Synthesis and microstructure of the (Co, Cr, Fe, Mn, Ni)$_3O_4$ high entropy oxide characterized by spinel structure. Mater Lett 2018;216:32–6.
[194] Berardan D, Meena AK, Franger S, Herrero C, Dragoe N. Controlled Jahn-Teller distortion in (MgCoNiCuZn)O-based high entropy oxides. J Alloy Compd 2017;704:693–700.
[195] Hooch Antink W, Lee S, Lee HS, Shin H, Yoo TY, Ko W, et al. High-valence metal-driven electronic modulation for boosting oxygen evolution reaction in high-entropy spinel oxide. Adv Funct Mater 2024;34:2309438.
[196] Dragoe N, Bérardan D. Order emerging from disorder. Science 2019;366:573–4.
[197] Shi X-L, Zou J, Chen Z-G. Advanced thermoelectric design: from materials and structures to devices. Chem Rev 2020;120:7399–515.
[198] Chen W-Y, Shi X-L, Zou J, Chen Z-G. Thermoelectric coolers: progress, challenges, and opportunities. Small Methods 2022;6:2101235.
[199] Cao T, Shi X-L, Chen Z-G. Advances in the design and assembly of flexible thermoelectric device. Prog Mater Sci 2023;131:101003.
[200] He J, Liu Y, Funahashi R. Oxide thermoelectrics: The challenges, progress, and outlook. J Mater Res 2011;26:1762–72.
[201] Ren G-K, Lan J-L, Zhao L-D, Liu C, Yuan H, Shi Y, et al. Layered oxygen-containing thermoelectric materials: mechanisms, strategies, and beyond. Mater Today 2019;29:68–85.
[202] Fergus JW. Oxide materials for high temperature thermoelectric energy conversion. J Eur Ceram Soc 2012;32:525–40.
[203] Lin YH, Lan J, Nan C. Oxide thermoelectric materials: from basic principles to applications2019.
[204] Snyder GJ, Toberer ES. Complex thermoelectric materials. Nat Mater 2008;7:105–14.
[205] Thermoelectrics RDM. Handbook: Macro to Nano. CRC Press; 2018.
[206] Xiao Y, Wang D, Zhang Y, Chen C, Zhang S, Wang K, et al. Band sharpening and band alignment enable high quality factor to enhance thermoelectric performance in n-type PbS. J Am Chem Soc 2020;142:4051–60.
[207] Kim S, Hwang J, You T-S, Yeon S, Kim J, Yu B-K, et al. Enhanced thermoelectric performance by resonant doping and embedded magnetic impurity. Phys Rev Appl 2023;19:014034.
[208] Liu H-T, Sun Q, Zhong Y, Deng Q, Gan L, Lv F-L, et al. High-performance in n-type PbTe-based thermoelectric materials achieved by synergistically dynamic doping and energy filtering. Nano Energy 2022;91:106706.

[209] Lin Y, Dylla MT, Kuo JJ, Male JP, Kinloch IA, Freer R, et al. Graphene/strontium titanate: approaching single crystal-like charge transport in polycrystalline oxide perovskite nanocomposites through grain boundary engineering. Adv Funct Mater 2020;30:1910079.
[210] Lin Y, Wood M, Imasato K, Kuo JJ, Lam D, Mortazavi AN, et al. Expression of interfacial Seebeck coefficient through grain boundary engineering with multi-layer graphene nanoplatelets. Energ Environ Sci 2020;13:4114–21.
[211] Hu C, Xia K, Fu C, Zhao X, Zhu T. Carrier grain boundary scattering in thermoelectric materials. Energ Environ Sci 2022;15:1406–22.
[212] Ren G-K, Wang S, Zhou Z, Li X, Yang J, Zhang W, et al. Complex electronic structure and compositing effect in high performance thermoelectric BiCuSeO. Nat Commun 2019;10:2814.
[213] Zhou Z, Huang Y, Wei B, Yang Y, Yu D, Zheng Y, et al. Compositing effects for high thermoelectric performance of Cu_2Se-based materials. Nat Commun 2023;14:2410.
[214] Koumoto K, Wang YF, Zhang RZ, Kosuga A, Funahashi R. Oxide 'Thermoelectric Materials: A Nanostructuring Approach. In: Clarke DR, Ruhle M, Zok F, editors. Annual Review of Materials Research, Vol 402010. p. 363-94.
[215] Nielsch K, Bachmann J, Kimling J, Böttner H. Thermoelectric nanostructures: from physical model systems towards nanograined composites. Adv Energy Mater 2011;1:713–31.
[216] Ma Y, Ma Y, Wang Q, Schweidler S, Botros M, Fu T, et al. High-entropy energy materials: challenges and new opportunities. Energ Environ Sci 2021;14:2883–905.
[217] Jiang B, Yu Y, Cui J, Liu X, Xie L, Liao J, et al. High-entropy-stabilized chalcogenides with high thermoelectric performance. Science 2021;371:830–4.
[218] Luo Y, Hao S, Cai S, Slade TJ, Luo ZZ, Dravid VP, et al. High thermoelectric performance in the new cubic semiconductor $AgSnSbSe_3$ by high-entropy engineering. J Am Chem Soc 2020;142:15187–98.
[219] Ma Z, Xu T, Li W, Cheng Y, Li J, Zhang D, et al. High entropy semiconductor $AgMnGeSbTe_4$ with desirable thermoelectric performance. Adv Funct Mater 2021;31:2103197.
[220] Ren G-K, Lan J-L, Ventura KJ, Tan X, Lin Y-H, Nan C-W. Contribution of point defects and nano-grains to thermal transport behaviours of oxide-based thermoelectrics. npj Comput Mater 2016;2:16023.
[221] Gurunathan R, Hanus R, Snyder GJ. Alloy scattering of phonons. Mater Horiz 2020;7:1452–6.
[222] Klemens PG. The scattering of low-frequency lattice waves by static imperfections. Proc Phys Soc London, Sect A 1955;68:1113.
[223] Klemens PG. Thermal resistance due to point defects at high temperatures. Phys Rev 1960;119:507–9.
[224] Hanus R, Gurunathan R, Lindsay L, Agne MT, Shi J, Graham S, et al. Thermal transport in defective and disordered materials. Appl Phys Rev 2021;8.
[225] Körmann F, Ikeda Y, Grabowski B, Sluiter MHF. Phonon broadening in high entropy alloys. npj Comput Mater 2017;3:36.
[226] Zhao M, Ren X, Pan W. Effect of lattice distortion and disordering on the mechanical properties of Titania-doped Yttria-stabilized zirconia. J Am Ceram Soc 2014;97:1566–71.
[227] Zhao Z, Chen H, Xiang H, Dai F-Z, Wang X, Xu W, et al. High entropy defective fluorite structured rare-earth niobates and tantalates for thermal barrier applications. J Adv Ceram 2020;9:303–11.
[228] Jiang B, Yu Y, Chen H, Cui J, Liu X, Xie L, et al. Entropy engineering promotes thermoelectric performance in p-type chalcogenides. Nat Commun 2021;12:3234.
[229] Yang B, Zhang Y, Pan H, Si W, Zhang Q, Shen Z, et al. High-entropy enhanced capacitive energy storage. Nat Mater 2022;21:1074–80.
[230] Dou L, Yang B, Lan S, Liu Y, Liu Y, Nan C-W, et al. High-entropy-nanofibers enhanced polymer nanocomposites for high-performance energy storage. Adv Energy Mater 2023;13:2203925.
[231] Li F, Li J-F, Zhao L-D, Xiang K, Liu Y, Zhang B-P, et al. Polycrystalline BiCuSeO oxide as a potential thermoelectric material. Energ Environ Sci 2012;5:7188–95.
[232] Tan X, Lan J-L, Liu Y-C, Ren G-K, Zeng C-C, Lin Y-H, et al. Optimization of the thermoelectric properties of Bi_2O_2Se ceramics by altering the temperature of spark plasma sintering. J Electroceram 2016;37:66–72.
[233] Zhu T, Gao H, Chen Y, Zhao X. Ioffe-Regel limit and lattice thermal conductivity reduction of high performance $(AgSbTe_2)_{15}(GeTe)_{85}$ thermoelectric materials. J Mater Chem A 2014;2:3251–6.
[234] Rowe DM, Shukla VS, Savvides N. Phonon scattering at grain boundaries in heavily doped fine-grained silicon–germanium alloys. Nature 1981;290:765–6.
[235] Hu L, Zhang Y, Wu H, Li J, Li Y, Mckenna M, et al. Entropy engineering of SnTe: multi-principal-element alloying leading to ultralow lattice thermal conductivity and state-of-the-art thermoelectric performance. Adv Energy Mater 2018;8:1802116.
[236] Zeng Y, Ouyang B, Liu J, Byeon Y-W, Cai Z, Miara LJ, et al. High-entropy mechanism to boost ionic conductivity. Science 2022;378:1320–4.
[237] Ranganathan S. Alloyed pleasures: Multimetallic cocktails. 2003.
[238] Zheng Y, Zhang Q, Shi C, Zhou Z, Lu Y, Han J, et al. Carrier-phonon decoupling in perovskite thermoelectrics via entropy engineering. Nat Commun 2024;15:7650.
[239] Zhu B, Chen C, Yao Z, Chen J, Jia C, Wang Z, et al. Multiple doped ZnO with enhanced thermoelectric properties. J Eur Ceram Soc 2021;41:4182–8.
[240] Wang J, Zhang B-Y, Kang H-J, Li Y, Yaer X, Li J-F, et al. Record high thermoelectric performance in bulk $SrTiO_3$ via nano-scale modulation doping. Nano Energy 2017;35:387–95.
[241] Tilley RJD. Perovskites: structure-property relationships. MRS Bull 2017;42:325–7.
[242] Zhang P, Lou Z, Qin M, Xu J, Zhu J, Shi Z, et al. High-entropy $(Ca_{0.2}Sr_{0.2}Ba_{0.2}La_{0.2}Pb_{0.2})TiO_3$ perovskite ceramics with A-site short-range disorder for thermoelectric applications. J Mater Sci Technol 2022;97:182–9.
[243] Zhang P, Lou Z, Gong L, Xu J, Chen Q, Reece MJ, et al. High-entropy $MTiO_3$ perovskite oxides with glass-like thermal conductivity for thermoelectric applications. J Alloy Compd 2023;937:168366.
[244] Zhang P, Gong L, Lou Z, Xu J, Cao S, Zhu J, et al. Reduced lattice thermal conductivity of perovskite-type high-entropy $(Ca_{0.25}Sr_{0.25}Ba_{0.25}RE_{0.25})TiO_3$ ceramics by phonon engineering for thermoelectric applications. J Alloy Compd 2022;898:162858.
[245] Yao J, Chen T, Wang H, Khan M, Tan C, Sun Y, et al. Stable cubic crystal structures and optimized thermoelectric performance of $SrTiO_3$-based ceramics driven by entropy engineering. J Mater Chem A 2022;10:24561–72.
[246] Shi Z, Zhang J, Wei J, Hou X, Cao S, Tong S, et al. A-site deficiency improved the thermoelectric performance of high-entropy perovskite manganite-based ceramics. J Mater Chem C 2022;10:15582–92.
[247] Kumar A, Dragoe D, Berardan D, Dragoe N. Thermoelectric properties of high-entropy rare-earth cobaltates. J Materiomics 2023;9:191–6.
[248] Yang C, Wu H, Song H, Wang X, Chen S, Xu X, et al. Ultralow thermal conductivity and enhanced thermoelectric properties in a textured $(Ca_{0.35}Sr_{0.2}Ba_{0.15}Na_{0.2}Bi_{0.1})_3Co_4O_9$ high-entropy ceramic. J Alloy Compd 2023;940:168802.
[249] Shi Z, Su T, Zhang P, Lou Z, Qin M, Gao T, et al. Enhanced thermoelectric performance of $Ca_3Co_4O_9$ ceramics through grain orientation and interface modulation. J Mater Chem A 2020;8:19561–72.
[250] Cheng Chang MGK. High-entropy thermoelectric materials emerging. Mater Lab 2023;2:220048.
[251] Popuri SR, Decourt R, McNulty JA, Pollet M, Fortes AD, Morrison FD, et al. Phonon-glass and heterogeneous electrical transport in A-site-deficient $SrTiO_3$. J Phys Chem C 2019;123:5198–208.
[252] Daniels LM, Savvin SN, Pitcher MJ, Dyer MS, Claridge JB, Ling S, et al. Phonon-glass electron-crystal behaviour by A site disorder in n-type thermoelectric oxides. Energ Environ Sci 2017;10:1917–22.
[253] Wang Y, Lee KH, Hyuga H, Kita H, Inaba K, Ohta H, et al. Enhancement of Seebeck coefficient for $SrO(SrTiO_3)_2$ by Sm substitution: crystal symmetry restoration of distorted TiO6 octahedra. Appl Phys Lett 2007;91.
[254] Ma Z, Luo Y, Li W, Xu T, Wei Y, Li C, et al. High thermoelectric performance and low lattice thermal conductivity in lattice-distorted high-entropy semiconductors $AgMnSn_{1-x}PbxSbTe_4$. Chem Mater 2022;34:8959–67.
[255] Barr AED. Introduction to solid state physics. Phys Bull 1957;8:313.
[256] Leitner J, Voňka P, Sedmidubský D, Svoboda P. Application of Neumann-Kopp rule for the estimation of heat capacity of mixed oxides. Thermochim Acta 2010;497:7–13.

[257] Huo W, Liu X, Tan S, Fang F, Xie Z, Shang J, et al. Ultrahigh hardness and high electrical resistivity in nano-twinned, nanocrystalline high-entropy alloy films. Appl Surf Sci 2018;439:222–5.
[258] Srivastava A, Gaur NK. The role of lattice distortions in determining the thermal properties of electron doped $CaMnO_3$. J Phys Condens Matter 2009;21:096001.
[259] Roy A, Sreeramagiri P, Babuska T, Krick B, Ray PK, Balasubramanian G. Lattice distortion as an estimator of solid solution strengthening in high-entropy alloys. Mater Charact 2021;172:110877.
[260] Jiang B, Wang W, Liu S, Wang Y, Wang C, Chen Y, et al. High figure-of-merit and power generation in high-entropy GeTe-based thermoelectrics. Science 2022;377:208–13.
[261] Zhao Zifan XH, Fu-Zhi D, Zhijian P, Yanchun Z. $(La_{0.2}Ce_{0.2}Nd_{0.2}Sm_{0.2}Eu_{0.2})_2Zr_2O_7$: a novel high-entropy ceramic with low thermal conductivity and sluggish grain growth rate. J Mater Sci Technol 2019;35:2647–51.
[262] Zhang M, Lan S, Yang BB, Pan H, Liu YQ, Zhang QH, et al. Ultrahigh energy storage in high-entropy ceramic capacitors with polymorphic relaxor phase. Science 2024;384:185–9.
[263] Werman Y, Berg E. Mott-Ioffe-Regel limit and resistivity crossover in a tractable electron-phonon model. Phys Rev B 2016;93:075109.
[264] Clarke DR, Phillpot SR. Thermal barrier coating materials. Mater Today 2005;8:22–9.
[265] Padture NP, Gell M, Jordan EH. Thermal barrier coatings for gas-turbine engine applications. Science 2002;296:280–4.
[266] Wang X, Xiang H, Sun X, Liu J, Hou F, Zhou Y. Thermal properties of a prospective thermal barrier material: $Yb_3Al_5O_{12}$. J Mater Res 2014;29:2673–81.
[267] Qiu S, Xiang H, Dai F-Z, Wang H, Huang M, Wan C, et al. Medium-entropy $(Me, Ti)_{0.1}(Zr, Hf, Ce)_{0.9}O_2$ (Me = Y and Ta): promising thermal barrier materials for high-temperature thermal radiation shielding and CMAS blocking. J Mater Sci Technol 2022;123:144–53.
[268] Li F, Zhou L, Liu J-X, Liang Y, Zhang G-J. High-entropy pyrochlores with low thermal conductivity for thermal barrier coating materials. J Adv Ceram 2019;8:576–82.
[269] Ping X, Meng B, Li C, Lin W, Chen Y, Fang C, et al. Thermophysical and electrical properties of rare-earth-cerate high-entropy ceramics. J Am Ceram Soc 2022;105:4910–20.
[270] Liu D, Shi B, Geng L, Wang Y, Xu B, Chen Y. High-entropy rare-earth zirconate ceramics with low thermal conductivity for advanced thermal-barrier coatings. J Adv Ceram 2022;11:961–73.
[271] Guo Y, Feng S, Yang Y, Zheng R, Zhang Y, Fu J, et al. High-entropy titanate pyrochlore as newly low-thermal conductivity ceramics. J Eur Ceram Soc 2022;42:6614–23.
[272] He J, He G, Wang P, Xu L, Liu J, Tao J. Pyrochlore–fluorite dual-phase high-entropy $RE_2(Ce_{0.2}Zr_{0.2}Hf_{0.2}Sn_{0.2}Ti_{0.2})_2O_7$ ($RE_2HE_2O_7$, RE = La, Nd, Sm, Eu, Gd, Dy) ceramics with glass-like thermal conductivity. J Mater Sci 2022;57:17563–76.
[273] Ren K, Wang Q, Shao G, Zhao X, Wang Y. Multicomponent high-entropy zirconates with comprehensive properties for advanced thermal barrier coating. Scr Mater 2020;178:382–6.
[274] Xue Y, Zhao X, An Y, Wang Y, Gao M, Zhou H, et al. High-entropy $(La_{0.2}Nd_{0.2}Sm_{0.2}Eu_{0.2}Gd_{0.2})_2Ce_2O_7$: a potential thermal barrier material with improved thermo-physical properties. J Adv Ceram 2022;11:615–28.
[275] Xu L, Su L, Wang H, Gao H, Lu D, Peng K, et al. Tuning stoichiometry of high-entropy oxides for tailorable thermal expansion coefficients and low thermal conductivity. J Am Ceram Soc 2022;105:1548–57.
[276] Wright AJ, Luo J. A step forward from high-entropy ceramics to compositionally complex ceramics: a new perspective. J Mater Sci 2020;55:9812–27.
[277] Xu L, Su L, Wang H, Gao H, Guo P, Niu M, et al. High-entropy $Sm_2B_2O_7$ (B=Ti, Zr, Sn, Hf, Y, Yb, Nb, and Ta) oxides with highly disordered B-site cations for ultralow thermal conductivity. J Mater Sci Technol 2022;119:182–9.
[278] Xue Y, Zhao X, An Y, Nie H, Gao M, Zhou H, et al. Corrosion behavior of high-entropy $(La_{0.2}Nd_{0.2}Sm_{0.2}Eu_{0.2}Gd_{0.2})Ce_2O_7$ in different aggressive molten salt. Corros Sci 2022;204:110414.
[279] Wang Y, Zhu J, Shao G, Wang H, Li M, Lu H, et al. Synthesis of high-entropy $La_2B_2O_7$ ceramics with non-equivalent principal elements in B-sites and their CMAS resistance performance. J Alloy Compd 2022;924:166635.
[280] Xu L, Su L, Wang H, Niu M, Zhuang L, Peng K, et al. Phase evolution and thermophysical properties of high-entropy $RE_2(Y_{0.2}Yb_{0.2}Nb_{0.2}Ta_{0.2}Ce_{0.2})_2O_7$ oxides. J Am Ceram Soc 2022;105:5490–500.
[281] Tang A, Li B, Sang W, Hongsong Z, Chen X, Zhang H, et al. Thermophysical performances of high-entropy $(La_{0.2}Nd_{0.2}Yb_{0.2}Y_{0.2}Sm_{0.2})_2Ce_2O_7$ and $(La_{0.2}Nd_{0.2}Yb_{0.2}Y_{0.2}Lu_{0.2})_2Ce_2O_7$ oxides. Ceram Int 2022;48:5574–80.
[282] Haoming Z, Yan S, Weiwei S, Yihao G, Yukun Z, Yuzhu Z, et al. Thermophysical performances of novel high entropy $(La_{0.25}\ RE_{0.25}Yb_{0.25}\ Y_{0.25})_2Ce_2O_7$ (RE=Nd and Dy) oxides. Ceram Int 2022;48:8380–6.
[283] Junjie H, Guo H, Jing L, Jingchao T. New class of high-entropy defect fluorite oxides $RE_2(Ce_{0.2}Zr_{0.2}Hf_{0.2}Sn_{0.2}Ti_{0.2})_2O_7$ (RE = Y, Ho, Er, or Yb) as promising thermal barrier coatings. J Eur Ceram Soc 2021;41:6080–6.
[284] Liu H-L, Pang S, Liu C-Q, Wu Y-T, Zhang G-J. High-entropy yttrium pyrochlore ceramics with glass-like thermal conductivity for thermal barrier coating application. J Am Ceram Soc 2022;105:6437–48.
[285] Yang L, Kong X, Li F, Hao H, Cheng Z, Liu H, et al. Perovskite lead-free dielectrics for energy storage applications. Prog Mater Sci 2019;102:72–108.
[286] Wang G, Lu Z, Li Y, Li L, Ji H, Feteira A, et al. Electroceramics for high-energy density capacitors: current status and future perspectives. Chem Rev 2021;121:6124–72.
[287] Gür TM. Review of electrical energy storage technologies, materials and systems: challenges and prospects for large-scale grid storage. Energ Environ Sci 2018;11:2696–767.
[288] Zhao P, Cai Z, Chen L, Wu L, Huan Y, Guo L, et al. Ultra-high energy storage performance in lead-free multilayer ceramic capacitors via a multiscale optimization strategy. Energ Environ Sci 2020;13:4882–90.
[289] Wang D, Fan Z, Zhou D, Khesro A, Murakami S, Feteira A, et al. Bismuth ferrite-based lead-free ceramics and multilayers with high recoverable energy density. J Mater Chem A 2018;6:4133–44.
[290] Lu Z, Wang G, Bao W, Li J, Li L, Mostaed A, et al. Superior energy density through tailored dopant strategies in multilayer ceramic capacitors. Energ Environ Sci 2020;13:2938–48.
[291] Li J, Shen Z, Chen X, Yang S, Zhou W, Wang M, et al. Grain-orientation-engineered multilayer ceramic capacitors for energy storage applications. Nat Mater 2020;19:999–1005.
[292] Zhang X, Li J, Ni B, Yang R, Xie H, Yang S, et al. Dielectric properties of novel high-entropy $(La_{0.2}Li_{0.2}Ba_{0.2}Sr_{0.2}Ca_{0.2})Nb_2O_6$-δ tungsten bronze ceramics. J Mater Sci 2022;57:15901–12.
[293] Xie H, Li J, Yang S, Wu L, Li P, Qi X. Microstructures and dielectric properties of novel $(La_{0.2}Pr_{0.2}Nd_{0.2}Sm_{0.2}Eu_{0.2})_2Ce_2O_7$ high entropy ceramics. J Mater Sci Mater Electron 2021;32:27860–70.
[294] Wang Y, Jie W, Yang C, Wei X, Hao J. Colossal permittivity materials as superior dielectrics for diverse applications. Adv Funct Mater 2019;29:1808118.
[295] Hu Z, Zhang H, Reece MJ, Viola G, Yan H. Relaxor ferroelectric behaviour observed in $(Ca_{0.5}Sr_{0.5}Ba_{0.5}Pb_{0.5})Nb_2O_7$ perovskite layered structure ceramics. J Eur Ceram Soc 2023;43:177–82.
[296] Sharma Y, Lee M-C, Pitike KC, Mishra KK, Zheng Q, Gao X, et al. High entropy oxide relaxor ferroelectrics. ACS Appl Mater Interfaces 2022;14:11962–70.
[297] Ding YH, Liu L, Guo RZ, Li L, Chen XM. $(Hf_{0.25}Zr_{0.25}Sn_{0.25}Ti_{0.25})O_2$ high-entropy ceramics and their microwave dielectric characteristics. J Am Ceram Soc 2022;105:6710–7.
[298] Xiang H, Yao L, Chen J, Yang A, Yang H, Fang L. Microwave dielectric high-entropy ceramic $Li(Gd_{0.2}Ho_{0.2}Er_{0.2}Yb_{0.2}Lu_{0.2})GeO_4$ with stable temperature coefficient for low-temperature cofired ceramic technologies. J Mater Sci Technol 2021;93:28–32.
[299] Qi J, Zhang M, Chen Y, Luo Z, Zhao P, Su H, et al. High-entropy assisted $BaTiO_3$-based ceramic capacitors for energy storage. Cell Rep Phys Sci 2022;3:101110.
[300] Chen L, Deng S, Liu H, Wu J, Qi H, Chen J. Giant energy-storage density with ultrahigh efficiency in lead-free relaxors via high-entropy design. Nat Commun 2022;13:3089.

[301] Liu X, Li X, Li Y, Zhang H, Jia Q, Zhang S, et al. High-entropy oxide: a future anode contender for lithium-ion battery. EcoMat 2022;4:e12261.
[302] Nguyen TX, Tsai C-C, Patra J, Clemens O, Chang J-K, Ting J-M. Co-free high entropy spinel oxide anode with controlled morphology and crystallinity for outstanding charge/discharge performance in Lithium-ion batteries. Chem Eng J 2022;430:132658.
[303] Patra J, Nguyen TX, Tsai C-C, Clemens O, Li J, Pal P, et al. Effects of elemental modulation on phase purity and electrochemical properties of Co-free high-entropy spinel oxide anodes for lithium-ion batteries. Adv Funct Mater 2022;32:2110992.
[304] Chen TY, Wang SY, Kuo CH, Huang SC, et al. In operando synchrotron X-ray studies of a novel spinel $(Ni_{0.2}Co_{0.2}Mn_{0.2}Fe_{0.2}Ti_{0.2})_3O_4$ high-entropy oxide for energy storage applications. J Mater Chem A 2020;8:21756–70.
[305] Xiang H-Z, Xie H-X, Chen Y-X, Zhang H, Mao A, Zheng C-H. Porous spinel-type $(Al_{0.2}CoCrFeMnNi)_{0.58}O_4$-δ high-entropy oxide as a novel high-performance anode material for lithium-ion batteries. J Mater Sci 2021;56:8127–42.
[306] Qiu N, Chen H, Yang Z, Sun S, Wang Y, Cui Y. A high entropy oxide ($Mg_{0.2}Co_{0.2}Ni_{0.2}Cu_{0.2}Zn_{0.2}O$) with superior lithium storage performance. J Alloy Compd 2019;777:767–74.
[307] Luo X-F, Patra J, Chuang W-T, Nguyen TX, Ting J-M, Li J, et al. Charge-discharge mechanism of high-entropy Co-free spinel oxide toward Li+ storage examined using operando quick-scanning X-Ray absorption spectroscopy. Adv Sci 2022;9:2201219.
[308] Xiao B, Wu G, Wang T, Wei Z, Sui Y, Shen B, et al. High-entropy oxides as advanced anode materials for long-life lithium-ion Batteries. Nano Energy 2022;95:106962.
[309] Yuan K, Tu T, Shen C, Zhou L, Liu J, Li J, et al. Self-ball milling strategy to construct high-entropy oxide coated $LiNi_{0.8}Co_{0.1}Mn_{0.1}O_2$ with enhanced electrochemical performance. J Adv Ceram 2022;11:882–92.
[310] Wang Q, Sarkar A, Wang D, Velasco L, Azmi R, Bhattacharya SS, et al. Multi-anionic and -cationic compounds: new high entropy materials for advanced Li-ion batteries. Energ Environ Sci 2019;12:2433–42.
[311] Zhao C, Wang C, Liu X, Hwang I, Li T, Zhou X, et al. Suppressing strain propagation in ultrahigh-Ni cathodes during fast charging via epitaxial entropy-assisted coating. Nat Energy 2024;9:345–56.
[312] Liang L, Su M, Sun Z, Wang L, Hou L, Liu H, et al. High-entropy doping promising ultrahigh-Ni Co-free single-crystalline cathode toward commercializable high-energy lithium-ion batteries. Sci Adv 2024;10:eado4472.
[313] Yang Y, Cai J, Zuo Y, Zhang K, Gao C, Zhou L, et al. Enhancing the stability of Li-Rich Mn-based oxide cathodes through surface high-entropy strategy. Energy Storage Mater 2024;71:103587.
[314] Sturman J, Yim C-H, Baranova EA, Abu-Lebdeh Y. Communication—design of $LiNi_{0.2}Mn_{0.2}Co_{0.2}Fe_{0.2}Ti_{0.2}O_2$ as a high-entropy cathode for lithium-ion batteries guided by machine learning. J Electrochem Soc 2021;168:050541.
[315] Wang J, Cui Y, Wang Q, Wang K, Huang X, Stenzel D, et al. Lithium containing layered high entropy oxide structures. Sci Rep 2020;10:18430.
[316] Zheng Q, Ren Z, Zhang Y, Qin T, Qi J, Jia H, et al. Surface phase conversion in a high-entropy layered oxide cathode material. ACS Appl Mater Interfaces 2023;15:4643–51.
[317] Shi Z, Ding Y, Zhang Q, Sun J. Electrocatalyst modulation toward bidirectional sulfur Redox in Li–S batteries: from strategic probing to mechanistic understanding. Adv Energy Mater 2022;12:2201056.
[318] Tian L, Zhang Z, Liu S, Li G, Gao X. High-entropy perovskite oxide nanofibers as efficient bidirectional electrocatalyst of liquid-solid conversion processes in lithium-sulfur batteries. Nano Energy 2023;106:108037.
[319] Tian L, Zhang Z, Liu S, Li G, Gao X. High-entropy spinel oxide nanofibers as catalytic sulfur hosts promise the high gravimetric and volumetric capacities for Lithium-Sulfur batteries. Energy Environ Mater 2022;5:645–54.
[320] Zheng Y, Yi Y, Fan M, Liu H, Li X, Zhang R, et al. A high-entropy metal oxide as chemical anchor of polysulfide for lithium-sulfur batteries. Energy Storage Mater 2019;23:678–83.
[321] Miao X, Guan S, Ma C, Li L, Nan C-W. Role of interfaces in solid-state batteries. Adv Mater. n/a 2206402.
[322] Bérardan D, Franger S, Meena AK, Dragoe N. Room temperature lithium superionic conductivity in high entropy oxides. J Mater Chem A 2016;4:9536–41.
[323] Osenciat N, Bérardan D, Dragoe D, Léridon B, Holé S, Meena AK, et al. Charge compensation mechanisms in Li-substituted high-entropy oxides and influence on Li superionic conductivity. J Am Ceram Soc 2019;102:6156–62.
[324] Liu W, Jiang J, Yang Z, Liu Y, Yang Z, Bu M, et al. Poly(ethylene oxide)-based composite electrolyte with lithium-doped high-entropy oxide ceramic enabled robust solid-state lithium-metal batteries. Chem–Asian J 2022;17:e202200839.
[325] Pan Y, Liu J-X, Tu T-Z, Wang W, Zhang G-J. High-entropy oxides for catalysis: a diamond in the rough. Chem Eng J 2023;451:138659.
[326] Gao Y, Liu Y, Yu H, Zou D. High-entropy oxides for catalysis: status and perspectives. Appl Catal A 2022;631:118478.
[327] Wang Y, Mi J, Wu Z-S. Recent status and challenging perspective of high entropy oxides for chemical catalysis. Chem Catal 2022;2:1624–56.
[328] Li H, Zhu H, Zhang S, Zhang N, Du M, Chai Y. Nano high-entropy materials: synthesis strategies and catalytic applications. Small Struct 2020;1:2000033.
[329] Li T, Yao Y, Huang Z, Xie P, Liu Z, Yang M, et al. Denary oxide nanoparticles as highly stable catalysts for methane combustion. Nat Catal 2021;4:62–70.
[330] Feng D, Dong Y, Zhang L, Ge X, Zhang W, Dai S, et al. Holey lamellar high-entropy oxide as an ultra-high-activity heterogeneous catalyst for solvent-free aerobic oxidation of benzyl alcohol. Angew Chem Int Ed 2020;59:19503–9.
[331] Wang L, Hossain MD, Du Y, Chambers SA. Exploring the potential of high entropy perovskite oxides as catalysts for water oxidation. Nano Today 2022;47:101697.
[332] Tang L, Yang Y, Guo H, Wang Y, Wang M, Liu Z, et al. High configuration entropy activated lattice oxygen for O_2 formation on perovskite electrocatalyst. Adv Funct Mater 2022;32:2112157.
[333] Wang Q, Li J, Li Y, Shao G, Jia Z, Shen B. Non-noble metal-based amorphous high-entropy oxides as efficient and reliable electrocatalysts for oxygen evolution reaction. Nano Res 2022;15:8751–9.
[334] Yu Y, Li H, Liu J, Xu W, Zhang D, Xiong J, et al. High entropy stabilizing lattice oxygen participation of Ru- based oxides in acidic water oxidation. J Mater Chem A 2022;10:21260–5.
[335] Yang X, Liping S, Qiang L, Lihua H, Hui Z. Co-prosperity of electrocatalytic activity and stability in high entropy spinel $(Cr_{0.2}Mn_{0.2}Fe_{0.2}Ni_{0.2}Zn_{0.2})_3O_4$ for the oxygen evolution reaction. J Mater Chem A 2022;10:17633–41.
[336] Yang JX, Dai B-H, Chiang C-Y, Chiu IC, Pao C-W, Lu S-Y, et al. Rapid fabrication of high-entropy ceramic nanomaterials for catalytic reactions. ACS Nano 2021;15:12324–33.
[337] Jin Z, Lyu J, Zhao Y-L, Li H, Chen Z, Lin X, et al. Top-down synthesis of noble metal particles on high-entropy oxide supports for electrocatalysis. Chem Mater 2021;33:1771–80.
[338] Okazaki Y, Fujita Y, Murata H, Masuyama N, Nojima Y, Ikeno H, et al. Composition-designed multielement perovskite oxides for oxygen evolution catalysis. Chem Mater 2022;34:10973–81.
[339] Li T, Yao Y, Ko BH, Huang Z, Dong Q, Gao J, et al. Carbon-supported high-entropy oxide nanoparticles as stable electrocatalysts for oxygen reduction reactions. Adv Funct Mater 2021;31:2010561.
[340] Jin Z, Lyu J, Hu K, Chen Z, Xie G, Liu X, et al. Eight-component nanoporous high-entropy oxides with low Ru contents as high-performance bifunctional catalysts in Zn-Air batteries. Small 2022;18:2107207.
[341] Chen Z, Wu J, Chen Z, Yang H, Zou K, Zhao X, et al. Entropy enhanced perovskite oxide ceramic for efficient electrochemical reduction of oxygen to hydrogen peroxide. Angew Chem Int Ed 2022;61:e202200086.
[342] Abdelhafiz A, Wang B, Harutyunyan AR, Li J. Carbothermal shock synthesis of high entropy oxide catalysts: dynamic structural and chemical reconstruction boosting the catalytic activity and stability toward oxygen evolution reaction. Adv Energy Mater 2022;12:2200742.
[343] He S, Somayaji V, Wang M, Lee S-H, Geng Z, Zhu S, et al. High entropy spinel oxide for efficient electrochemical oxidation of ammonia. Nano Res 2022;15:4785–91.
[344] Chu K, Qin J, Zhu H, De Ras M, Wang C, Xiong L, et al. High-entropy perovskite oxides: a versatile class of materials for nitrogen reduction reactions. Sci China Mater 2022;65:2711–20.

[345] Sun Y, Yu L, Xu S, Xie S, Jiang L, Duan J, et al. Battery-driven N_2 electrolysis enabled by high-entropy catalysts: from theoretical prediction to prototype model. Small 2022;18:2106358.
[346] Edalati P, Shen X-F, Watanabe M, Ishihara T, Arita M, Fuji M, et al. High-entropy oxynitride as a low-bandgap and stable photocatalyst for hydrogen production. J Mater Chem A 2021;9:15076–86.
[347] Edalati P, Wang Q, Razavi-Khosroshahi H, Fuji M, Ishihara T, Edalati K. Photocatalytic hydrogen evolution on a high-entropy oxide. J Mater Chem A 2020;8:3814–21.
[348] Akrami S, Murakami Y, Watanabe M, Ishihara T, Arita M, Fuji M, et al. Defective high-entropy oxide photocatalyst with high activity for CO_2 conversion. Appl Catal B 2022;303:120896.
[349] Akrami S, Edalati P, Shundo Y, Watanabe M, Ishihara T, Fuji M, et al. Significant CO_2 photoreduction on a high-entropy oxynitride. Chem Eng J 2022;449:137800.
[350] Edalati P, Itagoe Y, Ishihara H, Ishihara T, Emami H, Arita M, et al. Visible-light photocatalytic oxygen production on a high-entropy oxide by multiple-heterojunction introduction. J Photochem Photobiol A Chem 2022;433:114167.
[351] Chen H, Fu J, Zhang P, Peng H, Abney CW, Jie K, et al. Entropy-stabilized metal oxide solid solutions as CO oxidation catalysts with high-temperature stability. J Mater Chem A 2018;6:11129–33.
[352] Chen D, Nie S, Wu L, Zheng X, Du S, Duan X, et al. Metal-tannin coordination assembly route to nanostructured high-entropy oxide perovskites with abundant defects. Chem Mater 2022;34:1746–55.
[353] Vij V, Sultan S, Harzandi AM, Meena A, Tiwari JN, Lee W-G, et al. Nickel-based electrocatalysts for energy-related applications: oxygen reduction, oxygen evolution, and hydrogen evolution reactions. ACS Catal 2017;7:7196–225.
[354] Fabbri E, Habereder A, Waltar K, Kötz R, Schmidt TJ. Developments and perspectives of oxide-based catalysts for the oxygen evolution reaction. Cat Sci Technol 2014;4:3800–21.
[355] Liu Y, Ye C, Chen L, Fan J, Liu C, Xue L, et al. High entropy-driven role of oxygen vacancies for water oxidation. Adv Funct Mater 2024;34:2314820.
[356] Wong HSP, Salahuddin S. Memory leads the way to better computing. Nat Nanotechnol 2015;10:191–4.
[357] He QL, Hughes TL, Armitage NP, Tokura Y, Wang KL. Topological spintronics and magnetoelectronics. Nat Mater 2022;21:15–23.
[358] Molnár G, Rat S, Salmon L, Nicolazzi W, Bousseksou A. Spin crossover nanomaterials: from fundamental concepts to devices. Adv Mater 2018;30:1703862.
[359] Kumari P, Gupta AK, Mishra RK, Ahmad MS, Shahi RR. A comprehensive review: recent progress on magnetic high entropy alloys and oxides. J Magn Magn Mater 2022;554:169142.
[360] Mao A, Xiang H-Z, Zhang Z-G, Kuramoto K, Yu H, Ran S. Solution combustion synthesis and magnetic property of rock-salt $(Co_{0.2}Cu_{0.2}Mg_{0.2}Ni_{0.2}Zn_{0.2})O$ high-entropy oxide nanocrystalline powder. J Magn Magn Mater 2019;484:245–52.
[361] Zhang J, Yan J, Calder S, Zheng Q, McGuire MA, Abernathy DL, et al. Long-range antiferromagnetic order in a rocksalt high entropy oxide. Chem Mater 2019;31:3705–11.
[362] Jimenez-Segura MP, Takayama T, Bérardan D, Hoser A, Reehuis M, Takagi H, et al. Long-range magnetic ordering in rocksalt-type high-entropy oxides. Appl Phys Lett 2019;114.
[363] Meisenheimer PB, Williams LD, Sung SH, Gim J, Shafer P, Kotsonis GN, et al. Magnetic frustration control through tunable stereochemically driven disorder in entropy-stabilized oxides. Phys Rev Mater 2019;3:104420.
[364] Pu Y, Moseley D, He Z, Pitike KC, Manley ME, Yan J, et al. (Mg, Mn, Fe Co, Ni)O: a rocksalt high-entropy oxide containing divalent Mn and Fe. Sci Adv 2023;9.eadi8809.
[365] Krysko E, Min L, Wang Y, Zhang N, Barber JP, Niculescu GE, et al. Studies on the structure and the magnetic properties of high-entropy spinel oxide (MgMnFeCoNi)Al2O4. APL Mater 2023;11.
[366] Senkale S, Kamp M, Mangold S, Indris S, Kienle L, Kremer RK, et al. Multi-method characterization of the high-entropy spinel oxide $Mn_{0.2}Co_{0.2}Ni_{0.2}Cu_{0.2}Zn_{0.2}Fe_2O_4$: entropy evidence, microstructure, and magnetic properties. Chemistry-Methods 2023;3. e202200043.
[367] Kumar A, Bérardan D, Dragoe D, Riviere E, Takayama T, Takagi H, et al. Magnetic and electrical properties of high-entropy rare-earth manganites. Mater Today Phys 2023;32:101026.
[368] Li W, Cui Y, Zhao Y, Chen Y. Preparation and magnetic properties of high-entropy perovskite oxide $(La_{0.2}Y_{0.2}Pr_{0.2}Nd_{0.2}Sm_{0.2})CrO_3$. J Supercond Nov Magn 2023;36:1413–9.
[369] Sharma Y, Mazza AR, Musico BL, Skoropata E, Nepal R, Jin R, et al. Magnetic texture in insulating single crystal high entropy oxide spinel films. ACS Appl Mater Interfaces 2021;13:17971–7.
[370] Jin F, Zhu Y, Li L, Pan Z, Pan D, Gu M, et al. Robust ferrimagnetism and switchable magnetic anisotropy in high-entropy ferrite film. Adv Funct Mater 2023;33:2214273.
[371] Ke W-E, Chen J-W, Liu C-E, Ku Y-C, Chang C-F, Shafer P, et al. Crystalline magnetic anisotropy in high entropy $(Fe\ Co,\ Ni,\ Cr,\ Mn)_3O_4$ oxide driven by single-element orbital anisotropy. Adv Funct Mater 2024;34:2312856.
[372] Musicó B, Wright Q, Ward TZ, Grutter A, Arenholz E, Gilbert D, et al. Tunable magnetic ordering through cation selection in entropic spinel oxides. Phys Rev Mater 2019;3:104416.
[373] Huang S, Zhu X, Sarkar S, Zhao Y. Challenges and opportunities for supercapacitors. APL Mater 2019;7.
[374] Park GL, Schäfer AI, Richards BS. Renewable energy-powered membrane technology: supercapacitors for buffering resource fluctuations in a wind-powered membrane system for brackish water desalination. Renew Energy 2013;50:126–35.
[375] Partridge J, Abouelamaimen DI. The role of supercapacitors in regenerative braking systems. Energies 2019;12:2683.
[376] Kurzweil P. Supercapacitors | Supercapacitors: electrochemical double-layer capacitors. reference module in chemistry, Mol Sci Chem Eng: Elsevier; 2023.
[377] Chen B, Zhang X-L, Zhang W-B, Yin Y, Feng J, Liu X-Y, et al. Electrochemical pseudocapacitance performance of high entropy carbide (FeCoCrMnNi)C film by magnetron sputtering technology. Ceram Int 2024;50:23302–14.
[378] Ren L, Liu J, Liu X, Luo J, Li J. Rapid synthesis of high-entropy antimonides under air atmosphere using microwave method to ultra-high energy density supercapacitors. J Alloy Compd 2023;967:171816.
[379] Zhu Z, Zhang Y, Kong D, He N, Chen Q. A novel high entropy hydroxide electrode material for promoting energy density of supercapacitors and its efficient synthesis strategy. Small 2024;20:2307754.
[380] Mohanty GC, Chowde Gowda C, Gakhad P, Das S, Sanjay M, Chowdhury S, et al. Iron-cobalt-nickel-copper-zinc (FeCoNiCuZn) high entropy alloy as positive electrode for high specific capacitance supercapacitor. Electrochim Acta 2023;470:143272.
[381] Gupta AK, Shubham K, Giri NK, Shahi RR. Electrochemical charge storage properties of novel inverse spinel (CuNiZnAlFe)O type high entropy oxide. Energy Storage 2024;6:e527.
[382] Gupta AK, Singh A, Kumari P, Giri NK, Shahi RR. Effect of synthesis routes on electrochemical properties as supercapacitor electrode for novel spinel (CuNiFeMnCo)O high entropy oxide. Energy Storage 2024;6:e538.
[383] Talluri B, Aparna ML, Sreenivasulu N, Bhattacharya SS, Thomas T. High entropy spinel metal oxide $(CoCrFeMnNi)_3O_4$ nanoparticles as a high-performance supercapacitor electrode material. J Energy Storage 2021;42:103004.
[384] Guo M, Liu Y, Zhang F, Cheng F, Cheng C, Miao Y, et al. Inactive Al3+-doped La(CoCrFeMnNiAlx)1/(5+x)O3 high-entropy perovskite oxides as high performance supercapacitor electrodes. J Adv Ceram 2022;11:742–53.
[385] Sreenivasulu N, Kumar UN, Madhav KMVV, Thomas T, Bhattacharya SS. Structural and electrochemical investigations on nanocrystalline high entropy spinel oxides for battery-like supercapacitor applications. ChemistrySelect 2022;7:e202104015.
[386] Li L, Ji P, Geng C, Li Y, Meng L, Zhou B, et al. Facile synthesis of high-entropy $(Co_{0.2}Cr_{0.2}Fe_{0.2}Mn_{0.2}Ni_{0.2})_3O_4$ nanopowders and their electrochemical properties as supercapacitor electrode. J Energy Storage 2023;73. 109182.
[387] Pasupathi A, Subramaniam Y. A novel strategy for rapid synthesis of nanostructured high-entropy metal oxides through thermal plasma for supercapacitor applications. Energy Fuel 2024;38:5534–44.

[388] Pasupathi A, Perumal M, Narayanamoorthi E, Palanisamy B, Subramaniam Y. Electrochemical charge storage performance of (Mn, Ni, Mo Co, Fe)$_3O_4$ high entropy oxide nanoparticles produced via thermal plasma route. Ceram Int 2024;50:26740–9.
[389] Yin Y, Zhang W-B, Chen B, Feng J, Yang J-L, Yang Z-Q, et al. Porous powder synthesis of (FeCoCrMnNi)$_3O_4$ high entropy ceramic and its supercapacitor applications. Ceram Int 2024;50:10292–304.
[390] Yin Y, Zhang W-B, Zhang X-L, Theint MM, Yang J-L, Yang Z-Q, et al. Low-dimensional high entropy oxide (FeCoCrMnNi)$_3O_4$ for supercapacitor applications. Dalton Trans 2023;52:9005–16.
[391] Hu H, Yang C, Chen F, Li J, Jia X, Wang Y, et al. High-entropy engineering reinforced surface electronic states and structural defects of hierarchical metal Oxides@Graphene fibers toward high-performance wearable supercapacitors. Adv Mater 2024;36:2406483.
[392] Liang B, Ai Y, Wang Y, Liu C, Ouyang S, Liu M. Spinel-type (FeCoCrMnZn)$_3O_4$ high-entropy oxide: facile preparation and supercapacitor performance. Materials 2020;13:5798.
[393] Gupta AK, Kumar A, Marndi M, Giri NK, Shahi RR. Studies on supercapacitor electrode performance of novel (AlCuCoFeMnNi)O high entropy spinel oxide admixed with different carbon-based additives. Energy Storage 2024;6:e70002.
[394] Nan H, Song K, Xu J, Lv S, Yu S, Hu X, et al. Dual-ion (de)intercalation into high-entropy perovskite oxides for aqueous alkaline battery-supercapacitor hybrid devices. Acta Mater 2023;257:119174.
[395] Zhang D, Xu S, Li T, Zhang M, Qi J, Wei F, et al. High-entropy oxides prepared by Dealloying method for supercapacitors. ACS Appl Eng Mater 2023;1:780–9.
[396] Lee D, Choi Y, Kim MC, Ji H, Shin H-C, Kim KH. Design and mechanism study of multi-phase materials for cathodes in high-performance supercapacitors. J Storage Mater 2022;52:104831.
[397] Koh YK. Thermal Conductivity and Phonon Transport. In: Bhushan B, editor. Encyclopedia of Nanotechnology. Dordrecht: Springer Netherlands; 2012. p. 2704-11.